LIGHT CONTROL THROUGH HIGHLY SCATTERING MEDIA

by

DONALD BENJAMAN CONKEY

B.S., Brigham Young University, 2005

M.S., Brigham Young University, 2007

M.S., University of Colorado at Boulder, 2011

A thesis submitted to the

Faculty of the Graduate School of the

University of Colorado in partial fulfillment

of the requirement for the degree of

Doctor of Philosophy

Department of Electrical, Computer, and Energy Engineering

2013

This thesis entitled:
Light Control through Highly Scattering Media
written by Donald Benjaman Conkey
has been approved for the Department of Electrical, Computer, and Energy Engineering

_____

(Rafael Piestun)

_____

(Todd W. Murray)

Date_____

The final copy of this thesis has been examined by the signatories, and we
Find that both the content and the form meet acceptable presentation standards
Of scholarly work in the above mentioned discipline.

Conkey, Donald Benjaman (Ph.D., Electrical, Computer, and Energy Engineering)

Light Control through Highly Scattering Media

Thesis directed by Professor Rafael Piestun

Imaging through opaque, highly scattering walls is a long sought after capability with potential applications in a variety of fields, such as biomedical imaging. The use of wavefront shaping to compensate for scattering has recently brought a renewed interest as a potential solution to this problem. This method relies on the ability to shape an incident wavefront to pre-compensate for scattering, thus providing light control through a scattering layer. In order for these techniques to begin to extend the imaging depth inside of living biological tissue several constraints must be overcome. As living biological tissue is dynamic these techniques must be able to optimize fast enough to overcome the dynamic nature of the tissue. Also key to the practicality of overcoming scattering is focusing light without direct access behind the scattering wall. This thesis presents means of overcoming these limitations through novel optimization algorithms, wavefront shaping for high-speed modulation, and photoacoustic feedback and imaging behind a scattering layer.

A genetic algorithm (GA) is applied for wavefront optimization as a means of enabling parallel mode optimization to increase the speed of the optimization procedure. The results presented show that not only does the GA optimize more quickly, it is more robust in low signal-to-noise (SNR) environments than other optimization algorithms. The low SNR performance is critical to high speed performance, because SNR decreases with the integration time. The GA wavefont optimization is extended towards more complex light control problems, specifically multi-color image projection through scattering layers.

To overcome wavefront shaping modulation frequency limitations a novel wavefront shaping technique utilizing a binary amplitude Digital Micromirror Device (DMD) is demonstrated. The DMD enables wavefront modulation at 24 kHz by encoding binary amplitude computer generated holograms. To achieve real-time optimization and focusing, FPGA computation is demonstrated. This high-speed wavefront optimization system is applied to light control through multi-mode fibers, which exhibit similar light scattering characteristics to highly scattering materials.

The blind focusing limitation of focusing through turbid media is addressed by photoacoustic feedback. By combining the GA optimization with the photoacoustic feedback the optical fluence is enhanced by a factor of ten. This was extended to high-contrast, three-dimensional photoacoustic image creation by scanning the object behind the scatterer. This photoacoustic optimization technique is analyzed in detail through simulation and further experimentation. Interestingly, the photoacoustic optimization yields a sub-acoustic sized optical focus. This result is explained and discussed, and then utilized in the construction of a super-resolution photoacoustic image.

This thesis is dedicated to Emily and Sam.

ACKNOWLEDGMENTS

The successful completion of this work would not have been possible without the countless individuals who supported me throughout graduate school or contributed directly to this work. I am appreciative to all who encouraged and supported me along the way.

First thanks go to Prof. Rafael Piestun for accepting me into his group and providing me with this opportunity. He has proven to be a vast source of ideas and knowledge; he would always have a solution when I was lost. I have appreciated the freedom and flexibility he gave me to perform this work, which has allowed me to struggle and grow.

I am grateful to those who contributed to the research presented in this thesis. Dr. Youzhi Li worked with Prof. Piestun to initiate this project. Albert Brown coded the first generation genetic algorithm. Antonio Caravaca-Aguirre initially assisted with the project as a visiting student from Spain. Fortunately, he never went home and became a fantastic partner in this work as we have spent countless hours brainstorming and working together. I must acknowledge Eyal Niv for serendipitously knocking on my door exactly when we needed a hardware engineer. Without his adept reverse engineering and FPGA programming skills the high-speed system would not have been built. Yael Niv deserves recognition for assisting Eyal late into the night as our deadlines approached. The extension to photoacoustic imaging was enabled through a collaborative effort with Prof. Todd Murray and his students Hengyi Ju and Jake Dove.

I am grateful to my funding sources for removing the financial burden and supporting this project. Thanks to CDM/Omnivision for generously funding my first year. The National Science Foundation Integrative Graduate Education and Research Traineeship in Computational Optical Sensing and Imaging (COSI-IGERT) generously funded me through the rest of my education, including an international research rotation in Switzerland. Covidien and the National Academy of Sciences Keck Futures Initiative provided the wavefront shaping project funding.

I have had the privilege of working in and collaborating with many labs throughout graduate school. These have enriched my experience and broadened my perspective of optics research. Carol Cogswell took me in for my first semester research rotation and introduced me to imaging and wavefront coding. Working in Prof. Ivan Smalyukh's lab with Rahul Trivedi and Paul Ackerman was my first experience designing and building an optical setup. Collaborating with Prof. Ofer Levi of the University of Toronto and Iliya Sigal introduced me to speckle and live animal imaging. My international experience working at École Polytechnique Fédérale de Lausanne in Prof. Demetri Psaltis' lab deserves special recognition and appreciation. Not only did I learn of the complexities of a STED microscope while struggling to build one with Grégoire LaPorte, I did so while enjoying the intricacies of living abroad in Switzerland.

I would like to thank my fellow students who began this adventure with me in 2008, including Eric Dudley, Kevin Gemp, Kevin Zekis, Betsy Hall, Qing Chao, and Tony Barsic. Thank you for helping me through our challenging courses, such as those taught by Prof. Kelvin Wagner which I found especially mind expanding. I am particularly grateful to this group for helping me prepare for the preliminary examination. I also need to thank other students in the optics group for their friendship and stimulating conversations, namely Adam Urness, Darren Forman, Ramzi Zahreddin, and Dan Feldkhun.

I am grateful to all of the members of the Piestun group for their camaraderie and thought-provoking group meeting discussions. These members have included Dr. Ariel Libertun, Sri Rama Prasanna Pavani, Tim Gerke, Sean Quirin, Ginni Grover, Anurag Agrawal, Jer Brown, Tony Barsic, Antonio Caravaca-Aguirre, Eyal Niv, Haiyan Wang, and Liang Xu.

I would also like to acknowledge Prof. Juliet Gopinath for mentoring me while I was her teaching assistant, as well as providing me the opportunity of teaching and administering the Science Discovery Electromagnetic Waves course in 2012.

Most importantly, I am grateful for love and support from my family. I am deeply appreciative to my parents for opening my eyes to the wonders of the world and motivating me to do hard things. I am especially grateful to my wife Emily for her encouragement and companionship which have buoyed me up and carried me through this journey. She has traveled this path with me and I will be forever grateful to have her by my side. Finally, thanks to my son Sam who, despite attempting to sabotage my preliminary examination, has provided me with an elevated sense of joy in life.

CONTENTS

TABLES

FIGURES

CHAPTER 1

INTRODUCTION

Scattered light limits imaging visibility through, among other things, fog, murky water, walls, and biological tissue. In the realm of imaging in the human body, even as new technologies develop, scattered light continues to confound the ability to look deep into human tissue optically. Finding new ways to look through scattering media has inspired scientists for decades to invent an assortment of clever optical imaging techniques. However, none of these have overcome the limitations imposed by multiple scattering to image at optical resolutions deep in tissue. In recent years, a variety of new methods have emerged which show promise in finally solving the multiple scattering imaging problem. In this thesis, new techniques are explored and expanded upon to enable light control in and through scattering materials, specifically in enabling high-speed and blind wavefront optimization for imaging through a scattering material.

1.1 Multiple Scattering

When a wavefront propagates through a flat piece of glass, the light wavefront maintains its shape. As a result, our eyes are able to see clearly an object placed behind the glass. If the glass was ground into a fine powder it would essentially hide the object that lies behind it. This is

a result of the photons undergoing multiple scattering events and scrambling the incident wavefront; which is the same optical effect that causes occlusion in fog, a glass of milk, and white paint.

Scattering, in the simplest terms, is the deviation of a photon from a straight path caused by propagation medium inhomogeneities. When an optical wavefront enters a highly disordered sample individual photons begin to scatter. A highly scattering medium causes multiple scattering events per photon.

The photon propagation through a group of randomly distributed scatterers, or disordered medium, can be described by diffusion theory, which describes photon paths as performing a random walk. Diffusion theory predicts the relative intensity of the propagated field dependent on the distance between scattering events, or the mean free path of a photon, l, of the sample. Assuming negligible absorption the mean free path is:

$$l = \frac{1}{\mu_s}, \tag{1.1}$$

where μ_s is the scattering coefficient of the scattering material and is defined as:

$$\mu_s = \rho\sigma. \tag{1.2}$$

ρ is the density of the scatterer and σ is the scattering cross section of a single scatterer.

An important factor to consider in a scattering material is the strength or direction of the scattering. The anisotropy function, g, expresses the degree of forward scattering in the material. The transport mean free path, l^*, of the scattering material takes the anisotropy into account to provide the distance at which the beam is completely diffuse:

$$l^* = \frac{1}{\mu_s(1-g)}. \tag{1.3}$$

The transport mean free path also explains how the intensity of the ballistic, or unscattered, light moving through the sample exponentially decays as it scatters and the field becomes more diffuse:

$$I = I_0 e^{-z/l^*}. \tag{1.4}$$

With this construct the photon diffusion equation, which explains the total light distribution, both diffuse and ballistic, through the scattering sample can be introduced as:

$$\frac{\partial U(r,t)}{dt} = D\,\nabla^2 U(r,t), \tag{1.5}$$

where *U(r,t)* describes the light energy density and *D* is the diffusion coefficient which expresses the strength of the scattering in terms of the transport mean free path:

$$D = \frac{l^*}{3}. \tag{1.6}$$

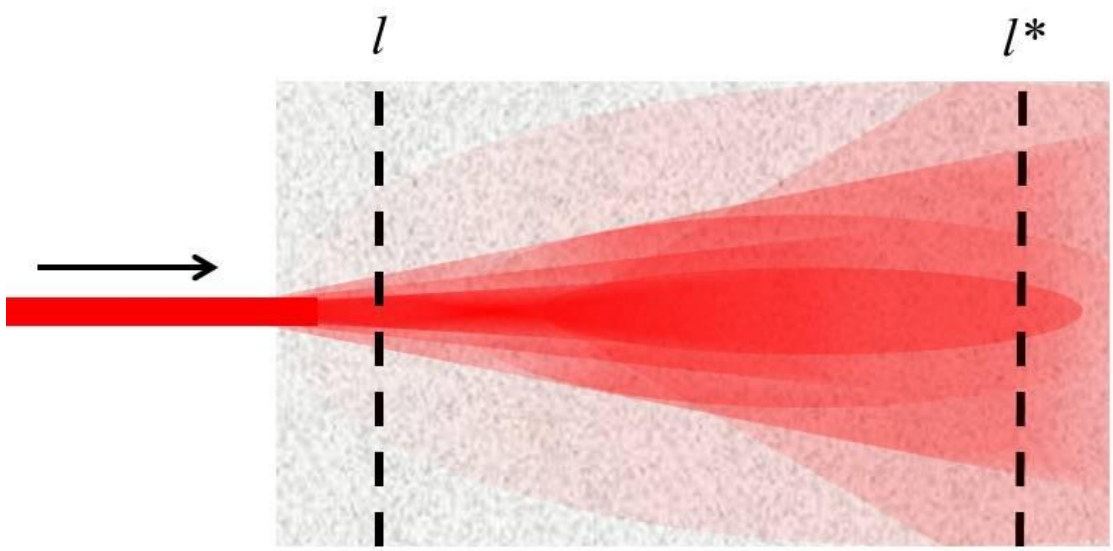

Figure 1.1. Illustration showing how light intensity and distribution change as a wavefront propagates through a turbid material based on the mean free path, *l*, and the transport mean free path, *l**.

Figure 1.1 provides an illustrative representation of how light transport becomes less intense and broadens as it becomes scattered through a sample. Within the depth of the mean free path, *l*, very little scattering has occurred. As the light propagates beyond the mean free path the light distribution broadens and the peak intensity decreases. At the transport mean free depth, *l**, the light has become completely diffuse and the photons propagate in random directions.

Concerning conventional imaging techniques, if the propagating wavefront contains ballistic photons, these can be used to form an image through the scattering layer. At increasing depths the number of ballistic photons decreases until it is insignificantly small. In this diffusive regime information about the object behind the scatterer is completely scrambled.

While diffusion theory expresses the intensity attenuation and spatial energy distribution of light propagation through turbidity, it does not account for important fundamental interference effects caused by coherent photons[1], [2]. In this case the wave equation better describes the light propagation:

$$\nabla^2 E - \frac{n^2(r)}{c^2}\frac{\partial^2 E}{\partial t^2} = 0, \tag{1.7}$$

where *c* is the speed of light in a vacuum, *n(r)* is the index of refraction of the medium, and the wave properties are described in *E*, the electric field. Wave propagation through multiply scattering materials is a complex problem which has been described in detail through systems of linear equations combining multiple scattering processes[3], [4]. In these derivations the scattering problem is first described through single scattering events and extended toward multiple scattering.

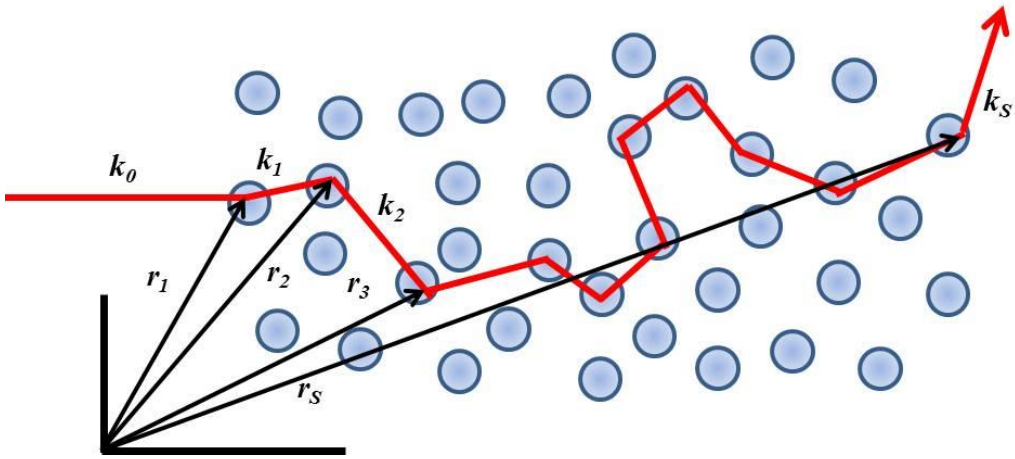

Figure 1.2. The scattering path of a wave through a group of scattering particles. The phase of the wave upon emerging from the group of scatterers depends on the total path length.

Here a simple mathematical description of light propagation through scattering materials is extended and the interested reader is referred to [3] and [4] for more exhaustive derivations. Figure 1.2 illustrates how a wave may propagate through a group of scattering particles. As it encounters different scatterers its propagation direction, or *k*-vector, is altered due to scattering. The path that the wave takes through the scattering material will ultimately determine its phase upon exiting the material. The total path length, *L*, can be expressed in terms of the distance between scattering event positions, *r*:

$$L = \sum_{s=0}^{S} \left| r_{s+1} - r_s \right| = \sum_{s=0}^{S} \frac{k_s}{\left| k_s \right|} \bullet \left(r_{s+1} - r_s \right). \tag{1.8}$$

S is the total number of scattering events. As a result the phase of the wave after multiple scattering is:

$$\phi(t) = k_0 L(t) = \sum_{s=0}^{S} k_s(t) \bullet \left(r_{s+1}(t) - r_s(t) \right). \tag{1.9}$$

When the wave described in the previous paragraph is a part of a wavefront containing a large number of photons. Each individual photon will travel a unique path through the group of scattering particles. As such the electric field, E^{out}, at an arbitrary point on the transmission side

of the scatterers is a summation of the photons which travel p paths and coherently combine at that point:

$$E^{out}(t) = \sum_{p} E_p e^{i\phi_p(t)}. \tag{1.10}$$

The electric field, E_p , refers to the amplitude contribution to the field from path p.

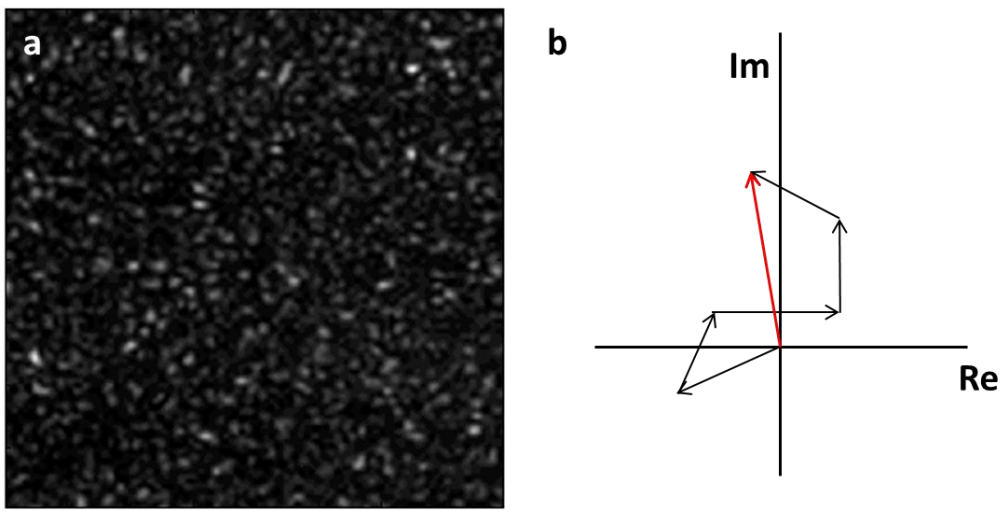

Figure 1.3. (a) A speckle field created by coherent light scattering. (b) The intensity of any output mode in the speckle field is determined by a random walk.

As the light field propagates through the scattering layer the incident photons travel different paths and consequently significantly different path lengths. Thus, on the transmitted side of the scattering layer the light field contains photons which are traveling along a wide range of directions, with different relative phases. As these coherent photons interact, they constructively and destructively interfere forming a speckle field (Figure 1.3(a)). At any output mode, E^{out}, the amplitude is determined by a random walk, or the summation of every path's random amplitude and phase contribution to that mode (Figure 1.3(b)). The resultant sum amplitude depends on whether constructive or destructive interference dominates[6]. As a result the output intensity field consists of bright and dark spots and is called a speckle field.

Figure 1.4. The scattering matrix relates the fields incident on a scattering layer (a^+ and b^-) and the fields propagating away from it (a^- and b^+).

Random matrix theory provides a different framework to describe light-wave propagation through a turbid, or highly scattering, layer and account for interference effects. The scattering matrix does not account for the physical path photons travel through a sample, but rather quantifies the complex relationship between spatial modes incident upon and exiting a scattering layer. Specifically, the scattering matrix is a $2M \times 2N$ matrix which relates input fields to output fields (Figure 1.4) through a random material[5]:

$$\begin{pmatrix} a^- \\ b^+ \end{pmatrix} = \begin{pmatrix} r & t' \\ t & r' \end{pmatrix} \begin{pmatrix} a^+ \\ b^- \end{pmatrix}. \tag{1.11}$$

The sub-matrices in the scattering matrix represent the reflection matrices (r and r'), and the transmission matrices (t and t'). These relate the incident electromagnetic fields, a^+ and b^-, to the resulting fields propagating away from the scattering layer, a^- and b^+ (Figure 1.4). These fields include N and M spatial modes for the a and b fields, respectively. The modes may be any set of orthogonal modes which represent the basis vectors of the scattering matrix.

The studies conducted within this thesis are concerned with light transmission through a scattering layer. Thus, the scattering matrix formulation used imposes light propagation only from the left to the right as shown in Figure 1.4. The light field transmitted through a scattering layer can then be expressed as:

$$b_m^+ = \sum_{n=1}^{N} t_{mn} a_n^+ . \tag{1.12}$$

Where b_m^+ is the electric field at output mode *m*, a_n^+ is the electric field at input mode n, and t_{mn} is the transmission matrix element relating input mode *n* to output mode *m*. In this way random matrix theory accounts for interference effects with a transmission matrix in a similar formulation to Equation 1.10.

1.2 Imaging through scattering media

To overcome scattering through turbid media a variety of imaging modalities have been developed. Many of these overcome optical scattering by using non-optical detection methods. For example, ultrasound imaging is an important medical diagnostic tool[7]. Acoustic waves exhibit three orders of magnitude less scattering in biological tissue than optical waves, enabling deep tissue imaging[8]. However, acoustic imaging differs from optical imaging in that its contrast mechanism stems from elastic and density properties of the material and more importantly can produce only moderately resolved images. Many other imaging methods take advantage of different scattering properties along other bands of the electromagnetic spectrum[9], including passive millimeter wave imaging through fog or clothing and X-ray radiography which utilizes an X-ray photons ability to penetrate through tissue with minimal scattering. Despite these capabilities, optical methods are still desirable because of the potential resolution and the vast and unique information the visual spectrum provides. Optical methods are safe, non-ionizing, noninvasive, and cost effective. In addition, most of the analytes of interest in tissue contain absorption bands in the visible and near Infrared portions of the spectrum that provide high contrast between the analytes and the background. Some potential light control through scattering media applications include biomedical imaging and sensing[10], fluorescence

imaging[11], [12], photodynamic therapy[13], neuron excitation and imaging[14], art preservation[15], and photonic crystal fabrication[16].

1.3 Early holographic methods for imaging through scattering media

Shortly after the invention of the laser, holographic methods were applied to imaging through scattering media. Leith and Upatnieks first proposed recording a scattered wave field holographically in 1962[17]. Then, by phase conjugation of the recorded field and back propagation through the inhomogeneous material the distortions would be corrected, as illustrated in Figure 1.5. They first demonstrated this optical phase conjugation (OPC) technique in 1965[18], [19] to reconstruct a high-quality image, despite propagating through a ground glass diffuser. Shortly afterward Goodman et al. demonstrated a holography technique which relied on an object's waves interfering with a mutually coherent point source of light after both propagated through a scatterer[20]. They observed that when the object and point source waves pass through highly correlated sections of the scatterer, the interference pattern was unaffected by scattering which allowed image reconstruction without back-propagation through the scatterer. Later, Chang and Leith reported a technique for imaging through scattering layers with incoherent light using an achromatic interferometer[21].

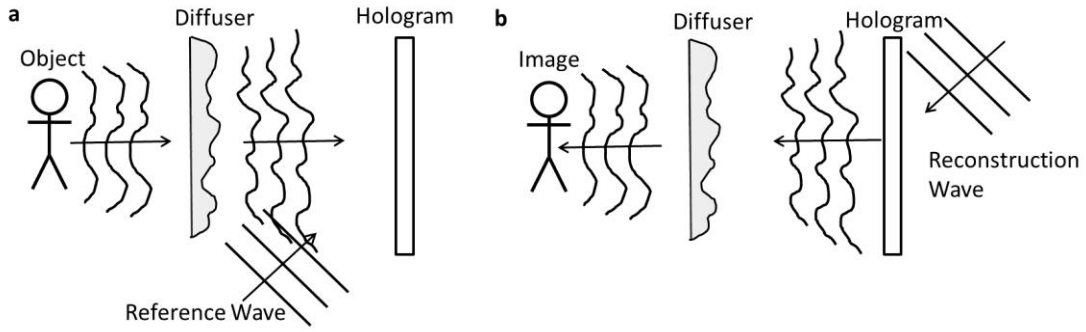

Figure 1.5. Illustration showing Leith's and Upatniek's original phase conjugation method for image recovery through a diffusing layer. (a) Recording a hologram of a scattered wave field. (b) An image of the occluded object is reconstructed after phase conjugation of the recorded field.

After the initial demonstrations of imaging through diffuse glass, significant work on imaging through scattering media with holography turned to imaging through fog. In 1967 Spitz and Stetson independently demonstrated imaging through fog by filtering out scattered light with holography[22], [23]. These demonstrations relied on moving fog particles imparting random frequency shifts on the scattered light due to the Doppler effect. Thus, the scattered light field became incoherent and only the ballistic photons interfered with the reference wave. In 1978 Lohmann and Schmalfuss reported a new version of imaging through fog with on-axis holography[24]. Subsequent reports showed interferometric methods of imaging through fog with one-way phase conjugation[25] and achromatic interferometers[26], [27]. These holographic applications demonstrated the possibility of imaging through turbid media, although no practical technique was developed.

1.4 Current methods for optical imaging through scattering media

The last half of the 20th Century saw the development of a vast array of imaging techniques to minimize the effects of scattering[28]. Many of these are based on the interferometric principles utilized in the early holography work. These imaging modalities are based on filtering out scattered light, like Spitz and Stetson[22], [23], or using scattered light to image inside of scattering materials. These modern imaging techniques include spatial filtering of scattered light, time-gating, coherence-gating, speckle contrast imaging, photoacoustic, and adaptive optics methods.

1.4.1 Spatial filtering

Of these imaging techniques, spatially filtering a wide-field transmission is perhaps the most straightforward technique for removing scattered light. This method is best understood by considering the angular variation imparted on scattered light as opposed to ballistic light. By

implementing a spatial filter at the back Fourier-transform plane of an objective lens, scattered photons which are out of line with ballistic photons are filtered[29], [30] (see Figure 1.6).

The most frequently utilized method for spatial filter reduction of scattered light is scanning confocal imaging[31]. In this method, instead of illuminating a wide-field of view, a tightly focused laser beam scans inside a scattering sample. A pinhole placed at a conjugate plane to the laser focus limits the collection to light which has been illuminated within the focus. This method provides an optical sectioning capability and is flexible enough to have been implemented in a variety of modalities, including reflection, transmission, fluorescence, differential interference, and phase contrast imaging[31]. Confocal imaging has been implemented extensively and remains a leading tool in science and industry. However, the technique is still limited to samples in which a significant number of ballistic photons can be collected. Thus, the depth of imaging in biological tissue samples is limited to the ballistic regime which is less than one millimeter.

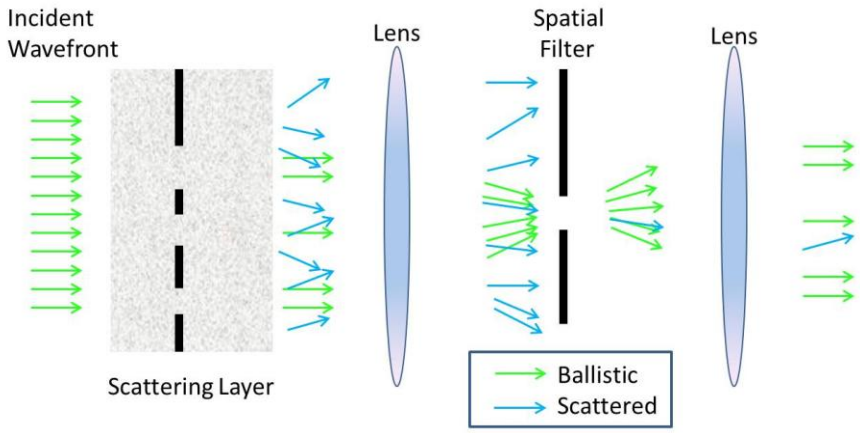

Figure 1.6. Spatial filtering to isolate ballistic photons. After propagating through a scattering layer most scattered photons do not propagate along the same path as ballistic photons. By implementing a spatial filter most scattered photons are filtered, thereby increasing the signal to background ratio of the ballistic photons.

1.4.2 Time-gating

Collecting early arrival photons, or time-gating, through a scattering sample provides another method for discriminating scattered photons. As depicted in Figure 1.7, by traveling a straight course, ballistic photons travel faster than scattered photons through a scattering material. Through selective detection of these early arrival photons, the scattered photons can be filtered. This requires temporal discrimination faster than 1 ps[28], which is much faster than typical photodiode and photomultiplier response times. However, the fastest photodetectors have been used to capture ballistic photons, in addition to some slightly scattered photons, to significantly improve image resolution by filtering out the most strongly scattered photons[32]. Short pulsed lasers combined with fast photodetectors can be effective time-gates and have been used for imaging through turbid water[33].

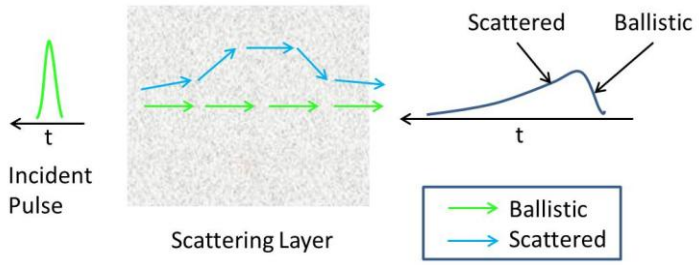

Figure 1.7. Scattered photons travel a greater distance through scattering layers than ballistic photons. Time-gating uses this principle to selectively detect early-arriving ballistic photons.

Laser pulses in conjunction with nonlinear optical effects provide an effective tool for time-gating. With these tools the scattered light is rejected by three means. First, the scattered light intensity is too low for nonlinear processes. Second, by exploiting nonlinear effects which require the interaction of two beams, a short pulse effectively time-gates the signal. Third, the strict nonlinear crystal acceptance angle requirement simultaneously spatially filters the signal for additional discrimination[34], [35]. This has been demonstrated with stimulated Raman scattering[36], parametric amplification[34], and the optical Kerr effect[35].

1.4.3 Coherence-gating

The coherence properties of lasers provide another mechanism for discriminating against scattered light. As discussed above, Spitz and Stetson demonstrated coherence-gating to image through fog[22], [23]. Today the most widely used form of coherence gating is optical coherence tomography (OCT). As an example, one type of OCT uses interferometry between light back-reflected from a scattering sample and light reflected in a reference arm, see Figure 1.8. By using a low coherence laser this technique effectively discriminates light incoherent to the reference. By scanning the reference arm path length the depth of the coherent back-reflection varies, thus providing axial discrimination. OCT has been developed in multiple modalities, including time-domain, frequency domain, Fourier domain, and swept source[28], [37]. OCT is now a major biomedical tool in imaging applications for dermatology, eye imaging, and ophthalmology.

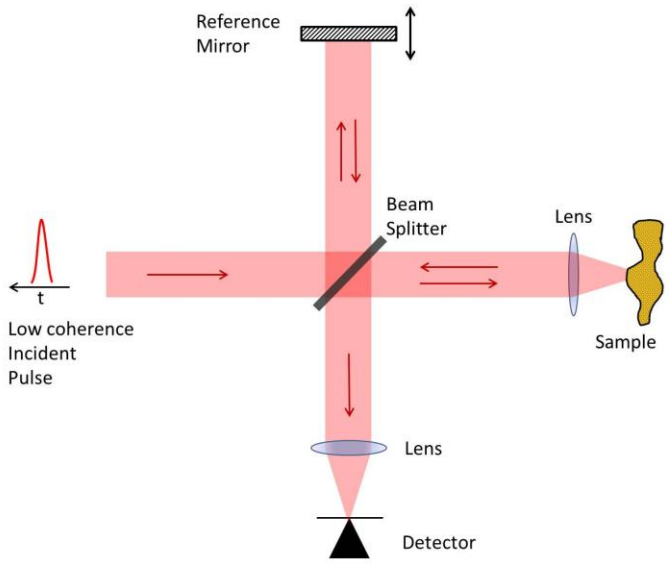

Figure 1.8. Basic OCT setup. A low coherence pulse is split into reference and sample paths. The sample path collects light backscattered in the sample. Interference between the reference and the sample arm provides axial discrimination by scanning the reference arm.

1.4.4 Optical projection tomography

Optical projection tomography is another technique which has been used for imaging inside of scattering materials[38]. By propagating light through the sample using multiple angular projections and measuring the intensity pattern exhibited after propagation, a map of the occluding or absorbing structures within are recreated through tomographic reconstruction algorithms. Often, optical projection tomography relies on chemical treatment of the sample to reduce the scattering of light; unfortunately such treatments make live-animal imaging impossible. The resolution achievable with this technique worsens as the thickness of the sample increases, thus diffraction limited imaging is not possible beyond the ballistic regime.

1.4.5 Laser speckle contrast imaging

Laser speckle contrast imaging is another technique which uses scattered light for image formation[39]. The laser speckle pattern created by tissue at any point in time depends completely on the structure of the inhomogeneities within the tissue. Light scattered by blood cells flowing within vessels causes this speckle pattern to vary with time. When this speckle image is imaged with a finite exposure time, the captured speckle pattern blurs. The resulting contrast provides information about the structure of blood vessels[40] and also about the blood flow velocity[39], [41].

1.4.6 Photoacoustic microscopy

Photoacoustic microscopy varies from the previously mentioned modalities in that it creates images based on optical information, but uses acoustic detection for image reconstruction. The photoacoustic effect, as first observed by Alexander Graham Bell[42], is the production of an acoustic wave after a medium absorbs light and undergoes thermal expansion. By shining light into a scattering medium, diffuse light absorbed in the material will generate

acoustic waves as illustrated in Figure 1.9. This method differs from ultrasound imaging in that its contrast stems from optical absorption as opposed to mechanical properties. The photoacoustic effect is used in modern photoacoustic microscopy to image in tissue at depth[43]. While photoacoustic microscopy uses optical contrast the resolution is acoustically limited when imaging beyond the ballistic regime.

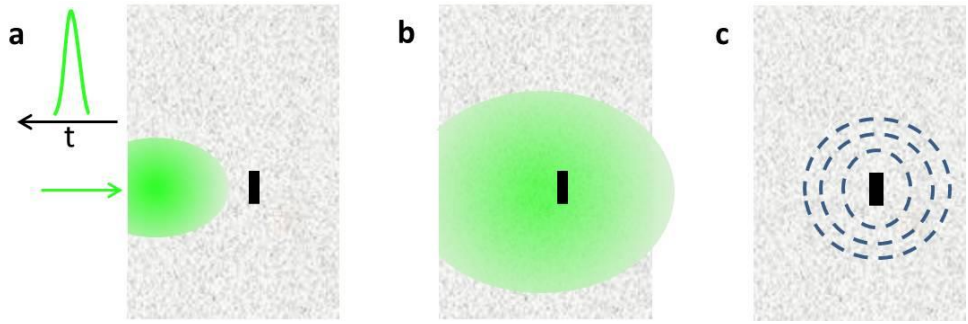

Figure 1.9. Illustration of photoacoustic effect. (a) A light pulse enters a scattering material and subsequently diffuses. (b) The diffuse light field propagates through an absorbing object. (c) The absorption causes thermal expansion of the object which creates an acoustic wave, which can be detected to reconstruct an image of the absorbing objects.

1.4.7 Adaptive optics

Adaptive optics corrects for aberrated wavefronts and is used in astronomy to obtain higher resolution imaging when viewing through atmospheric turbulence. This technique was first envisioned in 1953[44], but didn't become a reality until the 1990s when computational power was suitable for the task[45]. Adaptive optics uses a deformable mirror to correct for the aberrations introduced by turbulence in the atmosphere which is possible for astronomy because of the low number of spatial modes required to correct for the atmospheric turbulence aberrations. Adaptive optics has also been implemented to correct for lower order aberrations within the ballistic regime in biological imaging[46], however it cannot optimize beyond the ballistic regime due to the large number of spatial modes presented by highly scattering media.

Despite this progress in higher resolution imaging into a scattering medium, there is still no method for imaging deep into scattering layers with multiply-scattered light at optical resolutions.

1.5 Focusing through turbid media

In 2007 Vellekoop and Mosk introduced a method for controlling light propagation through scattering media and consequently reignited interest in imaging through highly-scattering materials[47]. This technique was enabled by the introduction of and the subsequent advances in spatial light modulator (SLM) technology. In this technique the wavefront incident on the scattering media was divided into N spatial modes providing N degrees of control over the light field incident on a scattering layer and consequently on the speckle field (Figure 1.10(a) and (b)). Each spatial input mode contributes independently to each spatial output mode; this relationship is described in the transmission matrix formulation:

$$E_m = \sum_{n=1}^{N} t_{mn} A_n e^{i\phi_n}. \tag{1.13}$$

Where E_m is the electric field at output mode m, A_n and ϕ_n are respectively the amplitude and phase of input mode n, and t_{mn} is the transmission matrix element relating input mode n to output mode m. By modulating the input mode phase, ϕ_n, the respective phase of all N mode contributions can constructively interfere at output mode m (Figure 1.10(c) and (d)). Assuming uniform illumination at the input modes, $A_n = 1/\sqrt{N}$, the resulting intensity of the optimized output mode is:

$$I_m^{opt} = \frac{1}{N}\left(\sum_{n=1}^{N} |t_{mn}|\right)^2. \tag{1.14}$$

Considering that the elements of t have a Gaussian distribution[6], [48], the intensity enhancement, or intensity increase over the average output mode intensity, of this mode is[49]:

$$\eta = \frac{\pi}{4}(N-1)+1. \tag{1.15}$$

Interestingly, the size of this optical focus is independent of the optical system before the scatterer and will be the size of a speckle grain, which depends on the scattering properties[50].

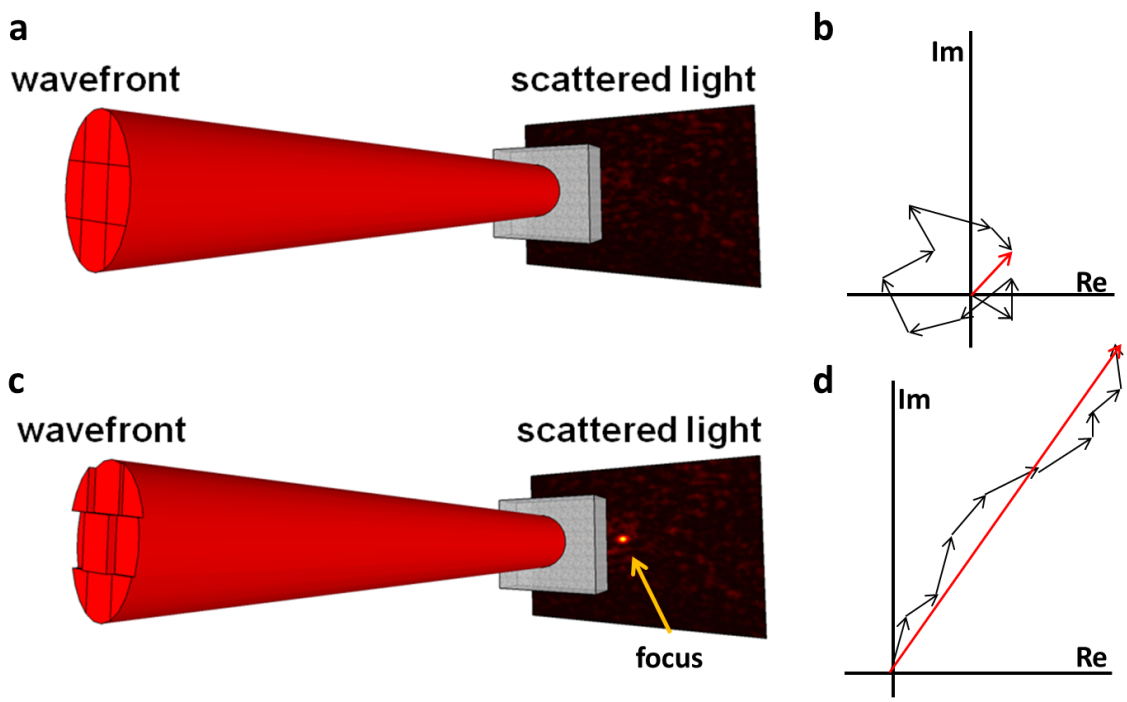

Figure 1.10. (a) The spatial input modes all contribute to the speckle field creation upon propagating through a turbid layer. (b) The random walk created from the random phase and amplitude contributions from each spatial input mode determines each individual speckle grain's intensity. (c) and (d) By optimizing the phase of the input modes to constructively interfere at an output mode, a high intensity focus is created.

The introduction of this method led to an assortment of algorithms for wavefront optimization[49], [51], [52] and a method to measure the transmission matrix through a scattering material[53]. In this technique the transmission matrix between N Hadamard basis input modes and M output modes was measured using phase shift interferometry. Importantly,

the reference wave passed through the scattering material, which provided a fixed speckle intensity spatial distribution for interferometry. This enabled measuring the phase of each scattered basis element at all M output modes. The measured transmission matrix provides the information necessary to create a focus at any output mode using phase conjugation of the measured matrix[54].

The iterative wavefront optimization techniques are mathematically equivalent to OPC through turbid media, as originally introduced by Leith and Upatnieks[17]. As such, shortly after the introduction of the iterative optimization technique, Yaqoob et. al. began experimenting with OPC through tissue samples using photorefractive crystals[55], [56]. Eventually, this led to the development of a digital optical phase conjugation (DOPC) method, in which an SLM and a detector array are placed in conjugate planes[57]. DOPC eliminated the nonlinear optical process constraints placed on the light source and media for phase conjugation by removing the photorefractive crystal from the apparatus[57].

All of these light control techniques rely on the deterministic nature of scattering. In 1990, Freund theorized that deterministic scattering implies that the scattered waves still contain important image information and the scattering material could essentially be used as a high precision optical instrument[58]. The transmission matrix measurement technique confirmed that the scattered light field contains image information. After measuring the transmission matrix through a scattering material, a phase image was displayed on the wavefront encoding SLM. Using the transmission matrix and the measured speckle field the image was recovered despite the image information being completely scrambled[59].

Freund’s work was further validated by Katz et al. who demonstrated how a scattering layer could be used as a lens and a mirror[60]. In this demonstration a point source was placed

some distance away from a diffuse glass. The light that scattered through the glass diffuser propagated to an SLM, which reflected the light to a lens and a detector array. In this way the experiment demonstrated wavefront optimization by correcting a light field after scattering, as opposed to previous techniques which pre-compensated for scattering. With the optimized wavefront encoded on the SLM, transparent objects were placed in the same location as the point source. The wavefront correction allowed these objects to be imaged onto the CCD, despite the diffuser. A similar demonstration took place for light scattered off of a piece of paper. By imaging with a scattering layer as an element in the optical system, these experiments displayed the ability of the scattering materials to act as lenses or mirrors.

The role of spatial wavefront shaping to control ultrashort pulses through scattering media was also investigated with interesting results[61]–[63]. Katz, et al. used a genetic algorithm optimization to enhance the two-photon fluorescence signal resulting from the interaction of a scattered light field and a nonlinear material[61]. By simply optimizing the spatial input modes before the scattering sample they observed that the pulse shape was optimized both spatially and temporally. Aulbach et al. had similar results by using heterodyne interferometry as feedback, which provided additional temporal control of the pulse[63]. In the third demonstration, McCabe et al. measured the spectrum of the scattered optical field then shaped the wavefront spatially to control the pulse focus in both space and time[62].

1.5.1 Speed

An important field in which focusing through turbid media could make a significant impact is in biomedical imaging. Biological tissue presents a moving target optimization challenge because it is dynamic. As blood or other cells move in tissue, the path photons travel changes, thus the scattering matrix changes. The rate at which the matrix evolves depends on the

type of tissue and the penetration depth, but it can be as low as a few milliseconds. The first demonstrations of focusing through turbid media utilized liquid crystal SLMs for wavefront shaping. The liquid crystal limits the modulation speed of these devices to 10s or 100s of Hz. In fact, focusing through living tissue was demonstrated early on with an iterative focusing technique[64] and OPC[55], [56]. However, in these demonstrations the rate of tissue change was slow, on the order of seconds. To enable focusing through more dynamic tissue the first attempts to increase the optimization time were algorithmic and based on parallel mode optimization[49], [51], [52]. Shortly after, new measurement schemes were introduced[65] and new wavefront shaping devices implemented[66], [67].

1.5.2 Blind focusing

A requirement for imaging through turbid media to be feasible in biomedical imaging is the ability to focus into or through a scattering layer without access to the backside. The original iterative focusing experimental setups placed a detector on the transmission side of the scattering material[47], [53]. Such a setup could not be implemented in a biomedical application and has resulted in a sustained effort to introduce methods to overcome this limitation. Vellekoop and Mosk demonstrated focusing inside a scattering material by embedding fluorescent particles sparsely inside of the turbid medium[68]. The feedback signal used in optimization measured the total fluorescent emission intensity coming from within the scatterer. A key to this method was the assumption that the fluorescent beads were well separated. Hsieh et al. introduced a similar technique for OPC, but used a nanoparticle which emitted a second harmonic generation (SHG) field and thus maintained its coherence[69]. The scattered field was then measured holographically and phase conjugated to return a focus to the nanoparticle through the scattering layer.

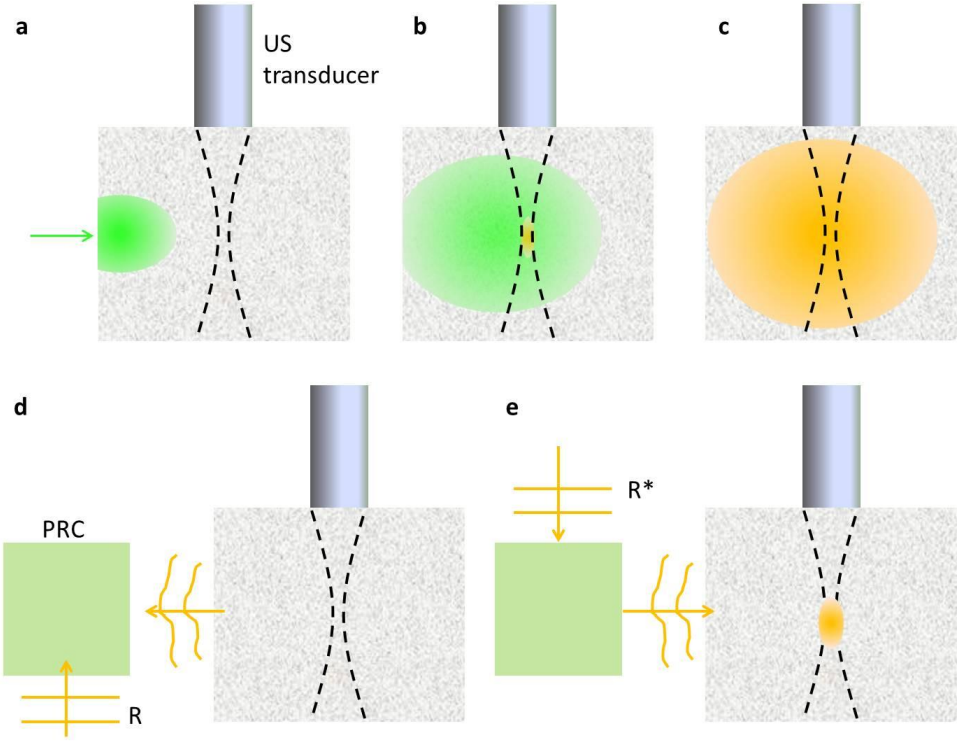

Figure 1.11. Light control through turbid media with ultrasound guidestar. (a) Coherent laser light enters a turbid material. (b) After propagating through the sample the light interacts with the focused acoustic wave. (c) Photons that travel through the ultrasound focus are frequency shifted and propagate. (d) The scattered photon-tagged field is recorded in a photorefractive crystal (PRC). (e) The recorded hologram is read out to create the conjugate beam, which returns light to the ultrasound focus.

Several different demonstrated techniques have recently overcome this limitation using acoustic waves, either with an ultrasound guide-star or a photoacoustic feedback. Acoustic waves are an appealing feedback mechanism for wavefront optimization in tissue, because their penetration depth is much greater than optical waves and they are not distorted by significant scattering. In the first demonstration Xu et al. tagged photons which passed through an ultrasound focus by frequency modulation as shown in Figure 1.11(a) and (b)[70]. The optical field of the tagged photons was recorded upon emerging from the scattering material (Figure 1.11(c) and (d). Light returned to the acoustic focus inside the scattering medium after OPC

using the recorded field (Figure 1.11(e)). Two subsequent modifications of this ultrasound guide-star method have allowed for the creation of a sub-acoustic resolution optical focus[71], [72]. In one method the spatial profile of the ultrasound transducer is used to encode photons and decrease the focus spot size[71]. By iteratively phase conjugating light towards the ultrasound focus, the Gaussian-shaped ultrasound wave more strongly photon-tags the center photons thereby increasing the optical intensity in a sub-acoustic focal region.

In a second method, introduced by B. Judkewitz et al.[72], an ultrasound guide star is used for photon tagging. The light incident on the turbid material is randomly phase modulated and the resultant photon-tagged scattered field measured for many random wavefronts. This process is then repeated for three additional, neighboring ultrasound guide star positions. The variance of a single output mode contribution in the speckle field depends on its location in the Gaussian shaped ultrasound focus. By measuring the variance with several ultrasound focus locations the output modes in the ultrasound transducer focus can be decoupled and the conjugate phase mask calculated to focus to a single, near speckle sized optical focus. While these methods are promising, complex optical set-ups and low SNR could limit implementation.

Photoacoustics, where acoustic waves are generated from optical absorption and subsequent thermal expansion, can also be used for wavefront optimization[73]–[76]. In this case, the pressure of the generated acoustic wave is proportional to the optical fluence. Thus, the photoacoustic signal can be used as feedback in iterative optimization algorithms[73]. The transmission matrix has also been measured using a photoacoustic feedback, in so doing the relationship between the spatial optical input modes and the detected photoacoustic signals was described[74].

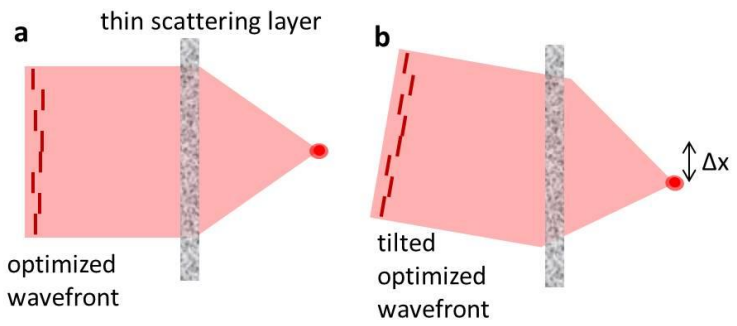

Figure 1.12 . Memory effect focus scanning through turbid media. (a) With an optimized wavefront a focus is created behind the scattering layer. (b) When the scattering layer is sufficiently 'thin' the focus can be transversely shifted by tilting the incident wavefront.

1.5.3 Imaging

The blind focusing techniques have been extended to enable imaging behind scattering materials. Vellekoop and Aegerter first demonstrated imaging behind a scattering layer by optimizing onto a focus with access behind the layer, although, their method could be extended to blind focusing[11]. After optimization the authors used the memory effect to scan the optimized focus and create an image. The memory effect relies on the scattering behavior through a thin turbid layer having high angular correlations[77], [78]. In other words, small tilts of the incident beam do not change the speckle pattern, but impose a spatial shift, thereby allowing an optimized focus to be scanned (see Figure 1.12). SHG nanoparticles were also used in a similar way to create an optical focus scanned by the memory effect[79], [80]. An iterative optimization technique implemented in a two-photon fluorescence microscope extended the imaging depth and improved the contrast[81]. The ultrasound guide-star techniques have also been extended to imaging applications by imaging fluorescent particles embedded in a scatterer[12], [82]. The sub-acoustic, ultrasound tagging optical focus techniques have been utilized in image reconstructions as well[71], [72]. In these implementations the ultrasound guide star is scanned through the sample and the iterative OPC performed for optical focus creation.

Thus, the fluorescence excitation detected at each ultrasound focus point can be reconstructed for image formation.

1.6 Main contributions of this thesis

In this thesis, new iterative wavefront optimization techniques are applied to overcome speed and blind feedback limitations in controlling light through scattering media. In Chapter 2 a genetic algorithm for wavefront optimization is demonstrated both in simulation and experiment. The genetic algorithm enables parallel mode optimization, which speeds up the optimization procedure. These results show that the genetic algorithm is more robust in low signal-to-noise (SNR) environments than other optimization algorithms. The low SNR performance is critical to high speed performance, because SNR decreases with the integration time. This algorithm is extended towards image projection through scattering layers using wavefront shaping in Chapter 3. For this application the genetic algorithm cost function is customized to the task and a Bayer-filter RGB camera is used for three color light control, which enables full color image creation with color mosaicking.

A novel wavefront shaping technique using a binary amplitude Digital Micromirror Device (DMD) is demonstrated in Chapters 4 and 5. The original focusing through scattering media experiments used a liquid-crystal SLM for wavefront shaping. These devices are limited in their phase modulation to 10-100 Hz, as discussed above. For many biomedical applications a modulation rate over 10 kHz is necessary to overcome the dynamic turbidity with iterative optimization methods. The DMD enables modulation at 24 kHz. This wavefront optimization system applied to focusing light through multi-mode fibers is discussed in Chapter 5.

The blind focusing limitation of focusing through turbid media is addressed by implementing a photoacoustic feedback system. Chapter 6 describes how using a genetic

algorithm optimization for focusing through turbid media yielded photoacoustic enhancements of over ten. With the optimized focus created, an absorbing sample is scanned behind the scatterer and a three-dimensional image reconstructed. In Chapter 7 this technique is analyzed in detail through simulation and further experimentation. The unexpected result of the optimization yielding a sub-acoustic sized optical focus is presented and discussed. Using this focus a super-resolution photoacoustic image is created, revealing a ten-fold improvement in resolution over the acoustic transducer alone. This represents a significant advance in photoacoustic imaging in scattered media. Chapter 8 presents a summary discussion of this thesis and suggestions for future research directions, while Chapter 9 contains the concluding remarks.

CHAPTER 2

HIGH NOISE RESISTENT WAVEFRONT OPTIMIZATION FOR FOCUSING THROUGH TURBID MEDIA VIA GENETIC ALGORITHM

2.1 Introduction

Recently, focusing light through turbid media has been achieved by optimizing wavefronts via a feedback system and spatial light modulators for wavefront control[47]. The resulting waves overcome the effects of multiple scattering and are capable of producing a focal spot after propagation through the scattering media. These methods have the potential to image deep into biological tissue. However, living tissue has the additional problem of a constantly changing scattering path due to cell movement within, which necessitates a relatively fast optimization. The turbid media focusing systems optimize the incident wavefront by dividing it into N input modes and setting the phase of each mode, using a phase mask, to maximize the intensity of a spot in the output plane. Several phase control algorithms have been introduced to optimize the phase of each input mode[49], [51], [53]. The stepwise sequential algorithm and the continuous sequential algorithm (CSA) optimize each input mode independently and are consequently slow[49]. Furthermore, by modulating a single mode the interference signal detected at the output plane is small, resulting in initial errors in measurement and phase mask

selection that remain until the SNR increases. The partitioning algorithm (PA), on the other hand, modulates and maximizes the interference signal of a randomly selected half of the input modes during each iteration[49], which increases the SNR and causes a faster initial enhancement of the focal spot intensity than the sequential algorithms. However, as the PA progresses the magnitude of enhancement improvement slows and the enhancement approaches the theoretical maximum more slowly than the CSA. This algorithm achieves best performance when the number of input modes is much larger than the number of iterations performed during the sample speckle decorrelation time[49], [64], or the time that the sample remains relatively stable.

Other techniques have been developed to compensate for random multiple scattering. For example, an observed transmission matrix (TM) can be measured and used to create a focus through the medium in the output plane[53]. The observed transmission matrix is measured by calculating the complex field response for a set of given input basis modes. The complex field response is measured by interference between each basis element and known phase reference beams (phase shifted by 0, $\pi/2$, π, and $3\pi/2$) after both propagate through the scattering medium[53]. Optical phase conjugation (OPC) has also been demonstrated for reverse propagation through highly scattering materials[55], [57], [83]. More recently, a method to optimize the input modes in parallel has been introduced[51]. In principle this method has a five-fold reduction in the number of required measurements with respect to the CSA, although more samples were required in the reported experiment to overcome the noisy environments. Hence, this signals to a tradeoff by which longer integration times are required to reduce the number of measurements, which is at odds with time scarce experiments.

Focusing light through scattering materials has potential in various biomedical applications, such as photodynamic therapy[84], fluorescence imaging[11], optical trapping[85], and neuron excitation and imaging[14], [86]. Focusing through turbid biological materials, which typically change on a millisecond timescale, requires faster algorithms. Moreover, the intensity measurements required in these techniques are noisier, due to sample vibrations and lower photon counts as a result of higher frame rates. Therefore, in this chapter an optimization method is introduced to speed up focusing through scattering materials in low signal-to-noise environments. The method uses a genetic algorithm (GA) approach for adaptively optimizing the phase mask. The GA technique increases the focal spot intensity faster than the CSA or PA while being less susceptible to noise errors.

2.2 Genetic algorithms applied to phase mask optimization

A GA is an optimization algorithm which uses principles inspired in nature to “evolve” toward a best solution. GAs are well-suited for large-scale optimization problems[87] and thus attractive to optimize the phase of the N input modes in the focusing task. GAs have been previously used, among many other applications, in optical pattern recognition for optimal filter design[61], [88].

The GA developed for focusing through turbid media begins by generating an initial population of phase masks. Each phase mask is created by selecting each input mode value from a uniform pseudorandom distribution of phase values. Once the population of phase masks is created a cost function for each mask is measured. For this task the cost function is the intensity of a predefined spot in the output plane. The population of masks is then ranked according to the cost function, with a higher intensity receiving a higher ranking.

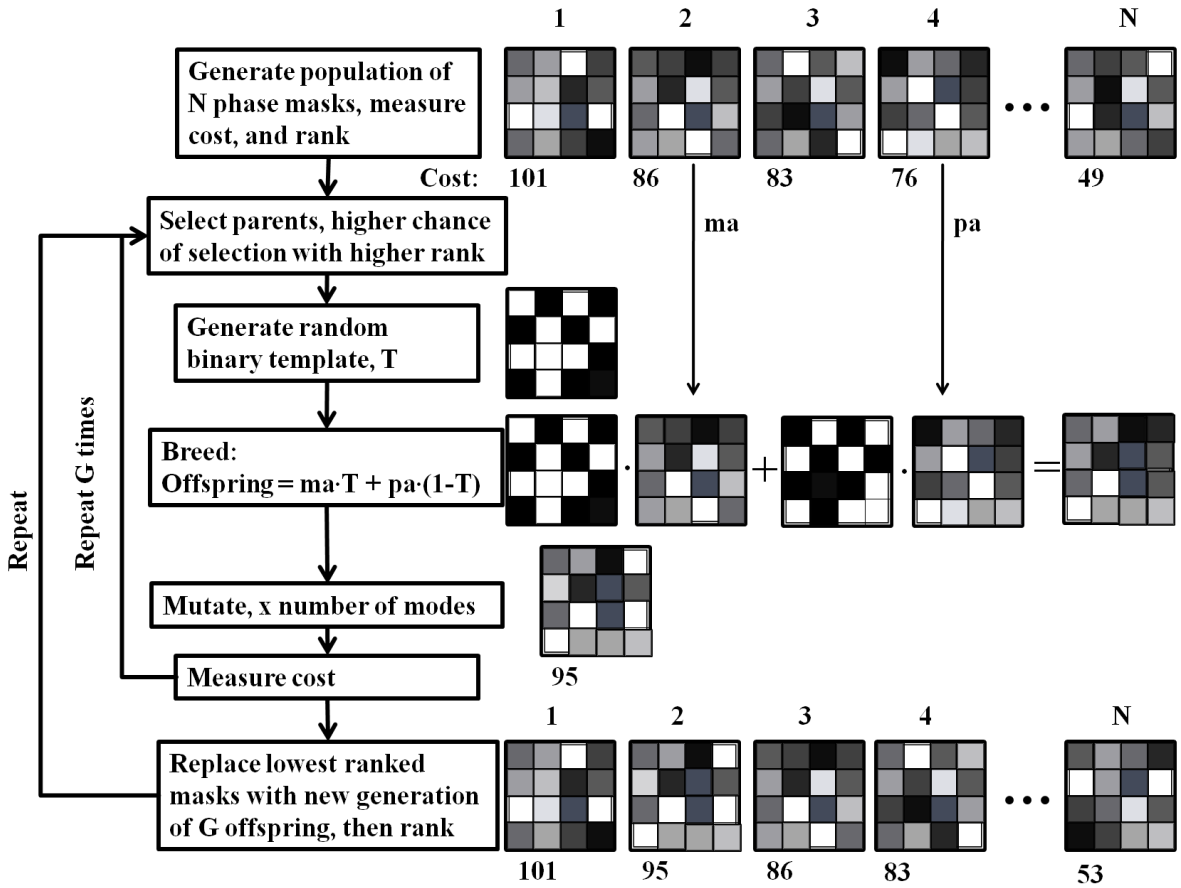

Figure 2.1. A block diagram showing the steps of the genetic algorithm: (1) A population of phase masks is created. (2) The cost function of each mask is measured and the masks ranked. (3) Breeding is implemented, with the breeding parent phase mask being selected with a higher probability if it is higher ranked. The new offspring mask is created by combining the ma and pa masks using the breeding template, T, and mutating x input modes of the new mask. (4) The cost function of this new offspring mask is then measured and used to place it within the population. (5) The process repeats for a certain number of iterations or until a satisfactory solution is achieved.

The algorithm then iteratively optimizes the phase masks through breeding and mutation operations. A random binary breeding template array, *T*, is created before breeding. Subsequently, two parent masks (*ma* and *pa*) are randomly selected from the population for breeding. A higher probability of selection is given to higher ranked phase masks. The input modes of the two parent masks are combined using *T* to create a new offspring according to: $Offspring = ma \cdot T + pa \cdot (1-T)$. This new mask is then mutated by randomly changing the phase of

a set number of input modes. In order to prevent the algorithm from mutating too many optimized phase modes, the percentage of modes mutated, R, decreases as the algorithm runs and nears the optimal phase mask. In this implementation R was determined as $R = (R_0 - R_{end})\cdot exp(-n/\lambda) + R_{end}$. Where R_0 is the initial mutation rate, R_{end} is the final mutation rate, n is measurement number, and λ is the decay factor. The cost function of the offspring is measured and used to rank and add the offspring within the existing population through a generational method. For each generation, a specified number of masks, G (in this case half of the population size), is replaced by the new offspring regardless of their cost function, at the expense of the lower ranked masks of the previous generation (See Figure 2.1).

2.3 Modeling of GA-enabled focusing through scattering

Modeling and simulation of the focusing algorithms allows for testing and optimizing the GA, as well as comparison with previously developed algorithms. The scattering process was modeled as a linear relation between the complex field at the input modes and the complex field at the output modes[49]:

$$E_m = \sum_{n}^{N} t_{mn} A_n e^{i\phi_n}, \tag{2.1}$$

where E_m is the complex field at output mode m. A_n is the amplitude contribution from input mode n, which is assumed to be uniform across the input plane and is defined as: $A_n = 1/\sqrt{N}$. ϕ_n is the phase at input mode n. The optical path through the scattering material is represented by an MxN transmission matrix (t) generated from a circular Gaussian distribution. The transmission matrix element t_{mn} relates the field at input mode n to the output mode m. The transmission matrix relates the complex field at N input modes to the complex field at M output modes.

The simulation uses the GA phase optimization algorithm to maximize the intensity of a specified output mode. The cost function measurement for the GA is defined as the intensity of the target output mode, *m*, with a given input mode phase distribution:

$$I_m = \frac{1}{N}\left|\sum_n^N t_{mn} e^{i\phi_n}\right|^2 . \tag{2.2}$$

To simulate experimental conditions the simulation included adding Gaussian noise to the cost function measurement. Varying levels of additive Gaussian noise were simulated to test the robustness of the GA in noisy environments. To further simulate experimental conditions a perturbation to the transmission matrix was included after each measurement to model either a sample whose structure or position changed with time. The perturbation simulations were implemented following the model described in Ref. [49].

2.4 Comparison of simulated algorithms

The overall possible enhancement which can be achieved by the GA is dependent on the number of input modes optimized. The enhancement, η, is defined as the ratio between the output mode intensity, I_m, and the initial average intensity, $\langle I_0 \rangle$. The enhancement dependence on input modes is the same as the CSA and TM (excluding reference beam) focusing methods[49], [53]: $\eta = \pi / 4(N-1)$, where N is the number of optimized input modes and the speckle decorrelation time, T_c, is much larger than the iteration time, T_i. The difference between the GA and CSA method is that the GA initially converges quickly, but approaches the maximum enhancement much more slowly. The PA under its ideal conditions ($N \gg T_c/T_i$), produces a theoretical enhancement that does not depend on the number of modes, but on the relationship

between T_c and T_i: $\eta = 0.5T_c/T_i$. These optimum enhancements are established for low noise environments, but the achievable maximum enhancement degrades with additional noise[49].

The algorithms are compared based on the number of measurements. A measurement being defined as the process of measuring the intensity of a specific output mode (I_m) with a phase mask, as in Equation 2.2. The CSA with 10 phase samples performs 10 measurements per input mode. Thus, when optimizing a phase mask with N input modes, there are 10·N measurements to optimize a full phase mask. In this section the CSA, TM, GA, and PA algorithm simulations were run through 10·N measurements for comparison. Each algorithm used N=256 input modes with a large speckle decorrelation time (T_c=50,000 measurements). Section 2.8 includes simulations comparing all algorithms in the regime where T_c is relatively small and the number of input modes for the GA and PA have been increased for best performance. The GA parameters selected for the simulation are indicated in Section 2.9. The effect of population size and number of input modes in GAs is explored in Section 2.7.

Figure 2.2 shows the enhancement of a focal spot with the various phase control algorithms for different levels of noise. Each algorithm was simulated 500 times, each time with a new transmission matrix, and then averaged for comparison. As expected, the CSA shows a quadratic improvement in enhancement. The PA initially enhances the intensity of the output mode more quickly than all others, but the rate of improvement rapidly decreases. In contrast, the simulation results indicate that with noise at 30% (Figure 2.2(a)) of the initial average intensity, $\langle I_0 \rangle$, the GA has an initially higher enhancement increase and can attain a higher overall enhancement through 10·N measurements than the CSA, PA, and TM optimization methods. After 4·N measurements the TM method has measured the transmission matrix and creates a focus, which is initially higher than all other iterative methods.

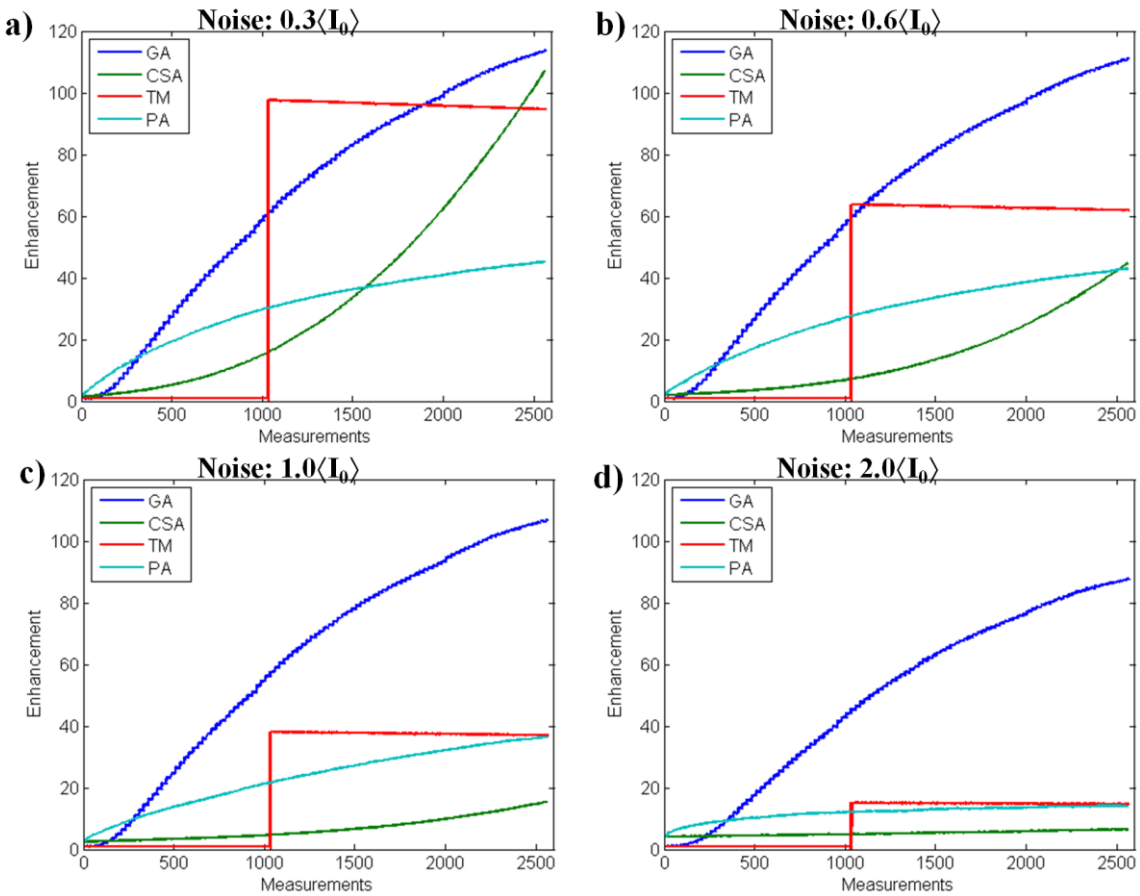

Figure 2.2. Simulations of the genetic algorithm (GA), continuous sequential algorithm (CSA), transmission matrix focusing (TM), and the partitioning algorithm (PA) comparing the enhancement of the focus to the number of measurements with varying noise levels. (a) Additive Gaussian noise at 30 percent of the initial average intensity, $\langle I_0 \rangle$. (b) 60 percent noise. (c) 100 percent noise. (d) 200 percent noise.

As the measurement noise level increases, the advantage of the GA becomes more dramatic. The CSA requires more measurements to raise the signal above the noise floor to start consistently making correct phase decisions. The inaccuracies in the measured transmission matrix increase with more noise, resulting in errors to the calculated phase mask. The PA, which modulates half of the input modes for optimization performs well in these conditions. Modulating half of the input modes increases the signal modulation strength and as such raises the modulated signal measurement above the noise level. The GA however, outperforms all

algorithms at high noise. The GA is less susceptible to noise, because it measures the merit of an entire mask and as a result, its cost function measurement quickly rises above the noise floor.

In Sections 2.7 and 2.8 the GA performance under relatively short T_c conditions is explored. In Section 2.7 the implications of the population size and number of input modes in these conditions suggests a tradeoff between population size and intensity enhancement consistency and a limitation in the enhancement imposed by the short T_c. Section 2.8 compares the CSA, TM, PA, and GA algorithms with the short T_c condition under increasingly noisy conditions, with an increased number of input modes for the PA and GA. As with the long T_c case, the GA performance is not severely affected by high noise levels, while the other algorithms performance deteriorates significantly.

2.5 Experiment

The algorithms were tested using a 425 micron thick chicken eggshell as the scattering material. A total intensity transmission measurement verifies the mean free path of the eggshell is less than ten times its thickness[11]. A HeNe laser and a phase-only spatial light modulator (Holoeye HEO 1080P) generated N=256 propagating input modes, that were focused with an objective lens (100X, NA = 0.75) onto the surface of the scattering sample. A second objective (20X, NA = 0.4) imaged a plane 1 mm behind the eggshell. The target was to create a focus on the opposing side of the eggshell. The cost function intensity measurements were provided by a 12-bit CCD camera (Point Grey Research Grasshopper). For comparison, each algorithm was run through 10·N measurements, which is equivalent to the number of phase mask measurements the CSA runs through in optimizing all input modes a single time. Each measurement was obtained at a rate of approximately 4.5 Hz. We varied the measurement noise by decreasing the shutter

speed of the camera. Each algorithm was run ten times for each noise level. The GA parameters selected for the experiment are shown in Section 2.9. The results are shown in Figure 2.3(b)-(f).

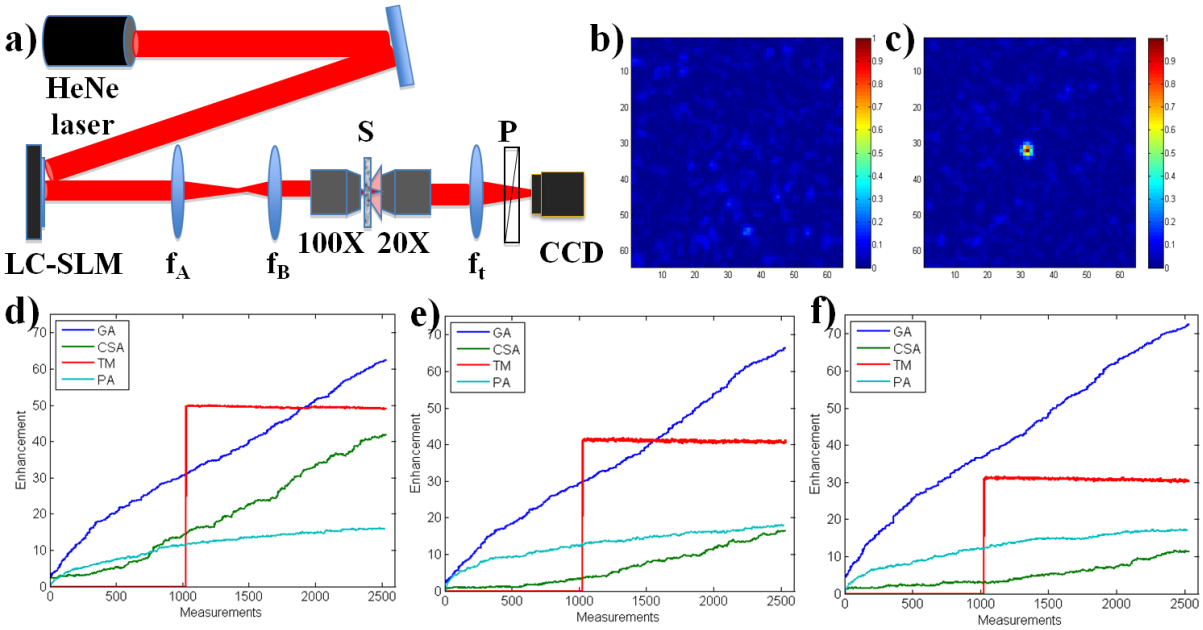

Figure 2.3. (a) The experimental setup. LC-SLM: liquid crystal – spatial light modulator. f_A, f_B, and f_t: lenses. 100X and 20X: objective lenses. S: scattering sample. P: linear polarizer. (b) The speckle field of light after passing through scattering material. (c) A focus spot created using the genetic algorithm. Signal to background ratio: 50. (d),(e), and (f) Experimental results of the genetic algorithm (GA), continuous sequential algorithm (CSA), the transmission matrix (TM), and the partition algorithm (PA) focusing methods. (d) With noise at 7 percent of initial average intensity, $\langle I_0 \rangle$, (e) 18 percent of $\langle I_0 \rangle$, and (f) 25 percent of $\langle I_0 \rangle$.

The low noise experiment (Figure 2.3(d)) shows the evolution of the enhancement of the spot intensity with each measurement. The standard deviation of the noise was measured to be at 7 percent of the initial average intensity, $\langle I_0 \rangle$. The experiment agreed well with simulation and shows that the GA achieves a higher enhancement after 10·N measurements than the CSA, TM, and PA. Similar to the simulations the TM achieved a higher enhancement after 4·N measurements than the CSA and GA after 4·N measurements.

The higher noise experiments (Figure 2.3(e) and (f)) show how the CSA and TM methods suffer with high noise. Noise in Figure 2.3(e) was measured to be 18 percent of the

average background intensity; while the noise in Figure 2.3(f) was measured to be 25 percent of the initial average intensity. With increased measurement noise the errors in the measured transmission matrix increased and lowered the enhancement of the focus spot. The CSA struggled to increase the enhancement with higher noise. The PA and GA perform just as well in any of the noise environments, with the PA more severely affected at the highest noise levels. However the GA initially increases faster and achieves a much higher enhancement.

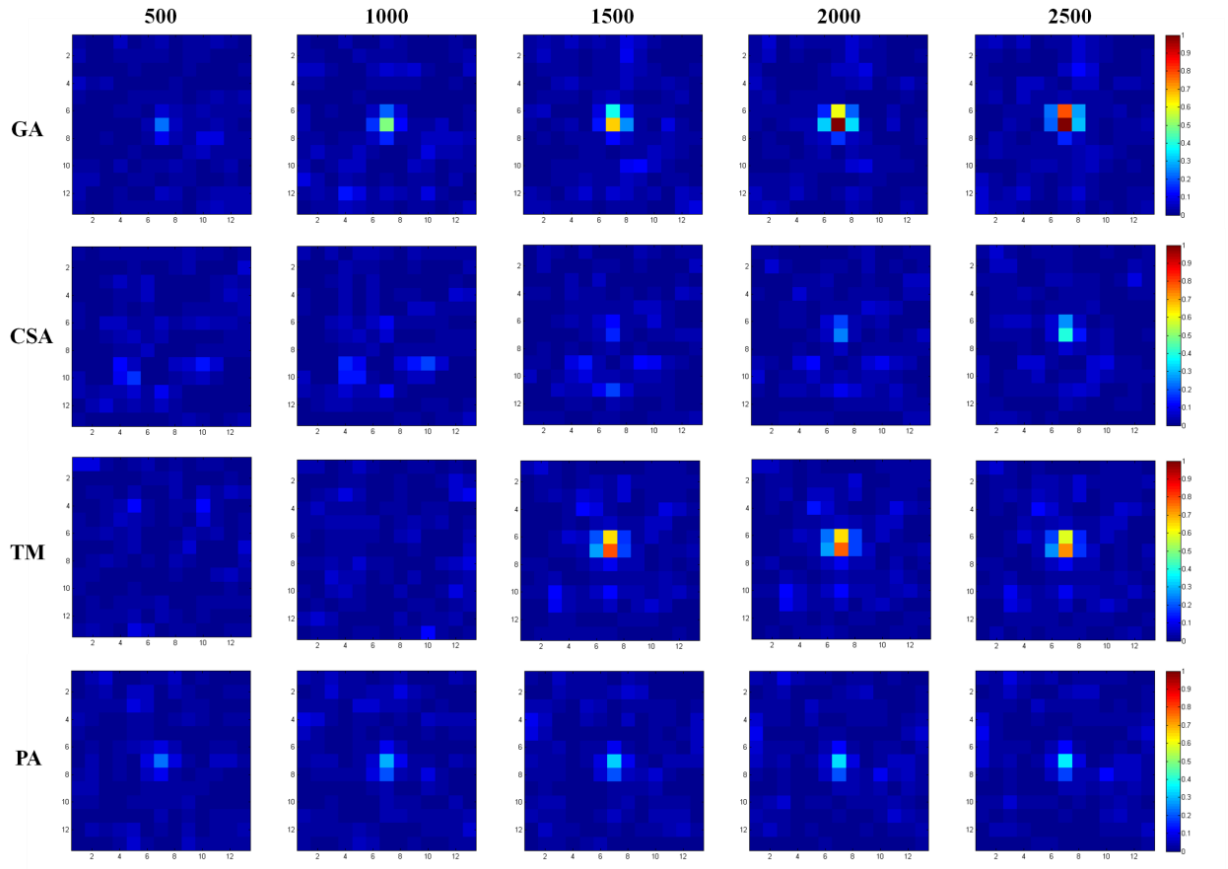

Figure 2.4. Comparison of the focal spots created after 500, 1000, 1500, 2000, and 2500 measurements under high noise conditions (corresponding to Figure 2.3(f)) with the GA, CSA, TM and PA methods. The intensities are normalized with respect to the maximum intensity attained with the GA algorithm after 2500 measurements.

Our experiments varied from the simulations in two areas. First, the experimental noise was signal dependent due to vibrations in the system. In other words, a displacement that reduces the signal to half its maximum, at a given enhancement, will also reduce the signal to half of the maximum for a higher enhancement. Hence, as the intensity of the output mode increases with the wavefront optimization, the measured noise in the system also increases due to vibrations creating shifts in the egg shell position relative to the optimized wavefront[55]. In our case the vibrations were mostly caused by the LC-SLM fan. While these could be reduced, we found it instructive to analyze the behavior under this perturbation. Unlike the other algorithms, the CSA was highly affected by this noise because it measures small variations on a high peak intensity. The TM measured the field before setting the optimized wavefront, typically with low intensities, so it was not significantly affected by this vibration noise. The PA intensity was never high enough to be negatively affected. The GA showed little, if any, degradation in performance from the increased noise, which further demonstrates its advantage under high noise conditions. In fact, the overall enhancement from the GA increased with increasing noise, although this was likely a result of the vibrations lowering the average peak intensity with a longer integration time in the lower noise experiments.

A second deviation from the simulation was a sample (Chicken eggshell) with a varying speckle decorrelation time most likely caused by thermal drift. The speckle decorrelation time is a measure of the temporal stability of the scattering sample[49]. We have measured speckle decorrelation times as long as 5000 seconds (22,500 measurements) and as short as 140 seconds (630 measurements) with the Chicken eggshell sample, with an average speckle decorrelation time of 2200 seconds (10,000 measurements). This high variability in the speckle decorrelation time increased the unpredictability of the overall enhancement achieved. (See Figure 2.5)

Therefore, in the experiments the overall enhancement reached by each algorithm was lower than in the respective simulations by at least 50 percent due to these two non-ideal factors. Nevertheless, the experiments demonstrate the same trend expected from the simulations, the same relative merit of each algorithm, and further illustrate the advantage of the genetic algorithm in non-ideal conditions.

2.6 Conclusion

The GA optimizes modes in parallel which results in a fast initial increase in the intensity enhancement. Under optimal low noise scenarios the CSA and TM optimization algorithms reach the global solution; a result of using a linear algorithm to solve this linear problem. The GA, however, would have a slow convergence to a solution which may not be the global maximum. Increasing the population size and allowing far more iterations would increase the probability of achieving the global optimum; however this would increase the total optimization time. Importantly, as the measurement noise increases the linear optimizations fall short of the global solution. It is in this scenario that the GA outperforms the linear optimization methods. The GA does not rely on detecting small changes in the interference signal as the CSA, and TM methods do, but instead measures the response of full phase masks created through breeding and mutation operations. This process reduces the negative effects of measurement error as seen in the linear solutions, like the CSA and TM methods.

The simulations and experimental results show that the genetic algorithm phase mask optimization algorithm works well in high noise environments. Under our experimental conditions with the eggshell, the GA showed an initial faster enhancement of the focus intensity and achieved a higher overall enhancement than the CSA, PA, and TM methods. The GA

achieved similar results with noisy environments that severely inhibited the ability of the CSA to work and decreased enhancement using the TM method. The high noise robustness of the GA could be useful as the need for higher speed algorithms increases. Higher speed algorithms would allow for focusing through more temporally dynamic samples such as tissue.

2.7 Appendix A: Dynamic sample GA performance with input mode number and population size

To explore the effects of the various GA parameters with dynamic samples, we analyze the performance with a short speckle decorrelation time equal to 2560 measurements, or the same number of measurements required to optimize the CSA mask once. To better understand the GA performance dependence on input modes in this environment, optimizations with 256, 1024, and 4096 input modes were simulated. The GA parameters are listed in Section 2.9. 500 simulations were performed and averaged.

The results are shown in Figure 2.5(a), with an inset showing the standard deviation of the enhancement data. As expected, the simulations indicate that more input modes results in a higher enhancement. They also indicate that the enhancement diminishes at higher N as a result of the short T_c, which changes the transmission matrix such that the seeding and subsequent breeding of the initial mask population degrades in quality as measured by the enhancement factor. Furthermore, by providing more degrees of freedom, using a higher number of input modes, leads to longer improvements before breaking down. The initial rate of increase is about the same for all input mode values for the first 500 measurements. Although not implemented in this report, the GA could be modified to avoid the enhancement degradation via periodic updates of the population measurements.

Further simulations were run to explore the effect of population size on the total enhancement and peak enhancement time (Figure 2.5(b)) with the GA parameters set as listed in Section 2.9. They reveal that a smaller population will optimize more quickly initially, but will saturate and break down sooner than larger population sets as a result of having less diversity in the population. The higher population also allows the algorithm to achieve a more consistent enhancement (Figure 2.5(b) inset). The standard deviation of the enhancement for the 500 runs is smaller for the higher population set, thus indicating a tradeoff between enhancement speed and intensity enhancement consistency.

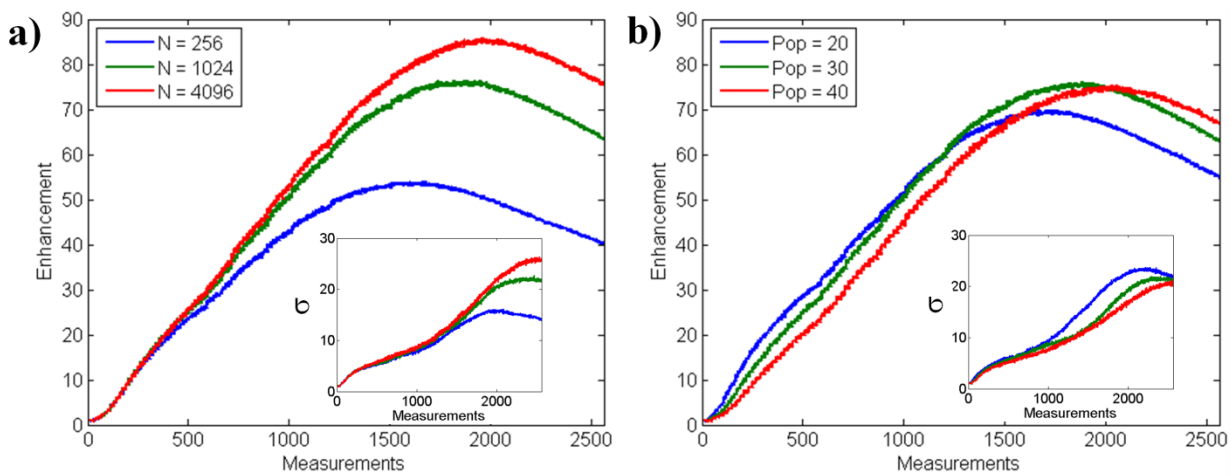

Figure 2.5. (a) Comparison of the GA simulated with T_c = 2560 measurements for 256, 1024, and 4096 input modes. The inset shows the standard deviation of the enhancement for the 500 simulated runs. (b) Comparison of the GA simulated with population sizes of 20, 30 and 40. The inset shows the standard deviation of the enhancement for the 500 simulated runs.

2.8 Appendix B: Comparison of algorithms with low sample speckle decorrelation time

A full comparison of all algorithms was simulated under a relatively low speckle decorrelation time (T_c = 2560 measurements) condition. For this comparison the GA used N = 1024 input modes. The PA used N = 2048 input modes, which placed it in the regime of

$N >> T_c/T_i$ where it should perform optimally[49]. The CSA and TM methods still optimized N = 256 modes. The GA parameters are shown in Section 2.9.

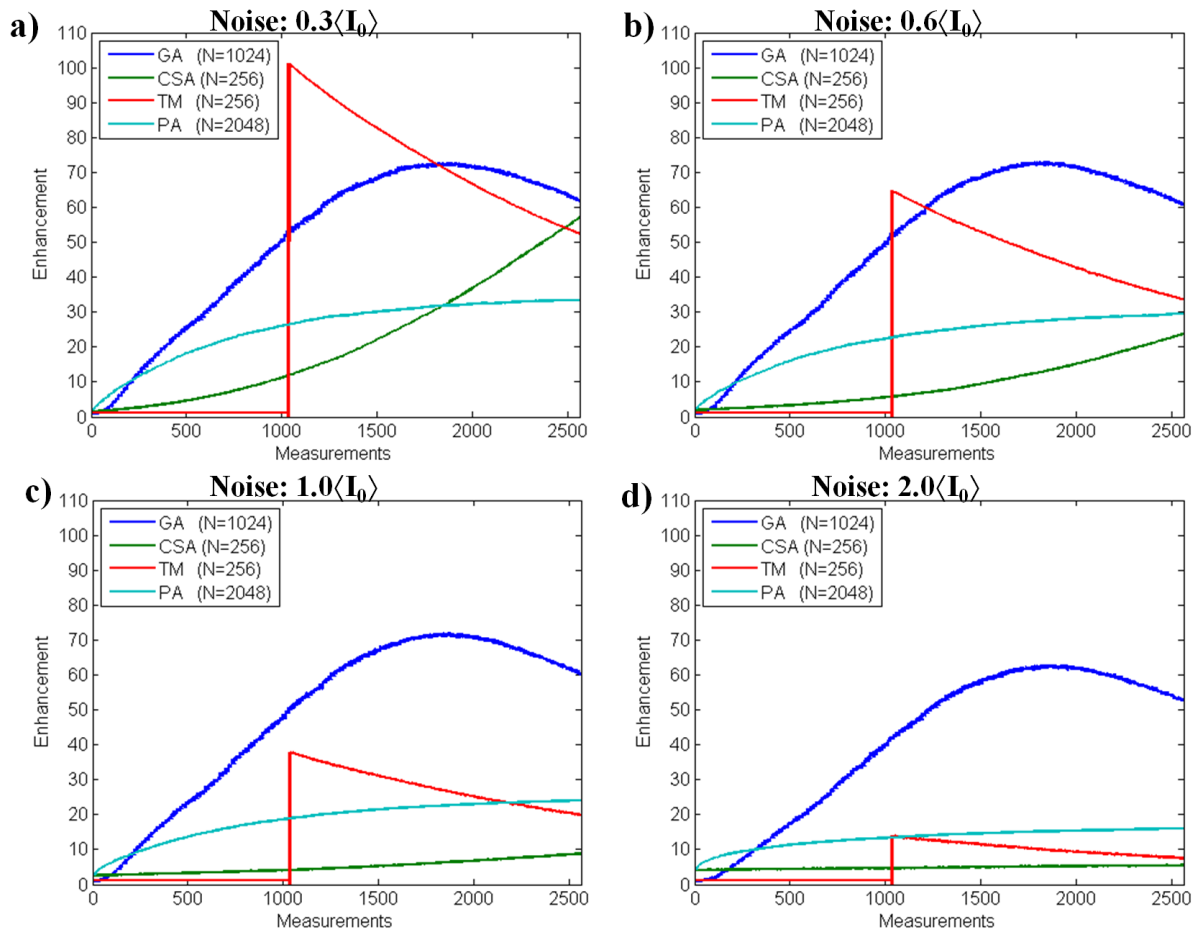

Figure 2.6. Simulations of the genetic algorithm (GA), continuous sequential algorithm (CSA), transmission matrix focusing (TM), and the partitioning algorithm (PA) comparing the enhancement of the focus to the number of measurements with varying noise levels with low speckle decorrelation time (T_c = 2560 measurements). (a) Additive Gaussian noise at 30 percent of the initial average intensity, $\langle I_0 \rangle$. (b) 60 percent noise. (c) 100 percent noise. (d) 200 percent noise.

As with the results shown in the long speckle decorrelation time simulations, the increasing noise levels severely degrade the CSA, PA, and TM algorithm performance. Under the lowest noise case, $0.3\langle I_0 \rangle$, the TM method, with its relatively low number of measurements can achieve a high enhancement after 1024 measurements, although this high enhancement

quickly decays as the transmission matrix changes. In this implementation the PA fails to achieve the theoretical enhancement of $\eta = 0.5T_c/T_i$, despite $N >> T_c/T_i$. The CSA quadratically improves with the number of measurements, but at a slower rate than in the long T_c simulations. The GA optimizes more quickly through the first measurements than the other algorithms, before reaching a break down point just before 2000 measurements. As with the long T_c case the GA continues to achieve a high enhancement despite increasing noise conditions. (See Figure 2.6.)

2.9 Appendix C: Simulation and experimental GA parameters

The reported simulations and experiments used different GA parameters. These parameters are reported in Table 2.1.

Table 2.1. GA parameters used in various simulations and experiments reported in this paper. The section number indicated identifies the corresponding simulation or experiment.

Section	Input modes (N)	Population size (Pop)	New offspring per generation (G)	Mutation rate begin (R_0)	Mutation rate end (R_{end})	Mutation rate decay factor (λ)
2.4	256	50	0.5·Population	0.1	0.0025	200
2.5	256	30	0.5·Population	0.1	0.013	600
2.7 (2.5(a))	variable	30	0.5·Population	0.1	0.012	650
2.7 (2.5(b))	1024	variable	0.5·Population	0.1	0.012	650
2.8	1024	30	0.5·Population	0.1	0.012	650

CHAPTER 3

COLOR IMAGE PROJECTION THROUGH A STRONGLY SCATTERING WALL

3.1 Introduction

The genetic algorithm (GA) was introduced in Chapter 2 for wavefront optimization in focusing light through turbid media. The GA successfully optimized the wavefront input modes in parallel, which allowed an initially higher rate of enhancement than sequential algorithms. Furthermore, the GA demonstrated superior performance in low SNR environments. The task of the simulations and experiments described was to create a single focus spot through the scattering material, as was done in other wavefront optimization algorithmic demonstrations[47], [51], [53]. These have shown how focusing light through turbid media is achieved by optimizing the incident wavefront to overcome the effects of multiple scattering and constructively interfere many input modes at a single speckle output mode after scattering. This has been demonstrated with optical phase conjugation[55], [83] or with a feedback system which uses a spatial light modulator (SLM) for wavefront control to maximize the focus spot intensity[1], [47], [50], [53], [68]. Most of these studies and techniques demonstrated the creation of a single focal spot inside of or through the turbid material[1], [47], [49], [50], [52], [53], [55], [66], [68], [83], with little

or no emphasis placed on focusing to multiple spots[49], [53]. Further research has explored the use of turbid material wavefront control for image transmission, but unfortunately none has achieved direct image creation through highly scattering materials[59], [60], [89]. For example, [59] and [89] require digital image reconstruction and [60] only works in thin (weakly) scattering media while operating on a limited field of view. Alternatively, scanning techniques require point-by-point reconstruction using, for instance, fluorescent particles[11] or second harmonic generation[79]. Image formation has also been demonstrated using OPC, however, the technique was limited to reforming an image of a real object, not creating arbitrary images[55].

In contrast, this chapter presents image creation and projection through highly scattering turbid media using multiple wavelengths without need for reconstruction. The technique requires a global optimization for which we implement a wavefront optimization genetic algorithm (GA)[52]. We show that the GA optimizes multiple spots with high uniformity and intensity. We experimentally demonstrate multiple focal spot and multiple wavelength focusing. We then demonstrate the creation of multi- wavelength images using this technique. The four distinct aspects of this image projection technique relative to prior proposals are: (1) the wide-field image appears without any need of further reconstruction after the adaptive optimization (except for demosaicing when needed), (2) it is amenable to thick, highly scattering media, (3) it can encode color images using RGB channels, and (4) it is capable of creating synthetic light objects.

3.2 Image projection through turbid media

The task at hand can be understood in two different ways, namely the creation of images using a turbid material in conjunction with a SLM or the creation of images through a given turbid material. The method decomposes the pattern into multiple focal spots and focuses

coherent, scattered light at those preselected locations creating an image. From a different perspective the process can be understood as the shaping of the speckle pattern for image formation.

The maximum enhancement or signal to background ratio (SBR) possible in this method is determined by the number of input modes used for wavefront control. The SBR for a single focus spot, $\eta(1)$, is defined as the ratio between the output mode intensity, I_m, and the initial average intensity, $\langle I_0 \rangle$. The SBR dependence on input modes is[47]: $\eta(1) = \pi / 4(N-1)$, where N is the number of optimized input modes. However, by focusing to multiple focus points, M, the maximum SBR is scaled by the number of focus points created: $\eta(M) = \eta(1)/M$, as the enhancement distributes evenly between targets[49], [68]. The total number of input modes which can be used is limited by the degrees of freedom of the SLM and the optics. Other factors, such as, sample drift and the diffraction efficiency of the SLM, further degrade the maximum achievable enhancement[1].

To efficiently optimize the wavefront to create the desired image through the turbid material we employ a genetic algorithm (GA)[52]. After verification via simulation we show that the genetic algorithm optimizes multiple points with a smaller standard deviation than the continuous sequential algorithm (CSA)[49] using either an intensity or amplitude metric.

We use a scattering model simulation for comparison of the GA and CSA[49], [52]. For multiple spot focusing the GA cost function and the CSA feedback need to take into account multiple targets. We modify the GA cost function to maximize the intensity of the focal spots, while penalizing for large differences in intensity value. Specifically, we modify the cost

function, C, to be the summation of all the focus spot intensities, I, minus the number of focus spots, M, multiplied by the standard deviation of the intensities of the focus spots, $\sigma(I)$:

$$C = \sum_{m=1}^{M} I_m - M \bullet \sigma(I), \tag{3.1}$$

where

$$I_m = \frac{1}{N} \left| \sum_{n}^{N} t_{mn} e^{i\phi_n} \right|^2, \tag{3.2}$$

where N is the number of input modes, t_{mn} is the transmission matrix through the turbid sample to target m from input mode n, and ϕ_n is the phase at input mode n. For the CSA feedback we use both the intensity (CSA-I) and amplitude metrics (CSA-A) presented by Vellekoop, et al[49], for multiple target focusing.

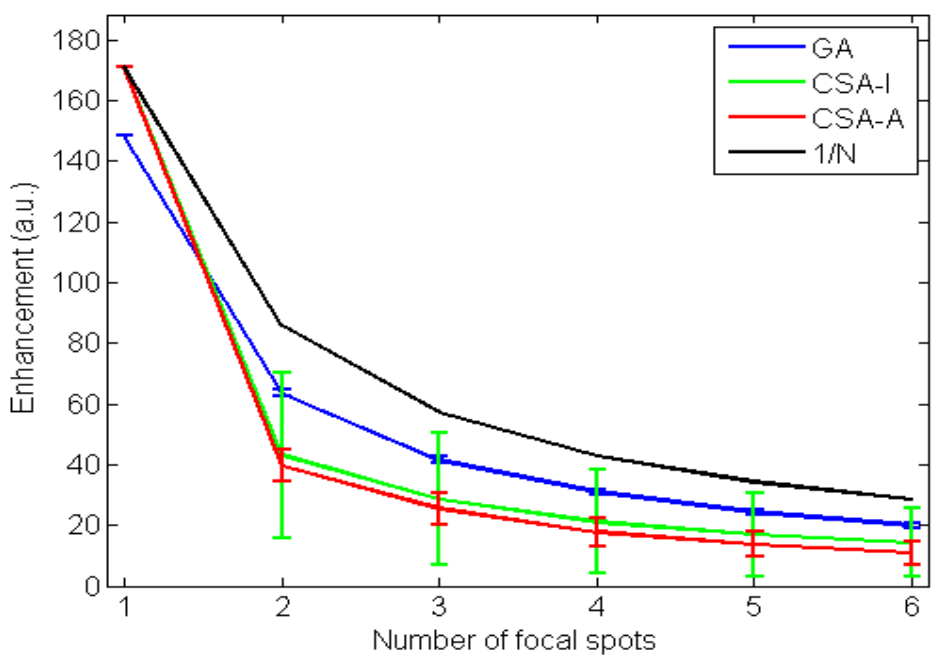

Figure 3.1. Simulation results comparing the mean enhancement and standard deviation of enhancement for the CSA-I, CSA-M, and GA methods to the ideal case of 1/N times CSA-I max.

We compare the algorithms based on the number of measurements. A measurement being defined as the process of measuring the GA cost function or the CSA metric for each phase mask. The CSA with 10 phase samples performs 10 measurements per input mode. Thus, when optimizing a phase mask with N input modes, there are 10·N measurements to optimize a full phase mask. For this simulation, we compare the GA and CSA algorithm simulations through 2·10·N measurements. Each algorithm has N=256 input modes with an infinitely long speckle decorrelation time. A Gaussian noise value of $0.3\cdot\langle I_0\rangle$ added to each measurement simulates experimental conditions. For this simulation the GA uses a population size of 50, with a mutation rate of $R = (R_0 - R_{end})\cdot exp(-d/\lambda) + R_{end}$, where R_0 is 0.1, R_{end} is 0.0025, λ is 1000, and d is the measurement number. Figure 3.1 shows the mean value of 100 optimizations for the CSA-I, CSA-A, and GA methods compared to 1/N times the CSA-I maximum for single point focusing. The error bar in the figure indicates the mean standard deviation of the enhancement for the various focal spots for the 100 optimizations. The simulations indicate that the GA leads to higher enhancements with lower deviation in the focal spot intensities than the CSA-A, which in turn improves over the CSA-I method with less spot intensity variability[49].

3.3 Experimental demonstration of multiple spot and multiple wavelength focusing

The GA is tested using a highly scattering 425 micron thick chicken eggshell. A total intensity transmission measurement verifies the mean free path of the eggshell is less than ten times its thickness[11]. Qualitatively this is confirmed through the observation that no detectable ballistic photons transmit through the eggshell. The illumination sources consist of HeNe (633 nm), frequency doubled Nd:YAG (532 nm), and Argon (455 nm or 514 nm) lasers collimated and combined on the same path. A phase-only SLM (Holoeye HEO 1080P) generates N=1024

propagating input modes, which are focused with an objective lens (40X, NA = 0.65) onto the surface of the scattering sample (Figure 3.2(a)). A second objective (20X, NA = 0.4) images a plane 1 mm behind the eggshell. The target is to create multiple foci on the opposing side of the eggshell, with either one or two colors. Single color focusing uses 633 nm illumination, while two color focusing uses 633 nm and 514 nm. The intensity measurements are provided by a 12-bit monochrome CCD (Point Grey Research Grasshopper) or a 12-bit RGB CCD camera (Point Grey Research Flea2). This camera has a RGB Bayer filter, thus providing color separation. The red, green, or blue pixels are used to create foci of red, green, or blue color, respectively. The algorithm runs until the GA cost function stops improving. Each measurement is obtained at a rate of ~4.5 Hz.

Initial experiments reveal that under the experimental conditions the ideal GA population size depends on the number of desired focal spots, with larger populations optimizing more focal spots more efficiently. Therefore, in this experiment the GA population size is varied depending on the number of desired focal spots. Furthermore, unlike the simulations the number of measurements required to maximize the focal spot intensities increases with the number of foci, thus, each iteration is run until the GA cost function is maximized. Each data point represented in Figure 3.2(b) is the average of ten experimental optimizations.

The experiment reveals that the GA intensity enhancement scales with the number of foci as shown in simulation and that multiple colors may be focused with enhancement values similar to a single color. This result can be explained by considering a second wavelength to have a unique transmission matrix through the sample, just as any individual focus spot has a unique transmission matrix from the input modes.

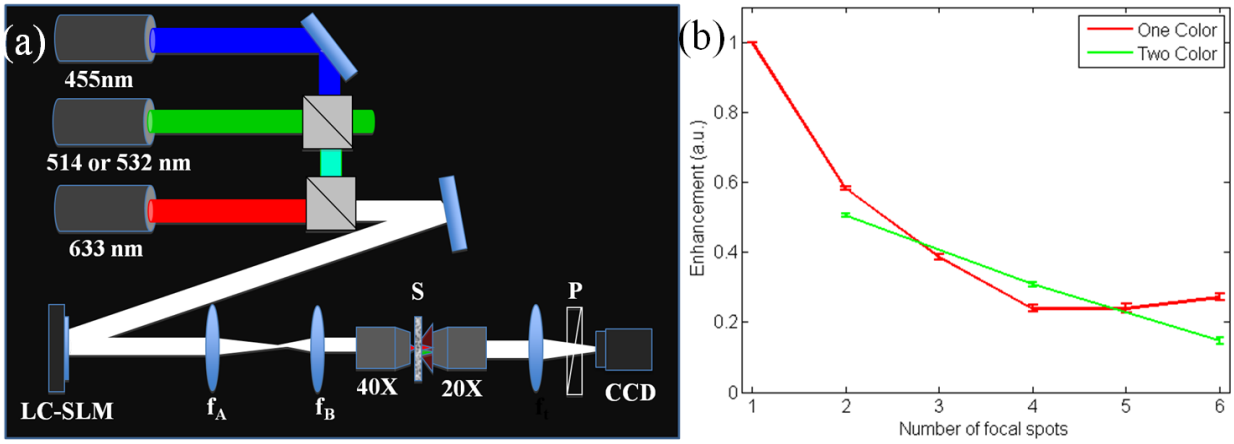

Figure 3.2. (a) The experimental setup. (b) Experimental results of focusing multiple spots with one and two colors with the GA. Each data point is experimentally optimized ten times.

Interestingly, the experimental data also reveals the variability of the GA with initial parameter selection, which resulted in a rather significant enhancement increase with the number of focal spots (from 4 to 6). An additional source of variability is the sample drift during the long experimental runs. The results of Figure 3.2(b) are presented to illustrate the sensitivity of the optimization to initial conditions and experimental perturbations.

3.4 Image formation

3.4.1 Single color image formation

To test image creation using wavefront control and turbid media we create an image generating the CU logo by superposition of a number of focal points. Using 4096 input modes and a single color (633 nm) the GA optimizes the image, composed of 49 focal points, as shown in Figure 3.3(a). After running through 55,000 measurements the image shown in Figure 3.3(b) is created. This image achieves an average SBR of 12.8 with a standard deviation in the SBR of the target points of 2.0. During the optimization 2x2 pixel binning with the monochrome CCD is used to match the size of a binned pixel to the size of a speckle grain. Figure 3.3(c) shows the

image captured without binning at a higher resolution. Interestingly, the image has high intensity throughout the targeted region, unlike typical reconstructions in computer generated holography (CGH) which suffer from speckle effects[90].

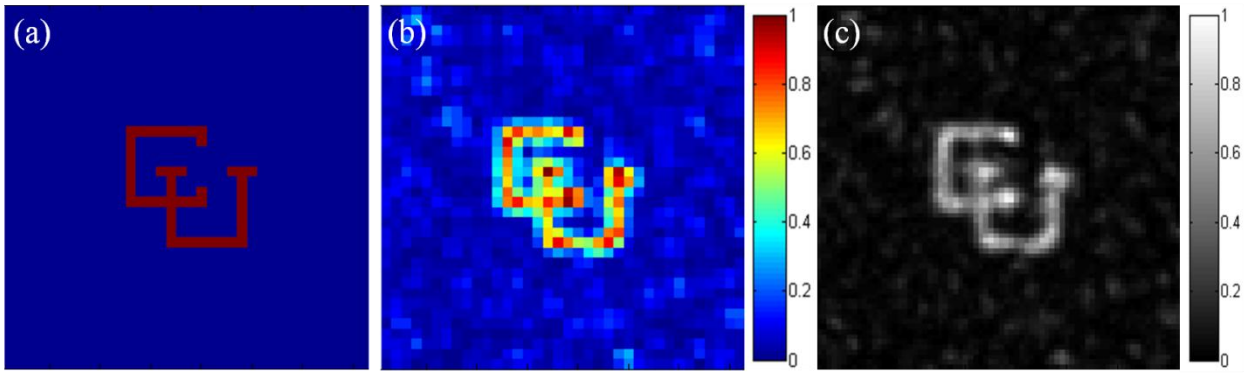

Figure 3.3. Single color image creation. (a) The target intensity distribution. (b) Experimentally generated intensity distribution through an eggshell using binned CCD pixels. (c) High resolution image intensity distribution.

3.4.2 Two color image formation

The ability to create images with two colors is tested through the creation of a number of focal points placed together to create a person riding a bike, with the rider composed of green light and the bike wheels composed of red light. Figure 3.4(a) shows the intensity distribution designed for a Bayer RGB filter. Using 3840 input modes and two colors (633 nm and 514 nm) the GA runs to optimize the image, which is composed of 49 separate focal points: 24 red and 25 green. After running through 35,000 measurements the image shown in Figure 3.4(b) is created with the RGB filter. This image achieves average SBR of 10.2 for the red and 9.6 for the green, with standard deviations of 1.1 and 0.9 respectively. The demosaiced color image, created using the MATLAB function “demosaic”, is shown in Figure 3.4(c) and clearly displays the two color target image. The SBR achieved for the two colors is similar to the SBR obtained with a single

color for the same number of focal spots. These results verify the experiment demonstrated in Figure 3.2(b) on a larger scale.

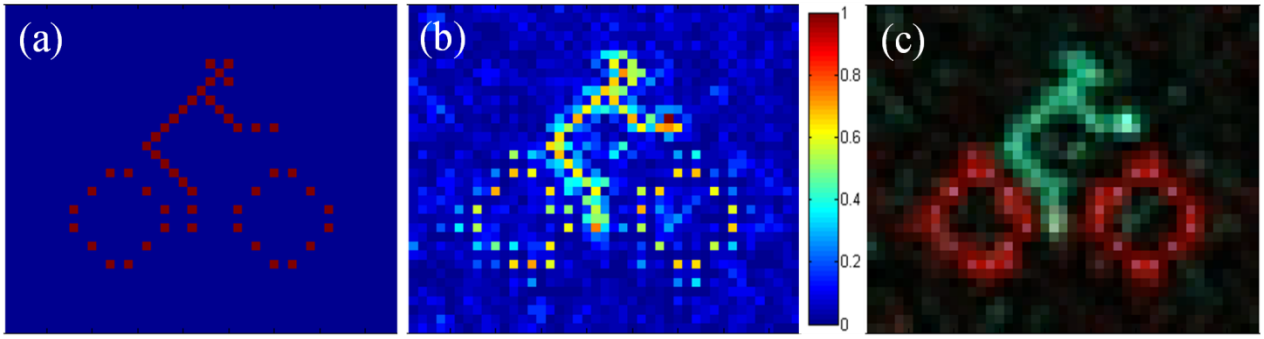

Figure 3.4. Two color image creation. (a) The desired intensity distribution designed for an RGB Bayer filter CCD. (b) Experimentally obtained intensity distribution through an eggshell with RGB CCD. (c) Two color image obtained after demosaicing the image in (b) with same resolution.

3.4.3 RGB image formation

Finally, we test three color image formation designed for RGB demosaicing to create full-color images. We place a number of focal points in the desired image to create a rainbow. By designing a target intensity distribution for the Bayer RGB filter (Figure 3.5(a)) a full color image of a rainbow is generated through demosaicing (Figure 3.5(b)). Using 2048 input modes and three colors (633 nm, 532 nm, and 455 nm) the GA runs to optimize the image, which is composed of 49 separate focal points: 16 red, 26 green, and 8 blue. After running through 20,000 measurements the image shown in Figure 3.5(c) is created. This image achieves an average SBR of 5.5, 10.8, and 7.0 for the red, green, and blue, respectively. The standard deviations are 0.6, 2.4 and 0.8 for the red, green, and blue, respectively, this measure scales the various SBR values by their target intensity (Figure 3.5(a)). The large disparity in the SBR of the different wavelengths is a side effect of the 532 nm laser having poor power stability. This also affects the

time the algorithm can run. Despite this technical issue, the demosaiced image (Figure 3.5(d)) clearly shows a rainbow following the desired image pattern (Figure 3.5(b)).

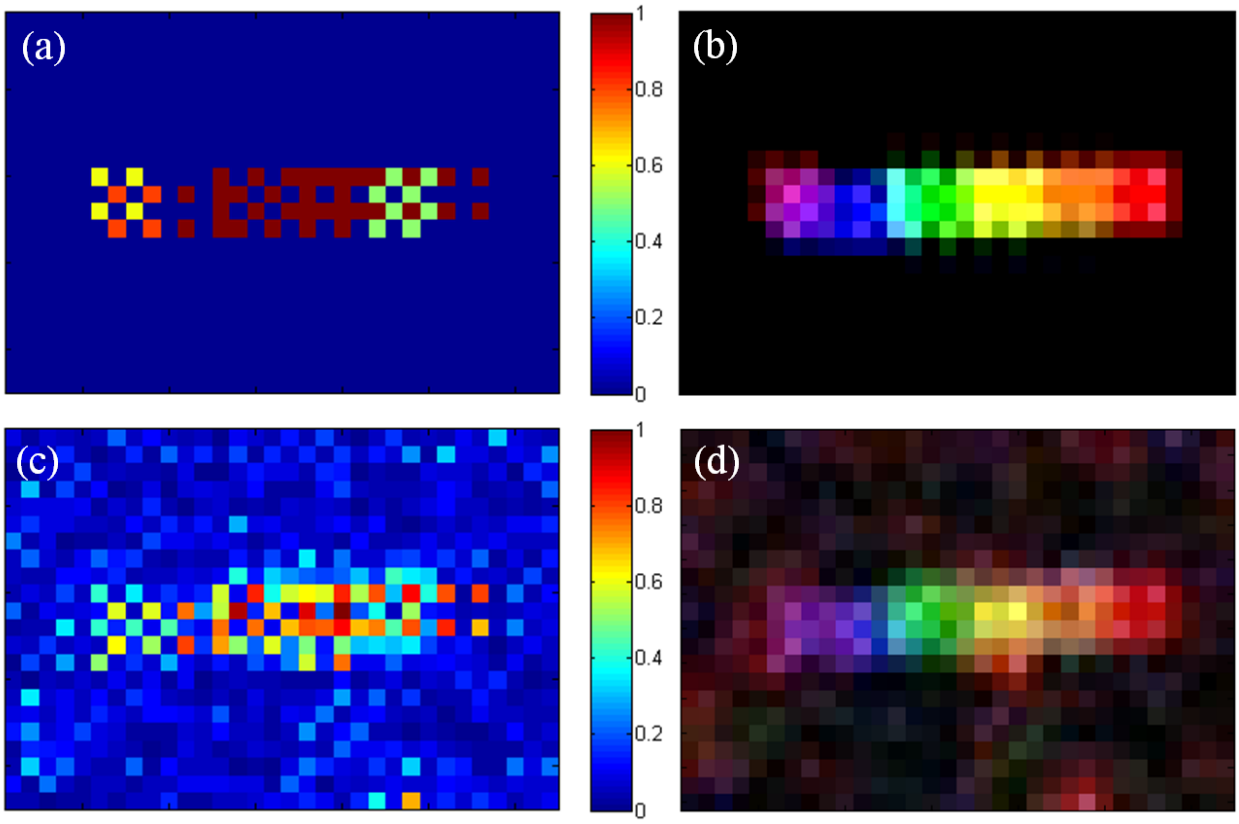

Figure 3.5. Three color pattern projection for full color image creation. (a) The target intensity distribution designed for an RGB Bayer filter CCD. (b) Rainbow created by demosaicing the target intensity distribution. (c) Experimentally obtained intensity distribution captured with RBG CCD through an eggshell. (d) Rainbow obtained after demosaicing the image in (c).

3.5 Discussion and conclusions

Similarly to computer generated volume holography and CGH the color image projection technique uses diffraction, but it is notably different in that it also takes advantage of multiple scattering for pattern formation. Therefore, it is the scattering which ultimately determines the image resolution, not the NA of the optics, as in CGH. Thus, the speckle size will ultimately yield the resolution[50]. The bandwidth of the light which can be focused through turbid media is also limited by the scattering properties of the material[91]. The more highly scattering the

material is, the narrower the bandwidth required. This is particularly useful when focusing multiple wavelengths, as the material uncouples the transmission matrix of different wavelengths. The method spatially multiplexes the input modes to create multiple focused wavelengths simultaneously. Limitations in the experimental system are a result of the spatial modulator device, which has a low fill factor, decreasing the maximum possible SBR. Furthermore, this device has a slow modulation speed, thus causing sample drift to limit the algorithm run time[49], [52]. Both of these issues can be addressed, for example, with the use of a deformable mirror device for wavefront control[66], [67] with a high speed camera.

In conclusion, we have demonstrated the use of wavefront control with highly scattering media for image creation using multiple focus spots and wavelengths. We have shown that a GA, with a cost function designed for the task, can be used for efficient creation of multiple, high intensity focal spots with small variations in intensity. This algorithm was used experimentally for the creation of multiple wavelength images. These images show uniform spot intensity with low standard deviations. Interestingly, the adaptive optimization reduces the negative speckle effects common in image creation with CGH.

Image formation with highly scattering materials could find applications in various fields. For example, focused patterns could be used to activate deep neurons with light using photochemical uncaging probes and allow near arbitrary excitation patterns, thus enabling three dimensional neuronal connections to be mapped by the simultaneous excitation of multiple neurons[86]. Furthermore, multiple wavelength focusing could be used for the excitation of different fluorophores in deep tissue fluorescence imaging. Pattern generation through turbid media could also be used for materials processing or energy delivery for various medical treatments.

CHAPTER 4

HIGH-SPEED WAVEFRONT MODULATION FOR FOCUSING LIGHT THROUGH DYNAMIC TURBID MEDIA

4.1 Introduction

An application of particular interest in controlling light through scattering layers is sensing and imaging into biological materials. Scattering limits the imaging depth into biological tissue, however recent work has demonstrated how scattering may be compensated via wavefront control[47]. The wavefront compensation is complicated in biological tissue by blood and other cells which move in the tissue and change light scattering with time. Thus, a fast wavefront optimization is important for focusing through the dynamic turbid layer within its speckle decorrelation time. The speckle decorrelation time of a turbid sample is the time over which the speckle pattern remains relatively stable and consequently the time over which an optimized phase mask will maintain a focus[64]. The previous chapters have demonstrated light control through scattering layers with a genetic algorithm wavefront optimization. In Chapter 2 this algorithm allowed for faster optimization through parallel input mode optimization and better performance in low SNR environments. While this algorithmic work reduced the time required to form a focus through scattering layers relative to sequential optimization techniques, the

demonstrations were fundamentally limited by switching rate restrictions imposed by the wavefront modulation device. Therefore, in this chapter a novel technique is introduced for high-speed wavefront modulation.

Most current focusing through turbid media methods use liquid crystal spatial light modulators (LC-SLM) for phase-only wavefront modulation[47], [49]–[53], which is more efficient for creating a focus than amplitude only modulation[93]. The LC-SLMs switching speed is limited by the rate at which the liquid crystals can align in the device which ranges from 10s to 100s of Hz. However, many living biological materials have speckle decorrelation times on the millisecond timescale[56], [64], [94]. As an example, consider a sample with a 100 ms speckle decorrelation time and an iterative optimization requires about a thousand measurements. Together these require at least a 10 kHz modulation rate to focus within the time restriction; far beyond the capabilities of liquid crystal devices. Thus, new high-speed techniques for optimizing phase masks are required to implement focusing through biological samples.

A first step in this direction has been implemented recently in a system that uses a scanned laser beam for wavefront determination and an LC-SLM for the final phase modulation[65]. The system achieved wavefront determination in 400ms. This chapter describes a new high-speed phase mask optimization technique, which utilizes off-axis binary-amplitude computer-generated holography implemented on a digital micromirror device (DMD)[95] and demonstrates wavefront determination about one order of magnitude faster than the prior state of the art[65], [66]. Furthermore, the transmission matrix approach provides a general and thorough characterization of the scattering medium that not only allows for focusing on a given point in space but also enables the determination of wavefronts for other optical processing applications[53], [59], [96]. The main speed limitation of the initial system described is the

increased computation and data transfer time created by sending the data to a computer and then back to the DMD. This limitation is overcome through optimization algorithm implementation on the FPGA included with the DLP Discovery Kit, DLP4100, to reduce the total time to focus from 300 ms to 37 ms.

4.2 Binary amplitude holography

We introduce the computer-generated holographic technique to simultaneously implement phase-only control of the wavefront using the high switching speed of DMDs. Phase-only wavefront modulation has in principle a theoretical enhancement five times higher than binary amplitude modulation for the same number of input modes[47], [93]. Considering that biological samples have a limited timeframe for focusing in the 10s of milliseconds and that commercially available DMDs have a maximum full-image frame rate of 22.7 kHz, the possible number of optimized modes available under these conditions is limited. For this reason we combine the 1024x768 array of binary pixels into far fewer modes for phase-only modulation through off-axis binary amplitude holography. As a result, we are able to simultaneously take advantage of the high efficiency of phase modes and high frame rate of DMDs.

Binary amplitude off-axis holography is a well known method for generation of uniform-amplitude phase-modulated images[97]. We generate an amplitude hologram, $t(x,y)$ using the Lee method[97]. An off-axis reference wave encodes the desired phase distribution, $\varphi(x,y)$:

$$t(x,y) = 0.5\left[1+\cos(2\pi\left(x-y\right)\alpha-\varphi(x,y)\right], \tag{4.1}$$

where the carrier frequency is α, while x and y are the spatial coordinates of the hologram. In this implementation the hologram is off-axis diagonally with the carrier frequency selected to minimize crosstalk among orders by providing a large enough separation of the -1st order from

the 0th order beam. The binary amplitude hologram, *h(x,y)*, is generated by thresholding the amplitude hologram, *t(x,y)*. In order to maximize the diffraction efficiency the width of the fringes is chosen to be half of the fringe periodicity. This is accomplished by thresholding according to[97]:

$$h(x,y) = \begin{Bmatrix} 1; & t(x,y) > 0.5 \\ 0; & otherwise \end{Bmatrix}. \tag{4.2}$$

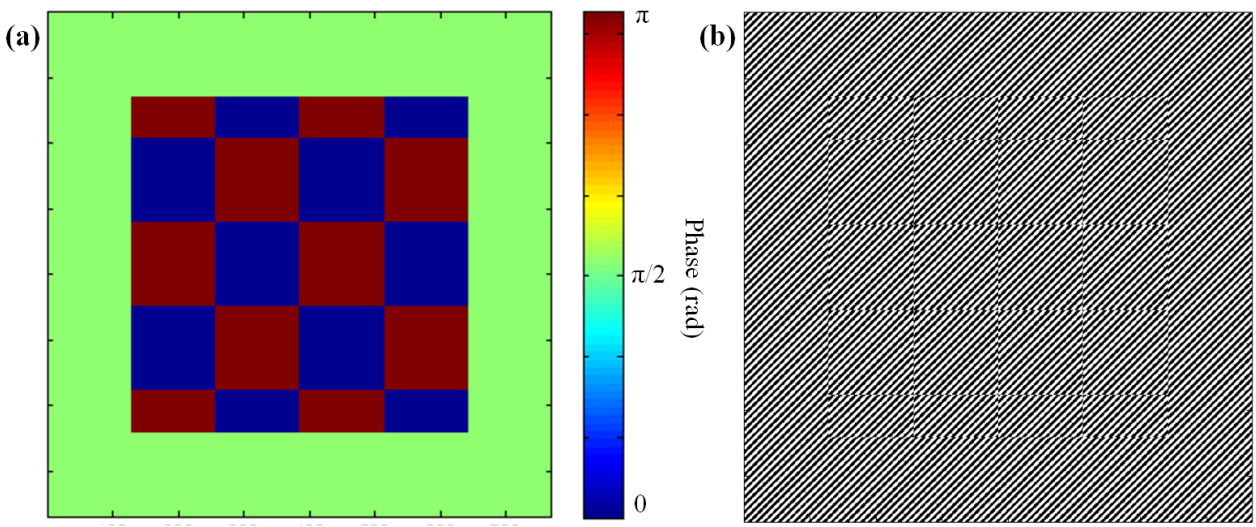

Figure 4.1. (a) An example of a phase distribution, *φ(x,y)*, for a single Hadamard basis element surrounded by a phase reference for transmission matrix measurement. (b) The binary amplitude Lee hologram, *h(x,y)*, which encodes the phase distribution shown in (a).

This technique can be extended to phase and amplitude modulation by selecting thresholds that give the appropriate relative amplitude of *t(x,y)*[97]. However, the available amplitude levels are limited by the number of pixels per period which must be relatively small to allow sufficient separation between diffraction orders. The desired wavefront is produced in the -1st diffraction order, thus an aperture spatial filter placed in the Fourier plane of the hologram around the -1st diffraction order blocks out all other diffraction orders. After another Fourier transforming lens the image is created with uniform intensity and phase variation determined by

$\varphi(x,y)$. Figure 4.1(b) illustrates a Lee hologram, h(x,y), corresponding to the phase distribution shown in Figure 4.1(a).

4.3 Transmission matrix focusing

The transmission matrix focusing method[53] was selected for wavefront determination, because it uses a set of predefined phase masks and requires only three measurements per input mode. Using a predefined set of phase masks minimizes data transfer time between the DMD and the computer allowing the DMD to display all preloaded images at a maximum frame rate.

The observed transmission matrix (K_{obs}) is measured by calculating the complex field response for a set of given input basis modes. The Hadamard basis set is selected, because it can be represented as a phase basis with uniform amplitude. The complex field response is measured by interference between the Hadamard basis element and known phase reference beams. To minimize the number of measurements made, we use a three-phase method to recover the complex field[98], [99], instead of the four-phase method[53]. Each Hadamard basis element interferes with phase references of 0, π/2, and π displayed on the frame of each function as shown in Figure 4.1(a) and detected after propagation through the scattering medium. Furthermore, due to CCD frame rate limitations, we use a photodetector for high speed intensity measurements. This simplifies the transmission matrix measured into an Nx1 matrix, defined as the response of N input modes to a single output mode. The observed transmission matrix response for Hadamard basis element *n* is calculated with the intensity measurements at the output mode from all three phase references ($I^0, I^{\pi/2}$, and I^{π}) according to:

$$k_{obs}^{n} = \left(I^{\pi} - I^{\pi/2}\right)/4 + i\left(I^{0} - I^{\pi/2}\right)/4. \tag{4.3}$$

Once the observed transmission matrix is measured, the appropriate phase mask for creating a focus at the single output mode is calculated:

$$E_{in} = K_{obs}^{t} / \left| K_{obs}^{t} \right|, \tag{4.4}$$

where *t* represents the matrix transpose.

The three-phase reference transmission matrix measurement method can find a suitable phase mask after measurements of 3*N predefined phase masks, providing a 25 percent improvement in speed over the 4*N measurements previously used[53]. Numerical simulations show that, with experimental level noise, the overall signal to background enhancement is comparable to the enhancement achieved with four-phase references.

4.4 System

A collimated and expanded 532 nm laser illuminates the DMD (DLP Discovery Kit D4100), which consists of an array of 1024x768 mirrors, as shown in Figure 4.2. Each mirror is individually controlled to two angular positions, which are used to encode the binary amplitude Lee hologram. For our purposes we use N=256 or 1024 inputs to a single output mode defined by the photodetector. To implement the transmission matrix measurement method with the DMD we generate 768 binary amplitude holograms for N=256, or 3072 holograms for N=1024. Figure 4.1(a) shows an example phase distribution, with the centered Hadamard basis element surrounded by the reference. Figure 4.1(b) shows the resulting Lee hologram that generates the phase distribution in Figure 4.1(a). The experimental diffraction efficiency of the holograms with the DMD was 6-10% of the incident power. All holograms are loaded onto the DMD memory, which in conjunction with high speed software, allows for DMD control at maximum frame rate.

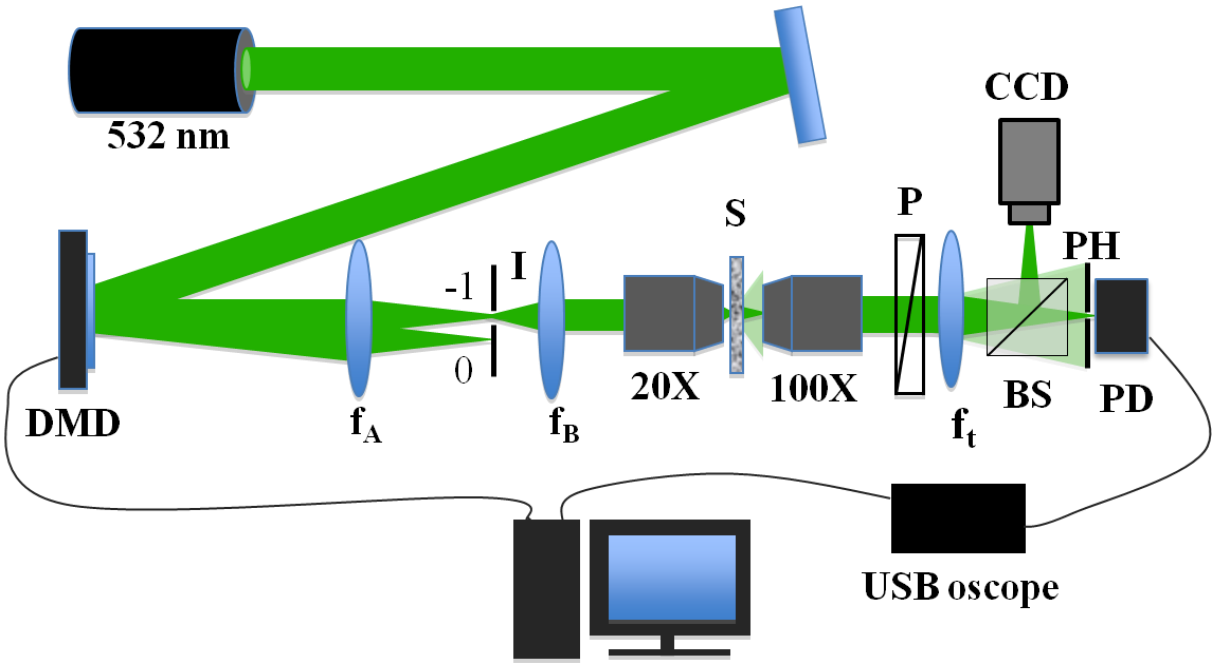

Figure 4.2. Diagram illustrating the experimental apparatus. A collimated 532nm laser beam is encoded with a Lee binary amplitude hologram by the DMD. The iris (I) passes the -1st diffraction order, which contains the hologram information, and blocks all other orders. The uniform amplitude, phase variation image is created at the back aperture of the 20X objective and focused onto the scattering sample. A 100X objective images a plane about a millimeter behind the scattering sample. This image is relayed to a pinhole placed before a photodetector. The photodetector signal is sent to a USB oscilloscope for A/D conversion before being processed by a PC to create a binary amplitude mask. A CCD and beamsplitter capture the focal spot image. DMD: digital micromirror device. fA, fB, and ft: lenses. I: iris. S: scattering sample. P: polarizer. BS: beamsplitter. PH: pinhole. PD: photodetector.

A Fourier transforming lens is placed one focal length away from the DMD. An iris placed after this lens in the Fourier plane blocks all diffraction orders, except for the -1st diffraction order, where the phase mask information is encoded. The -1st order light is then propagated through another Fourier transforming lens, which images the phase mask at the back aperture of a 20X (NA = 0.5) objective lens that focuses the beam onto the scattering sample. A 100X (NA = 0.75) objective images a plane ~1 mm behind the scattering sample onto a 50 μm pinhole placed before a photodetector. The back objective and the pinhole size are selected to

match the pinhole to the speckle size of the light scattered by the sample. The photodetector voltage is digitized and sent to the computer, where it is used to calculate the transmission matrix through the scattering material to the single output mode. A LabVIEW program controls all system computation and synchronization. By using a photodetector the intensity measurement is oversampled in time and an average value is used for the intensity measure to filter noise. A non-polarizing beamsplitter placed after the tube lens and before the pinhole creates a second image plane on a CCD array for imaging the focus spot.

4.5 Experiment

Using 120-grit ground glass (Edmund Optics, NT83-381) as the scattering medium we test the off-axis binary amplitude hologram focusing system. Each binary amplitude hologram is displayed on the DMD for 22 μs. With a switching time of 22 μs the total period for each mask is 44 μs (22.7 kHz). Thus, for N=256, all 768 measurements for transmission matrix determination occur in 33.8 ms. The photodetector signal is digitized and sent to the computer where the average intensity value for each measurement is used to calculate the transmission matrix of the system. Using the transmission matrix of the N input modes mapped to the single output mode, the phase conjugate mask is calculated and used to maximize the intensity of the light at the photodetector. The enhancement of the focus is calculated using the focus image taken with the CCD.

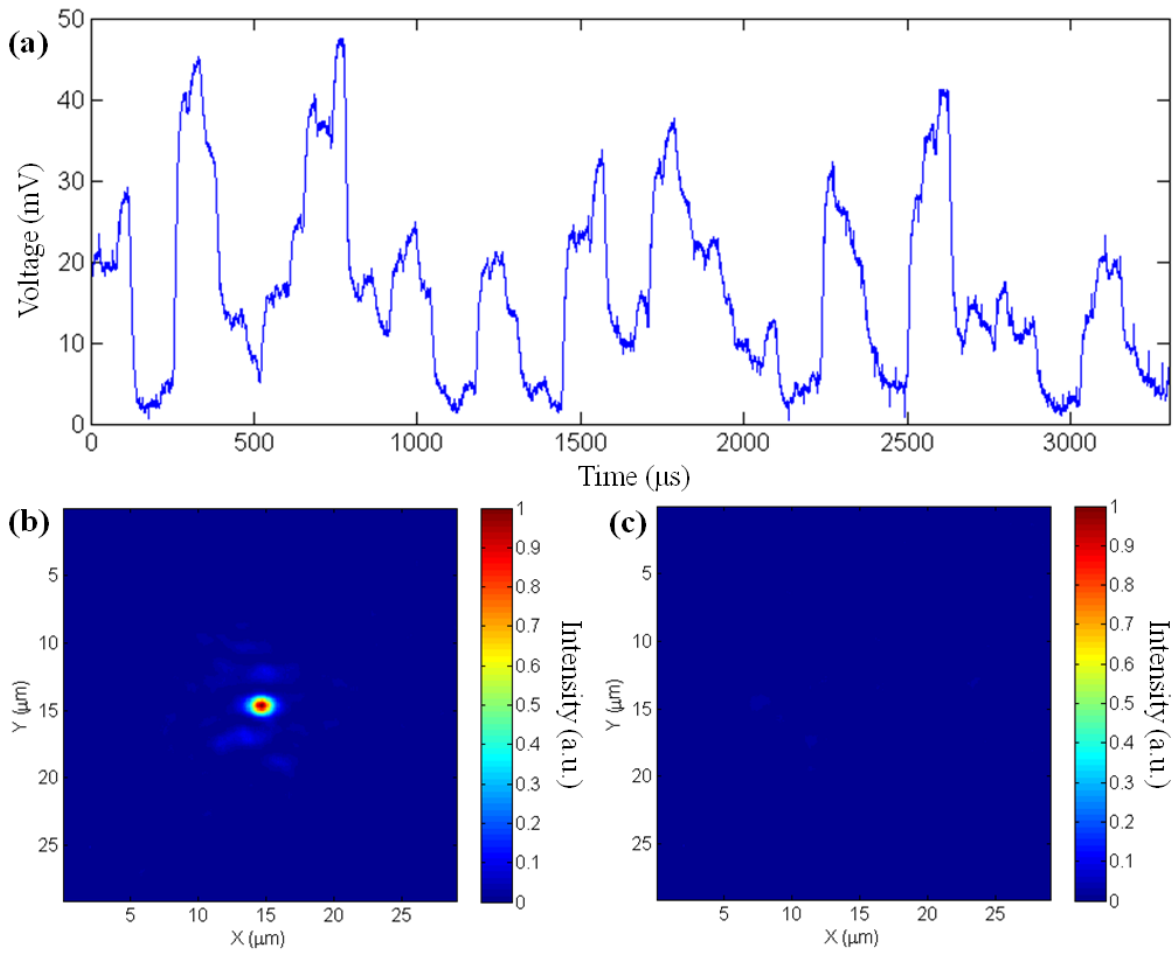

Figure 4.3. (a) First 3.3 ms of digitized sampling data from photodetector showing the intensity of the first 25 Hadamard basis modes interfered with three phase references. (b) Focus spot with enhancement of 450 created after optimization with 1024 modes. (c) Speckle field without the optimized phase mask.

Using this system we have demonstrated signal enhancements over the background intensity level of 164 and 454 with N=256 and N=1024 respectively. The values are comparable to enhancements obtained using a phase-only liquid crystal spatial light modulator[47], [53]. Interestingly, the intensity enhancement does not scale with N as predicted by theory in the ideal case, which is likely a result of phase hologram degradation for higher N due to the limited degrees of freedom of the DMD[97]. Figure 4.3(a) illustrates how the output mode intensity varies with each binary amplitude hologram. This is the sample data corresponding to the first 25

Hadamard basis elements and their three phase references. Figure 4.3(b) shows an example of a focus spot created through the scattering sample with 1024 modes, with signal enhancement of 450 over the background level, while Figure 4.3(c) shows the intensity distribution with a single Hadamard basis element and reference phase hologram on the DMD to illustrate the speckle field without optimization. With either 256 or 1024 input modes a focus spot with FWHM of 1.0 μm is created, which is comparable to previous reports with the same scattering sample[51], [65].

4.6 Focusing through dynamic turbid media

To explore the implication of dynamic changes of the transmission matrix in focusing through multiply scattering turbid materials with the off-axis binary amplitude technique, the algorithm was run with temporally dynamic turbid media of various speckle decorrelation times. For this experiment a 785 nm laser was used with the previously described system with N=256 input modes. The samples were prepared using varying amounts of Gelatin and water to create semifluid materials with Intralipid added as a light scatterer. These were 1 mm thick and had mean free path of ~200 μm. Given that the system run time between the start of measuring the TM to when the optimized mask displays is ~300 ms (Figure 4.4(f)), speckle decorrelation times greater than 300 ms were investigated, namely 350 ms, 650 ms, and 850 ms. The speckle decorrelation times were determined through the method described in Section 4.11. The measured average peak enhancements were 28, 54, and 69, respectively (Figure 4.4(a)-(c)).

Figure 4.4(f) shows the timing of the system. The first 34 ms have the lowest enhancement and correspond to the measurement time of the TM when the DMD mirrors are moving quickly and less light arrives at the focal plane. This is followed by a 270 ms interval with measured enhancements of one. This corresponds to the time spent transferring the

measurement data between the USB oscilloscope and computer, followed by data transmission of the optimized focusing phase mask to the DMD. During this time the DMD has the last mask from the TM measurement displayed which creates a random speckle at the output. Note that as an alternative, one could place the previous optimal mask on the DMD instead, in order to keep a high enhancement. The last part of the cycle, the 200 ms high enhancement, corresponds to the time when the optimized wavefront is encoded with the DMD. The enhancement can be seen to decrease during this time due to the short speckle decorrelation time. This process continuously repeats creating a bright focus twice per second.

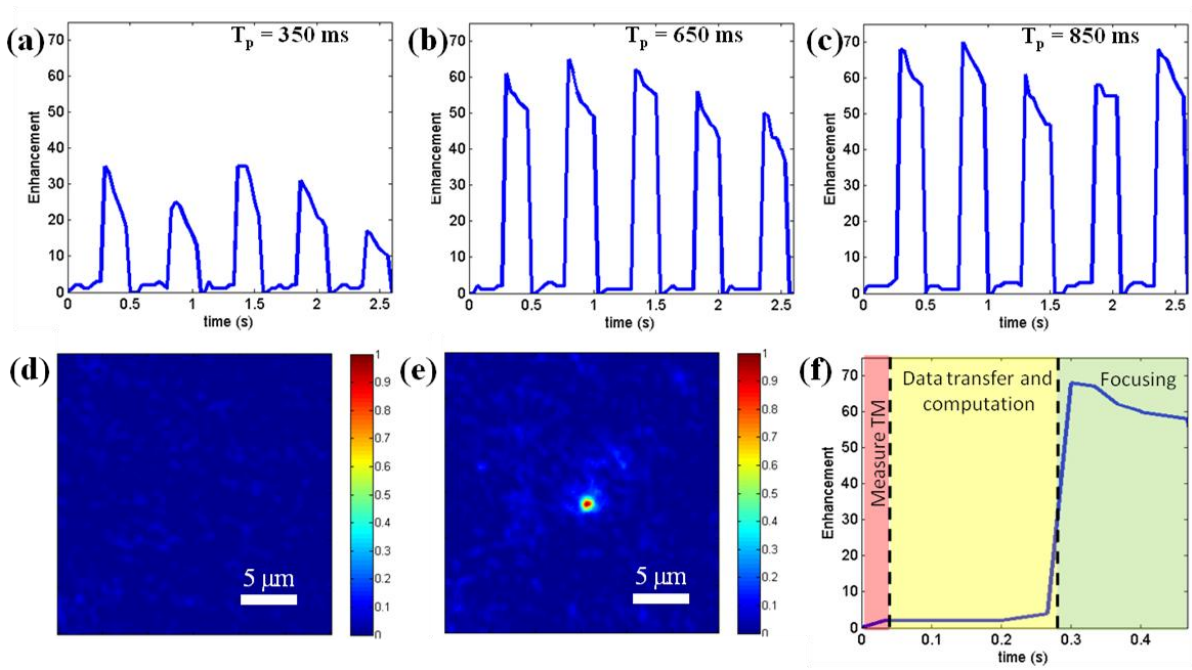

Figure 4.4. Enhancement of the focus spot versus time with temporally dynamic turbid samples of speckle decorrelation times: (a) 350 ms, (b) 650 ms, and (c) 850 ms. (d) Speckle field before optimization. (e) Focal spot after wavefront optimization through turbid sample with T_c = 850ms. (f) The timing of the system: Measure transmission matrix (TM): 34ms (red). Transfer data to computer, compute new mask, and transfer data to DMD and project: 270 ms (yellow). Display optimized binary amplitude mask: 200 ms (green).

4.7 Discussion

We have demonstrated high speed wavefront optimization for focusing through turbid media using a DMD with off-axis binary amplitude holography for phase control and the transmission matrix method adapted to the task. We measured the transmission matrix using a three-phase method and a single photodetector to decrease the total measurement time. With this approach we demonstrated an order of magnitude improvement in measurement speed over the current fastest wavefront determination method[65] and three orders of magnitude improvement over LC-SLM methods[47]. We also demonstrated focusing through temporally dynamic turbid materials with speckle decorrelation times similar to the system focusing time. The system focusing time is limited by the transfer of data from the USB oscilloscope to the computer and to the DMD board and does not represent a fundamental limit. In Sections 4.8 and 4.9 state of the art custom electronics are used to eliminate the speed limitation imposed by data transfer and computation.

4.8 FPGA algorithm implementation

In order to overcome the data transfer and computation limitations imposed by the system in the previous sections, the computation was accomplished directly on the DMD controller board. To calculate the optimized phase mask for focusing through turbid media, a three reference phase transmission matrix algorithm[100] was implemented directly on the Virtex5 FPGA, APPSFPGA, which is included in the DLP4100 kit. This optimization algorithm requires only three measurements per input mode for optimization and uses predetermined phase masks for input mode measurement, thus simplifying its implementation. Executing the algorithm on the FPGA allows for high-speed, parallel data processing. APPSFPGA utilizes the DDC4100

(Digital Data Controller) which projects patterns on the DMD (Digital Mirror Device) via the DMD power and reset driver, DAD2000. The analog voltage signal from the photo detector is digitized using a customized separate circuit board, the analog to digital convertor (ADC) daughterboard, which contains a fast ADC with a buffered analog input. APPSFPGA is responsible for accurate triggering of the analog conversion while computing and projecting phase modulating patterns at high speed. A black box approach was used for verification of the transmission matrix algorithm using two emulators, one for the DDC4100 and the other for the DMD. While the DDC4100 emulator verified correct functional and timing behavior of the APPSFPGA, the DMD emulator verified that the projected patterns and the focus mask are correct. Figure 4.5 shows a high level block diagram of the high speed focusing system from a hardware implementation point of view.

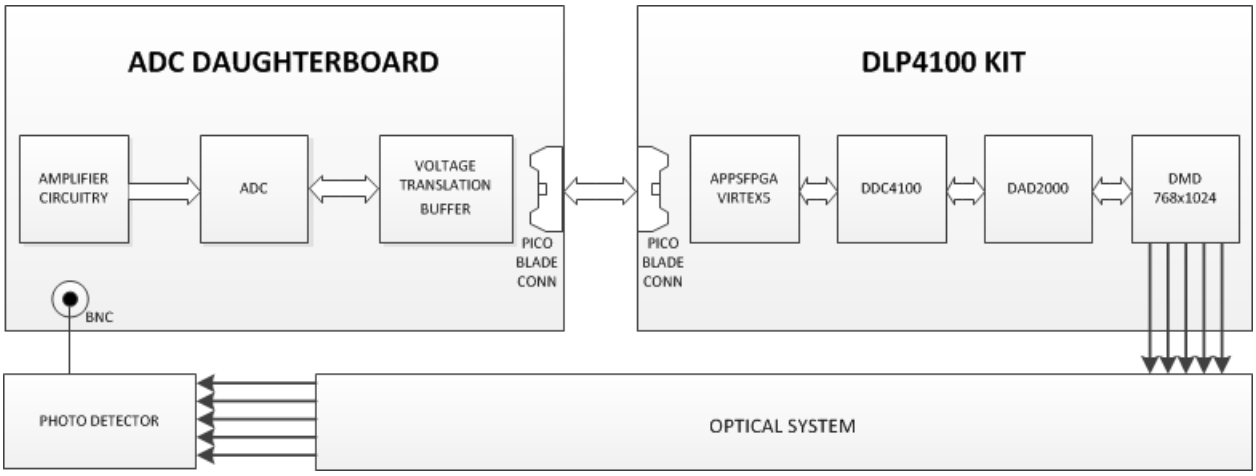

Figure 4.5. Block diagram illustrating the hardware implementation of the focusing algorithm.

4.9 Demonstration

4.9.1 System

The optical system utilized for this demonstration is essentially the same as the one described in Section 4.4 with the notable exception that an FPGA is used for computation as shown in Figure 4.6. In this case the photodetector voltage signal is sent to a custom built 8-bit analog/digital converter and sent to the DLP Discovery Kit, where the data is used by the FPGA to calculate the transmission matrix through the scattering material to the single output mode. By using a photodetector the intensity measurement is oversampled in time and an average value is used for the intensity measure to filter noise.

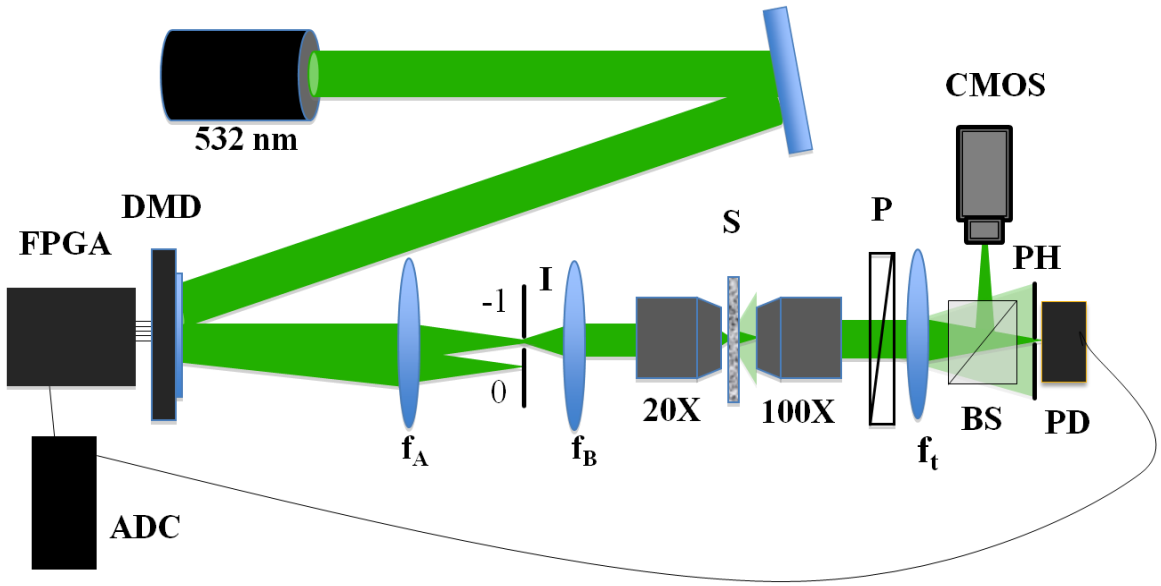

Figure 4.6. The experimental apparatus. A collimated 532nm laser beam is encoded with a Lee binary amplitude hologram by the DMD. An iris (I) passes the -1st diffraction order, which contains the hologram information, and blocks all other orders. The desired phase image is created at the back aperture of the 20X objective and focused onto the scattering sample. A 100X objective images a plane about a millimeter behind the scattering sample. This image is relayed to a 50 μm pinhole placed before a photodetector. The photodetector signal is sent to an ADC for A/D conversion before being processed by an FPGA to create a binary amplitude mask. A beamsplitter and CMOS capture the focal spot image. DMD: deformable mirror device. f_A, f_B, and f_t: lenses. I: iris. S: scattering sample. P: polarizer. BS: beamsplitter. PH: pinhole. PD: photodetector.

With the FPGA implementation the system can calculate a phase mask and project the optimized wavefront in ~37 ms. Measuring the response of the 768 wavefronts for the 256 input modes takes 34 ms. An additional 3 ms is all that is required for calculating the Lee hologram of the optimized phase mask, a significant improvement over using a computer for data processing as described in the previous chapter[66].

4.9.2 Focusing experiment

Dynamic tissue phantoms were created for studying the ability of the system to overcome highly temporally varying scattering materials. The samples were prepared using different amounts of Gelatin and water to create semifluid samples with Intralipid added as a light scatterer. These samples were 1 mm thick and had no ballistic light detected propagating through them. Given that the system run time between the start of measuring the TM to when the optimized mask displays is ~37 ms, speckle decorrelation times ranging from 10 ms to 200 ms were tested. Here we present the data from the samples with 12 ms, 26 ms, and 85 ms speckle decorrelation times (T_c) as determined by the method described in Section 4.11. The measured average peak signal to background ratio (SBR) of the focus spots were 14, 21, and 90, respectively (Figures 4.7(a)-(c), note that the vertical scales are not equivalent). The figures also illustrate the process the algorithm runs through. During the one second of data collected the algorithm repeats thirteen times, creating a bright focus for half of the time. With the more dynamic samples the focus exhibits itself as more of a spike in intensity as the transmission matrix quickly changes and the optimized phase mask no longer creates a focus. As expected, the more dynamic samples also have lower SBR. In these situations the earliest input mode measurements become obsolete before the optimized phase mask is displayed. Ideally the

number of input modes optimized would be matched to the speckle decorrelation time of the sample.

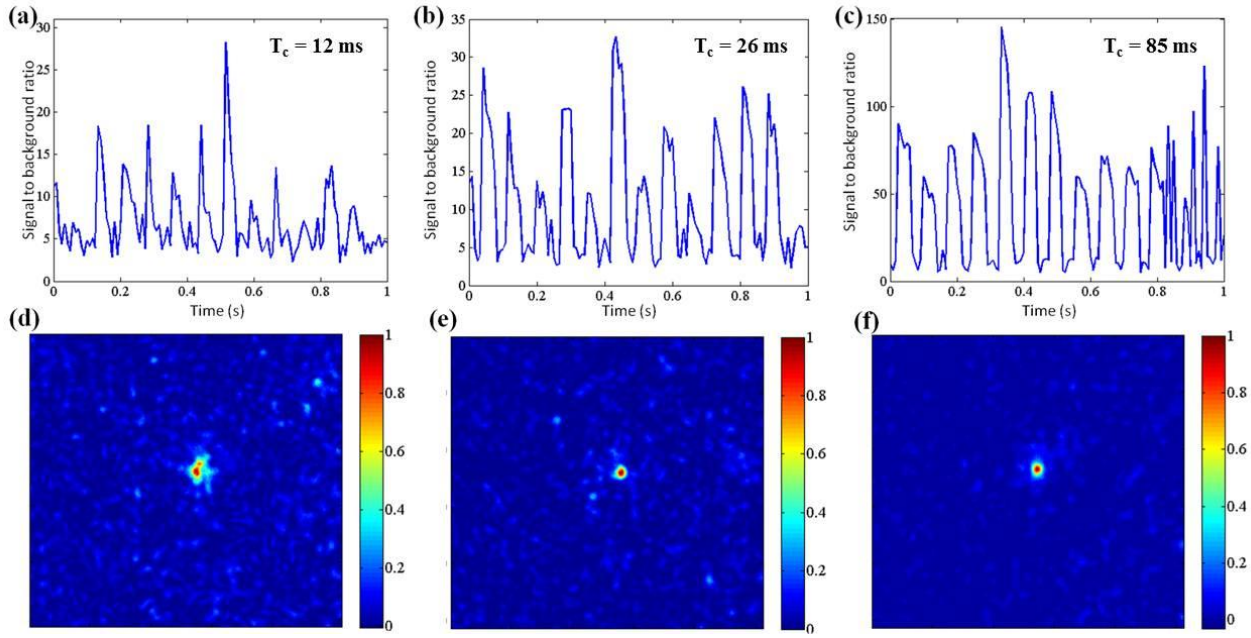

Figure 4.7. One second of data showing the temporal dependence of the signal to background ratio of focus spots created through dynamic tissue phantoms with speckle decorrelation times of (a) 12 ms, (b) 26 ms, and (c) 85 ms. NOTE: the vertical scales are not equivalent. Example images of the focal spot are shown in (d), (e), and (f), respectively.

4.10 Conclusions

By implementing a turbid media focusing optimization algorithm onto the DLP Discovery Kit FPGA, we can measure and focus through turbid media at speeds an order of magnitude faster than previously demonstrated[66]. The DMD allows for high-speed modulation of the wavefront through encoding off-axis binary amplitude CGHs, while the FPGA allows for high-speed calculation and projection of the optimized wavefront. We demonstrated focusing through temporally dynamic turbid materials with speckle decorrelation times similar to highly dynamic biological materials, such as tissue. Based on its speed, the binary amplitude holographic technique could find application in sensing and imaging of biological materials. By

measuring seven basis modes per millisecond this method should have enough speed to overcome the fast speckle decorrelation times of biological samples and generate enough focusing power for a variety of biomedical sensing and imaging applications.

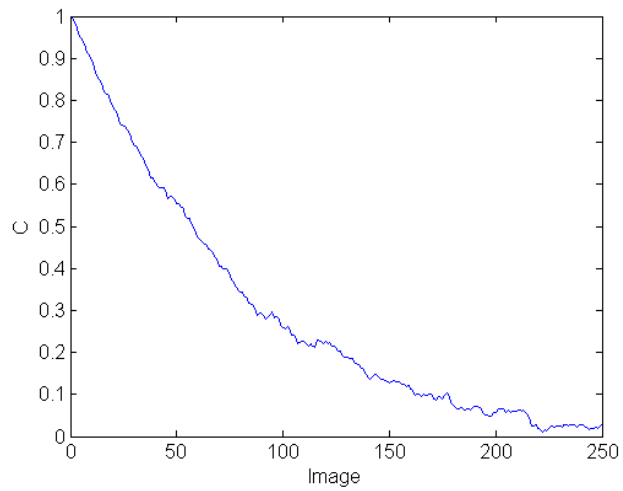

Figure 4.8. An experimental example of the cross correlation (C) between an initial speckle pattern and subsequent speckle patterns in dynamic turbid media.

4.11 Appendix: Measuring the speckle decorrelation time

The speckle decorrelation time is measured by capturing a sequence of speckle images through the dynamic turbid media. Each captured image is compared to the initial frame, at t = 0, through a cross correlation:

$$C(\tau) = \frac{\sum_i \left[I_i(0) - \overline{I(0)} \right] \left[\left[I_i(\tau) - \overline{I(\tau)} \right] \right]}{\sqrt{\sum_i \left[I_i(0) - \overline{I(0)} \right]^2} \sqrt{\sum_j \left[I_j(\tau) - \overline{I(\tau)} \right]^2}}. \tag{4.5}$$

I_i is the intensity of pixel i, I_j is the intensity of pixel j, and $\overline{I(\tau)}$ is the average intensity of every pixel in the image from time τ. An experimental example of the cross correlation evolution in a dynamic turbid sample is shown in Figure 4.8. The exponential decay shown in the cross

correlation with subsequent images (or time) determines the speckle decorrelation time, T_c, through:

$$C = e^{-\frac{1}{T_c}t}. \tag{4.6}$$

Thus, T_c corresponds to the time at which $C = 1/e$.

CHAPTER 5

REAL-TIME RESILIENT FOCUSING THROUGH A BENDING MULTIMODE FIBER

5.1 Introduction

The previous chapters have described light control through scattering media with the motivation of increasing the wavefront optimization speed through novel optimization algorithms and wavefront shaping implementations. The light control through turbid layers method is based on the division of the input and output fields into spatial modes, along with the iterative optimization of a merit function to optimize the speckle field to a single bright focus or image. Controlling light through turbid layers works because upon propagation through the turbid layer, the input modes become scattered and mixed such that each input mode contributes to every output mode. Thus, by optimizing the relative phase of the input modes to constructively interfere at the output modes the speckle field intensity can be shaped. Interestingly, light propagation through multi-mode fibers (MMF) yields a speckle field similar to the one produced when light propagates through scattering media, even though it is the result of significantly different interfering modes. Consequently, similar techniques have been adopted lately to overcome mode dispersion and coupling in multimode optical fibers[101]–[106]. Just as

the dynamic nature of tissue will create a time-varying speckle pattern, which necessitates a high-speed wavefront optimization to overcome, the speckle pattern in MMFs will vary with temperature and fiber bending. Thus, the technique described in Chapter 4 is directly applicable to light control through a bending MMF and are experimentally verified in this chapter.

In the 1970's, Yariv et al. provided a theoretical description of image transmission through optical fibers[107], [108] and several groups proved the concept later on[109], [110]. Lately, there has been a renewed interest in the topic sparked by new spatial light modulator (SLM), camera, and computation technical capabilities. For instance, Bianchi et al.[101] demonstrated the generation of multiple spots through a MMF utilizing a liquid crystal (LC) SLM and Monte-Carlo algorithm searching for the optimal input phase mask. In Ref.[102], [103] digital optical phase conjugation generates a sharp focus at the output of a MMF which can be scanned for imaging. However, the speed of this system is limited by the refresh rate of the SLM, camera acquisition and processing time. Furthermore, digital holography requires a reference brought through a different channel outside the fiber itself. Other techniques use a transmission matrix (TM) approach allowing bright and dark field imaging[104]. Alternatively, the TM information can be combined with averaged speckle imaging to attain widefield imaging[105]. Random pattern projection followed by optimization of the measurements provides an increased resolution[106]. Importantly, all these techniques rely on a pre-calibration of the optical fiber that typically takes several minutes, after which the fiber should not experience any significant physical change, thus precluding their use in a perturbation prone environment.

Most MMF biomedical applications require placing the fiber within tissue involving shape and temperature changes that produce modifications in the spatial configuration of optical modes. However, it should be emphasized that all these techniques developed for imaging or

focusing through MMFs[101]–[106] are contingent on avoiding any significant disturbance to the fiber during the experiment. Furthermore, a significant issue that limits real time implementation is the latency of the communication between the photodetector, the computer controlling, the experiment, and the SLM. Therefore, we introduce a real-time phase mask optimization through a MMF using a TM measurement technique[53]. The algorithm is implemented in a field programmable gate array (FPGA), which controls a DMD at full speed, improving one order of magnitude the overall focusing time with respect to the previous system that was applied in scattering materials[66]. As a result, we overcome fiber perturbation effects at video frame rates.

In Section 5.2 we describe the optical and embedded system, in Section 5.3 the experimental results, and in Section 5.4 we discuss the implications of this work.

5.2 Method and experimental setup

5.2.1 System

The setup of the system is shown in Figure 5.1. A 532 nm collimated laser beam illuminates a 1024x768 binary amplitude digital micromirror device (DMD TI-DLP Discovery Kit D4100). Each mirror can be controlled to two different angular positions, essentially creating a binary amplitude image. To control the phase of the beam, a binary amplitude Lee hologram[97] encodes the desired wavefront with the DMD. A lens, f_1, placed one focal length away from the DMD, Fourier transforms the hologram and an iris in the Fourier plane blocks all the diffraction orders except the -1st, which encodes the information of the desired phase distribution. The lens f_2 is used to image the phase mask on the back focal plane of a 10X

(NA=0.25) objective that couples the light into a 365μm core diameter MMF, 0.22 NA (BFL22-365-Thorlabs), which can propagate an estimated 1.1×10^5 modes.

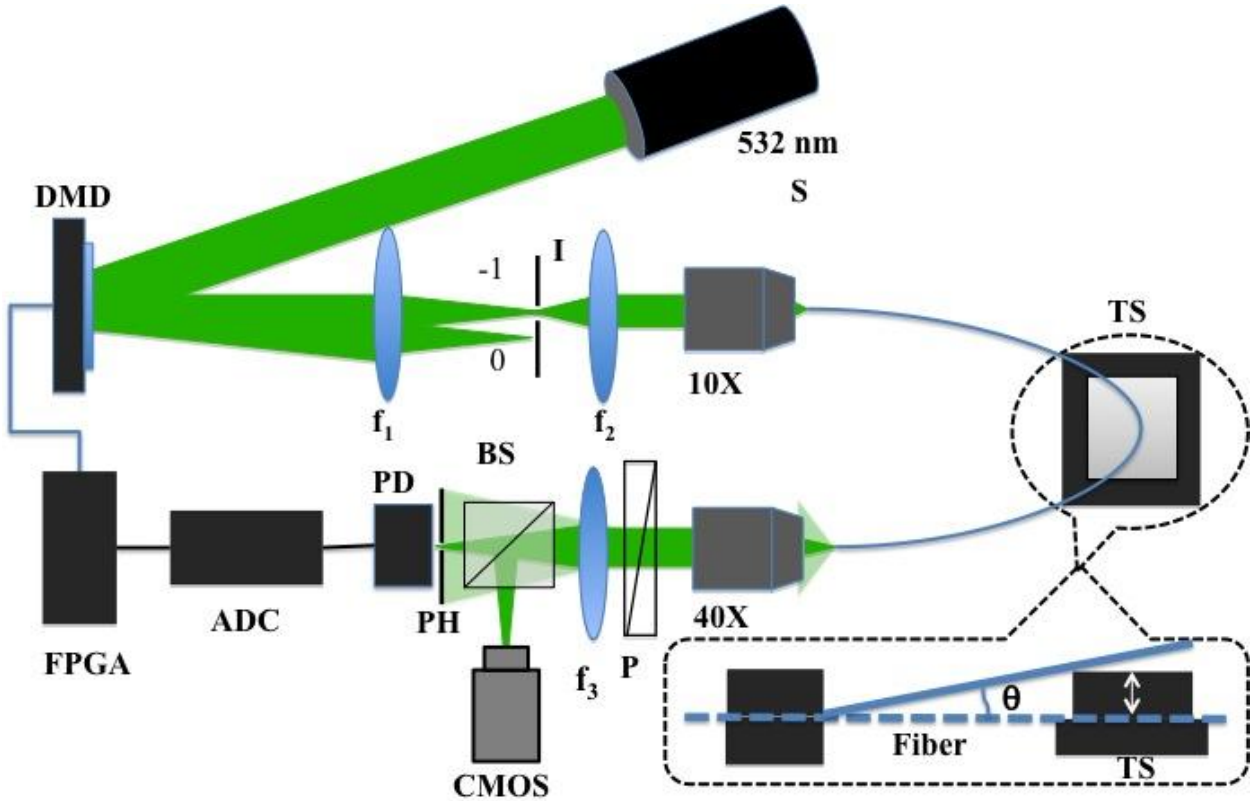

Figure 5.1. Diagram of the experimental setup. A 532 nm laser beam is encoded with a binary amplitude Lee-hologram displayed on the DMD. The iris placed between lenses f_1 and f_2 lets through the -1 diffraction order, which carries the encoded information; and is imaged in the back aperture of the objective. The phase mask is focused into the fiber and the output of the fiber is imaged by the f_3 lens onto a pinhole in front of a photodetector, whose signal is fed back into the FPGA controller. A CMOS camera images the output plane for monitoring but is not part of the focusing system. The inset shows how we characterize the bending angle. TS: translation stage; BS: Beam splitter; PD: Photodetector; C: CMOS Camera; P: Polarizer; f_1, f_2, f_3: lenses.

At the output of the MMF, the light is received by a 40X (NA=0.65) objective which images the surface of the fiber onto a 50μm pinhole placed before a photodetector. The objective magnification and the pinhole size are chosen to match the pinhole diameter to the speckle spot size at the image plane. To control and characterize the movement of the fiber, we use an

automated translation stage that bends the fiber by a measurable angle, θ, defined in the inset of Figure 5.1.

A beam splitter placed after the tube lens and before the pinhole creates a second image plane on a CMOS camera (Hamamatsu ORCA Flash 2.8) which enables high frame rate video recording for data analysis and speckle decorrelation measurement. The photodetector signal is digitized by an analog-to-digital converter (ADC) triggered by the customizable FPGA on the DMD controller board. The intensity values are temporally oversampled and the average value is used to build the hologram with the optimal phase mask encoded to produce the focus spot.

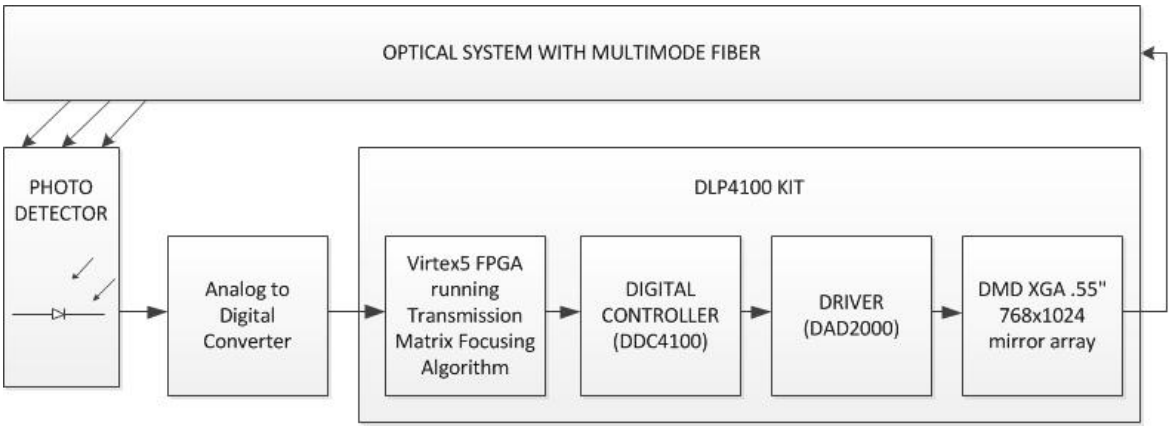

Figure 5.2. Block diagram of hardware implementation. Light propagates through the optical system and comes out of the MMF reaching the photodetector. The signal is digitized and sent to the DLP4100 kit. The FPGA runs the algorithm with the measured data.

5.2.2. Transmission matrix implementation in FPGA

For real-time experiments, a hardware implementation is often necessary to reduce latency and computation times. As discussed in Section 4.8 a phase shifting method based on three measurements per input mode for TM determination[53], [112] is implemented directly on a Virtex5 custom FPGA, APPSFPGA, which is included in the DLP4100 Discovery Kit. A separate analog-to-digital converter (ADC), with a buffered analog input, digitizes the signal and provides the input to the FPGA board. Figure 5.2 shows a high-level block diagram of the

hardware implementation of the TM focusing system. This configuration is independent of an external computation source and therefore able to toggle the DMD at the maximum frame rate. As a result, the system enables the measurements of the amplitude and phase corresponding to 256 different input modes (with three different reference phases per input mode) in 33.8 ms, corresponding to an update frequency of 22.7 kHz. Processing this information to construct the optimal phase mask, then sending to and projecting on the DMD adds an additional 3 ms. The optimized, focusing phase mask projection time can be varied based on experimental conditions. For this experiment we match focusing time with the measurement time: 37 ms, which provides a 50% duty cycle and allows for repetitive focusing at a constant rate of 13Hz.

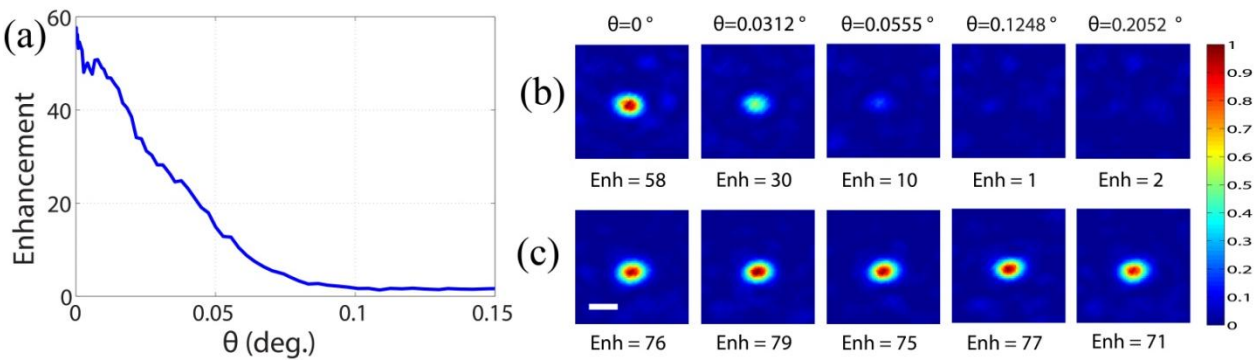

Figure 5.3. Demonstration of bending resilient focusing: (a) Experimental measurement of the focus degradation as a function of bending angle without active wavefront control. (b) Cross-section of the output intensity of the fiber without running the adaptive wavefront correction, and (c) with adaptive wavefront correction. The focus spot enhancement is shown at the bottom of each cross-section. Scale bar indicates 8μm.

5.3 Experiment and results

To quantify the performance of the system, we bend the fiber with different speeds and accelerations to create a dynamic environment. Bending the fiber alters the mode coupling within the fiber; this is manifested by a speckle pattern change at the fiber output. The speckle pattern change is quantified by measuring the 2D correlation between the speckle pattern associated with a bent fiber and a straight fiber. By analyzing the correlation between captured speckle image

frames from the CMOS using a static input illumination, the average decorrelation time associated with each setting of the stage is obtained.

To illustrate the sensitivity of the fiber to spatial changes, we measure the focus degradation as the fiber is bent without adaptive correction. In Figure 5.3(a) we observe how by displacing the fiber less than 0.1 mm, corresponding to bending the fiber just 0.09º in our configuration, the focus completely disappears. This illustrates the high sensitivity of our fiber to spatial displacements due to mode coupling. To demonstrate the performance of the system, we compare the degradation of the focus spot for two cases: a) with a static phase mask, and b) with adaptive wavefront correction. Figures 5.3(b) and (c) shows the output field intensity of the fiber taken by the camera at different positions of the translation stage. Figure 5.3(b) illustrates how bending the fiber quickly degrades the created focus when the phase mask is not re-optimized. In Figure 5.3(c), the image is shown at the output of the fiber with the adaptive system on. The stage moves with an initial acceleration of 2 mm/s^2 until reaching a constant velocity of 1 mm/s, corresponding to an average speckle decorrelation time of 150ms. Despite the fast rate of change, the focus enhancement remains high and stable. Note that the enhancements at θ=0º in Figure 5.3(b) and (c) do not match because the enhancement achieved is highly sensitive to the initial conditions.

To test the efficiency of the system, we track the dynamics of the focus enhancement as a function of time as the fiber bends, as shown in Figure 5.4 (blue line). The zone delimited by the red line corresponds to the interval when the stage is moving. The bending angle of the fiber as a function of time is represented in green. We observe that the enhancement is constant while the stage is not moving. Once the stage starts moving, we observe that the enhancements achieved with the bending fiber are smaller and more variable than with a static fiber, which is due to the

dynamics of the transmission matrix; the result of performing measurements while the system is changing.

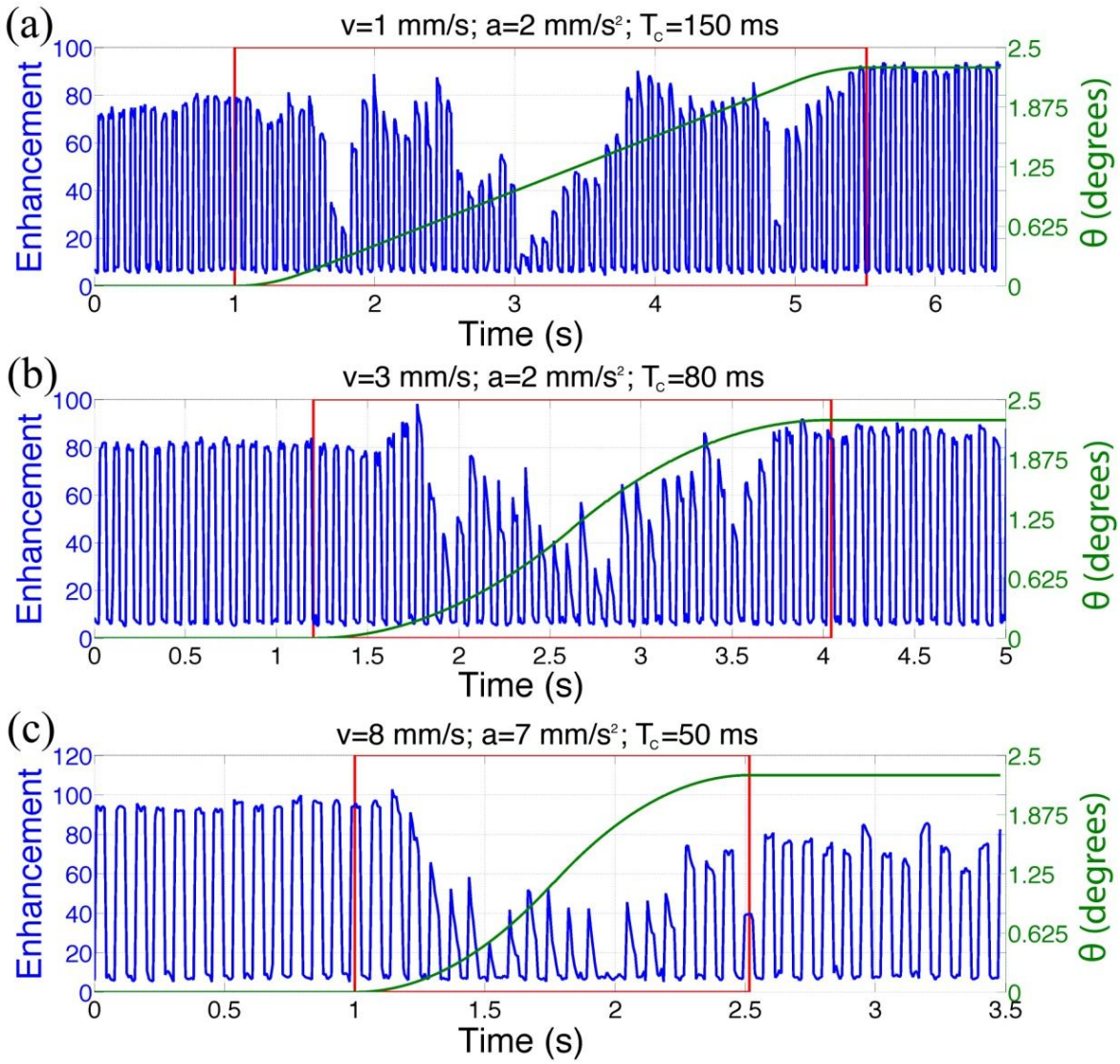

Figure 5.4. Enhancement of the focus as a function of time for different average decorrelation times as determined by the speed of bending of the fiber: (a) 150 ms, (b) 80 ms, (c) 50 ms. The red lines delimit the period during which the fiber is being bent. The angle of bending is shown in green. v: velocity of the stage, a: initial acceleration of the stage. T_c: Average decorrelation time of the settings.

It is worth noting that even for an average decorrelation time of 50 ms, close to the system cycle time (37 ms), the enhancement obtained does not fall too low, with values around 40. In this case, some of the modes measured have changed after 37 ms, which is the period from the first measurement to the projection of the optimal phase mask, explaining the lower enhancement. Furthermore, a higher number of input modes could be used to increase the enhancement as a tradeoff to speed. Note also that while we present small angle bends because of the range limitation of the automated translation stage, larger angle perturbations have been tested with a manual stage leading to similar enhancement.

5.4 Discussion and conclusion

We have demonstrated real-time focusing through a dynamically bending MMF. In these experiments we used a fiber with more than 100,000 propagating modes to demonstrate the concept. A smaller diameter fiber, which would propagate fewer modes allowing for a larger bending angle before total speckle decorrelation, could also be used. The system creates a focus in 37 ms at the output plane of the fiber leading to enhancements between 50 and 100 during fiber perturbation. As a result of the known relationship between number of modes and focus enhancement, faster operation could be achieved at the expense of enhancement factor. The FPGA implementation enables the system to perform at a constant rate of 13Hz with a 50% duty cycle. The FPGA operation is totally configurable and the phase mask update protocol could be adapted to the application. For example, different algorithms allowing steady state focusing[67] and existing imaging modalities[58], [102]–[106] could be implemented. The system can have applications in photodynamic therapy where localized energy delivery is needed. A very similar

system can be modified for use with dynamic scattering materials, like biological tissue, possessing decorrelation times on the order of ~10 ms[66].

Ongoing research is exploring different feedback mechanisms that can substitute the photodetector at the end of the fiber. For instance, the system could be adapted for imaging purposes by introducing a sparse fluorophore population in the output plane and using the emitted light for feedback[81], or using opto-acoustic effects as demonstrated in scattering media[73].

CHAPTER 6

HIGH CONTRAST, THREE-DIMENSIONAL PHOTOACOUSTIC IMAGING BY LOCALIZED OPTICAL FLUENCE ENHANCEMENT

6.1 Introduction

The introductory chapter discussed two limitations which must be overcome in order for light control through turbid media to be a viable sensing and imaging technique in living biological tissue. The first of these, overcoming tissue dynamics, was addressed in Chapters 2 and 4 by increasing the speed of the wavefront optimization through algorithms and high-speed wavefront modulation. The second obstacle is focus creation without physical access inside or behind a scattering layer, which would be impractical in biomedical implementation. All of the experiments discussed previously in this thesis put a detector behind the scattering layer. As discussed in detail in Section 1.5.2, several approaches have been introduced to focus inside scattering layers without placing a detector inside. Notable among these are acoustic guide star approaches which utilize ultrasonic waves which propagate with three orders of magnitude less scattering than light in soft tissue[70]. Thereby, allowing them to penetrate much deeper with minimal scattering. These facilitate optical enhancement by creating an ultrasound guide star inside of the tissue. The guide star locally modulates the frequency of light crossing it. Upon

propagating outside of the scattering tissue these tagged photons are used to record the scattered optical field, which when phase conjugated, delivers photons back to the ultrasound focus[70]. Importantly, the size of the high optical intensity region is determined by the ultrasound transducer focus size.

A less explored feedback mechanism for focusing light through scattering materials is the photoacoustic effect. The photoacoustic effect produces acoustic waves as a medium absorbs light and undergoes thermal expansion[42]. The photoacoustic effect is used in modern photoacoustic microscopy to image at depth in tissue[43]. Photoacoustic microsocopy differs from ultrasound imaging in that its contrast stems from optical absorption, as opposed to mechanical properties. Photoacoustics allows, for example, imaging of the vasculature by using hemoglobin in blood as the absorbing medium[114]. Recently, the first demonstration of focusing through turbid media using photoacoustic feedback by Kong *et al.* demonstrated the capability of this technique, however no attempts at image reconstruction were made[73]. Very recently, photoacoustic feedback was used in measuring the transmission matrix through a scattering material onto light absorbing fibers. In this transmission matrix measurement the input optical modes were related to the absorbers found behind the scattering material. As a result, it was possible to localize particles along the axis of the transducer and create optical foci at the absorbers detected in the matrix. Unfortunately, none of these two early techniques has demonstrated imaging capability, so far.

Therefore, in this chapter we use a photoacoustic feedback optimized optical focus for creating an image of an absorbing medium behind a scatterer. Analyzing the temporal profile of the photoacoustic wave, we form a three-dimensional (3D) image after a two dimensional scan.

Remarkably, we achieve a significant improvement in signal-to-noise ratio of about one order of magnitude.

This chapter is organized as follows. Section 6.2 describes the experimental apparatus. Section 6.3 follows with a discussion of the data collection and reconstruction methods as well as the experimental results showing photoacoustic signal enhancement and three-dimensional images.

6.2 High contrast photoacoustic imaging system

The high contrast photoacoustic imaging system combines wavefront shaping, using a liquid crystal spatial light modulator (SLM), and an ultrasound transducer for measuring the photoacoustic signal. The SLM phase encodes the wavefront to maximize the intensity of light, while the transducer provides feedback for the iterative optimization algorithm (Figure 6.1). More specifically, an attenuated, expanded, and collimated 5 ns laser pulse (Continuum Surelight I20, 20 Hz repetition rate, Nd:YAG frequency doubled to produce 532 nm wavelength) illuminates the entire screen of a phase-only liquid crystal spatial light modulator (SLM) (Boulder Non-linear Systems, 512x512 pixels). After the SLM the energy per pulse in the beam is ~21 μJ. In practice the pulse energy is limited by the damage threshold of the SLM and (more importantly) the sample. A 4f system (f_1=150mm, f_2=250mm) images the SLM onto the back aperture of a long working distance microscope objective (Mitutoyo, 34 mm working distance, 5x magnification, 0.14 NA). The beam focuses into a water tank and onto the surface of the scattering material (glass diffuser, Edmund optics, 120 grit). An absorbing sample used for wavefront optimization and imaging is placed ~8 mm behind the scattering material and mounted to a 2D translation stage to allow for scanning in the x and y dimensions. The distance

between the sample and the glass diffuser is chosen to approximately match the size of one speckle grain with the size of the photoacoustic focal region. The photoacoustic signal produced by the sample propagates through the water and is detected by a 90 MHz transducer (Olympus, model V3512, 50Mhz bandwidth). The location of the transducer is chosen based on the geometry of the system. However, it could be placed on the same side as the illumination beam without loss of generality. After being pre-amplified (Femto HSA-X-2-40, low-noise 40dB), an oscilloscope records and digitizes the signal and sends it to a computer for analysis. In order to limit the size of the acoustic volume during the optimization process the signal is digitally high-pass filtered using a 2nd order Butterworth filter with a cut-off frequency of 80 MHz.

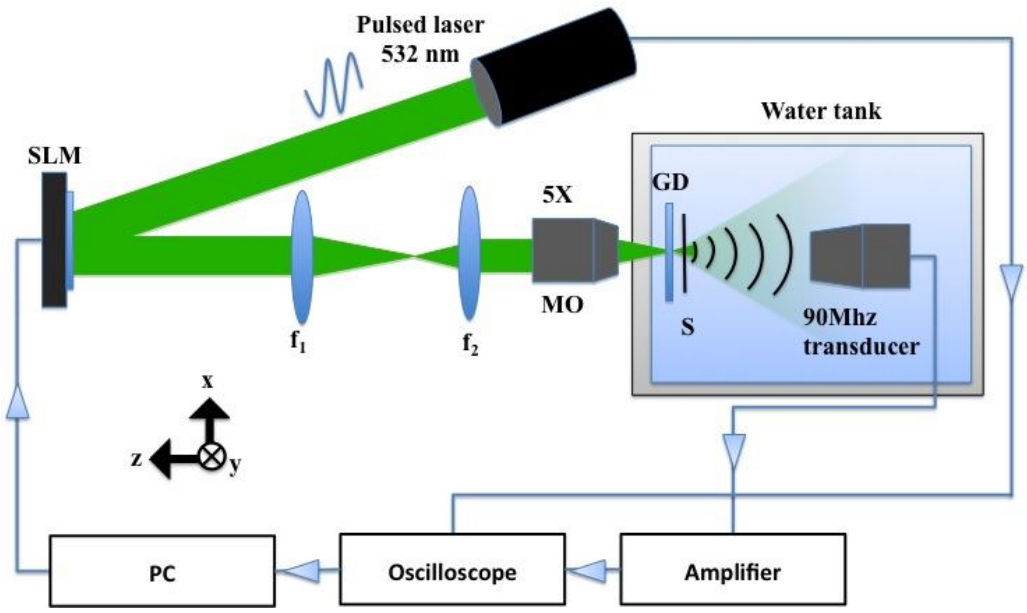

Figure 6.1. Experimental setup for localized fluence-enhanced 3D photoacoustic imaging. The sample is placed in a glass water tank. A 532 nm pulsed laser illuminates an SLM that controls the input wavefront focused through the glass diffuser. A 90 MHz ultrasound transducer detects the photoacoustic signal from a sample placed behind the scattering material. The signal is amplified and digitized before being analyzed in the PC. The coordinate axis defines the axis in the following figures. SLM: spatial light modulator; f_1, f_2: lenses; MO: microscope objective; GD: glass diffuser; S: sample.

The system maximizes the photoacoustic signal by modulating the wavefront with the SLM and using an iterative algorithm for optimization. We use a genetic algorithm (GA) for the optimization because it has been demonstrated to work well with low SNR signals[52], which is sometimes the case with photoacoustics. The GA cost function for the algorithm is the peak-to-peak voltage (proportional to pressure) of the acoustic signal. In general this signal depends on the absorber size, while in our case the absorber is much larger than the acoustic beam diameter so it does not affect the quality of the optimization process. Furthermore, during the optimization process, the absorber does not change, making the cost function depend only on the amount of light absorbed by the sample.

Using the feedback from the photoacoustic signal the GA finds a phase mask which maximizes the cost function and consequently the light intensity within the acoustic focus volume. After the optimization process the best phase mask is projected on the SLM to prepare for image scanning.

6.3 Photoacoustic enhancement and 3D imaging

6.3.1 Photoacoustic enhancement demonstration

As a first demonstration of the performance of the system, we test its ability to increase the photoacoustic signal produced inside a polypropylene tube (90 µm inner and 120 µm outer diameter) filled with India ink and placed behind a glass diffuser. The GA optimization runs through 1200 phase mask measurements, or 60 generations with a population size of 20 and 804 input modes, to find the optimal phase mask. As in [52] the mutation rate decreased as the optimization progressed. Figure 6.2(a) illustrates how the enhancement evolved as the optimization proceeded. Here we define the enhancement as the value of the cost function of the

projected mask divided by the mean of the cost function from each member of the initial population. An amplitude enhancement of 10 of the photoacoustic signal is observed, indicative of a 10-fold increase in absorbed light in the focal region. In Figure 6.2(b) and (c) the photoacoustic response for a flat phase and the optimized phase mask are compared. To minimize the noise of the photoacoustic signal we initially average 40 samples of the signal. As the signal strength increases the number of averaged samples decreases gradually to 5 in order to decrease the optimization time. As a result the signals in Figure 6.2(b) and (c) are taken with 40 and 5 averaged samples, respectively. The optimization process takes about 15 minutes, limited by the repetition rate of the laser. These figures show clearly the improvement in the photoacoustic signal produced using the GA optimization approach.

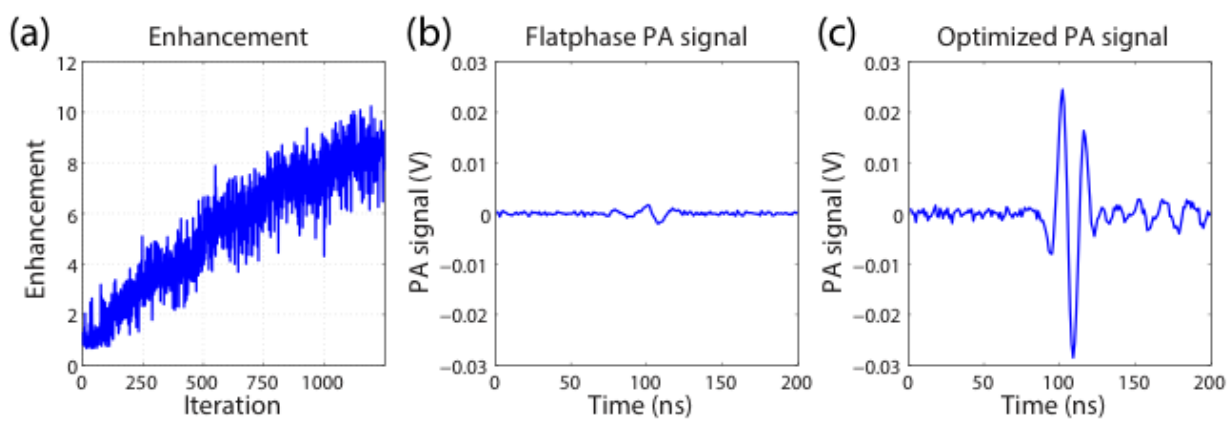

Figure 6.2. (a) Experimental photoacoustic enhancement evolution with the optimization process. (b) Photoacoustic amplitude signal for a flat input phase mask (40 averaged samples). (c) Photoacoustic amplitude signal for the optimal input wavefront (5 averaged samples).

6.3.2 High contrast image reconstruction

After verification of photoacoustic signal enhancement, we demonstrate 3D imaging with enhanced localized optical fluence. As a first demonstration we scan the sample around the optimized focus with the automated translation stage while keeping the scattering material at a

fixed location. The photoacoustic signal amplitude, recorded from each position (x-y plane, Figure 6.1), is processed to reconstruct the 3D maximum intensity projection of the two tubes (Figure 6.3(a)). The temporal profile of the photoacoustic signal (Figure 6.2(c)) encodes the z (axial) information. By sliding a window through the signal and selecting the maximum value for each window position many z values can be fixed to each x,y position to create the third dimension. The size of the window is determined by the axial resolution, δz, of the transducer, which comes from its bandwidth, B, and the speed of sound, c_s: $\delta z = c_s / B \cong 30\mu m$. The transducer also determines the transverse resolution of the acoustic beam: $BD(-6dB) = 1.02 \bullet Fc_s / Df \cong 36\mu m$ where BD is the acoustic beam diameter at the focus plane, F is the focal distance, D is the diameter of the transducer, and f is the central frequency. In these experiments we approximately match the size of the speckle with the acoustic BD during optimization. Hence, the resolution of our system is given by the speckle size at the transducer focal region.

A 2D slice is extracted from the 3D image to measure the distance between the two tubes. In Figure 6.3(b) the normalized 2D image corresponding to an intermediate plane shows the maximum photoacoustic signals from each tube are separated by 170 µm. From the size of the outer diameter we infer the tubes are 50 µm apart. A normalized 1D scan from the x=0.02 mm profile is shown in Figure 6.3(c). We observe the inner diameter is 50µm, significantly smaller than 90µm diameter given by the manufacture. This can be understood by considering that the photoacoustic feedback came from ink inside of the polypropylene tube. During the optimization, the wavefront correction accounted for the refraction of light produced by the polypropylene tube. In other words, the tube acted as a lens because of the higher index of

refraction (1.49) of the polypropylene tubing material. As the optical focus moved away from the center of the tube during the image scan procedure, the wavefront no longer matched the curvature of the tube and the focus inside the tube was destroyed, thus producing negligible signal at the tube edges. Despite this, the tubes are clearly defined with high absorption contrast. For comparison, the 3D, 2D, and 1D reconstruction with an unoptimized wavefront projected on the SLM are shown in Figure 6.3(d)-(f) respectively. In this case, the width of the two tubes and their separation agree with the actual tube size, although the SNR is more than 10 times lower than the optimized case. Figure 6.3(c) also compares the photoacoustic intensities (proportional to acoustic pressure squared) of the optimized and unoptimized scans.

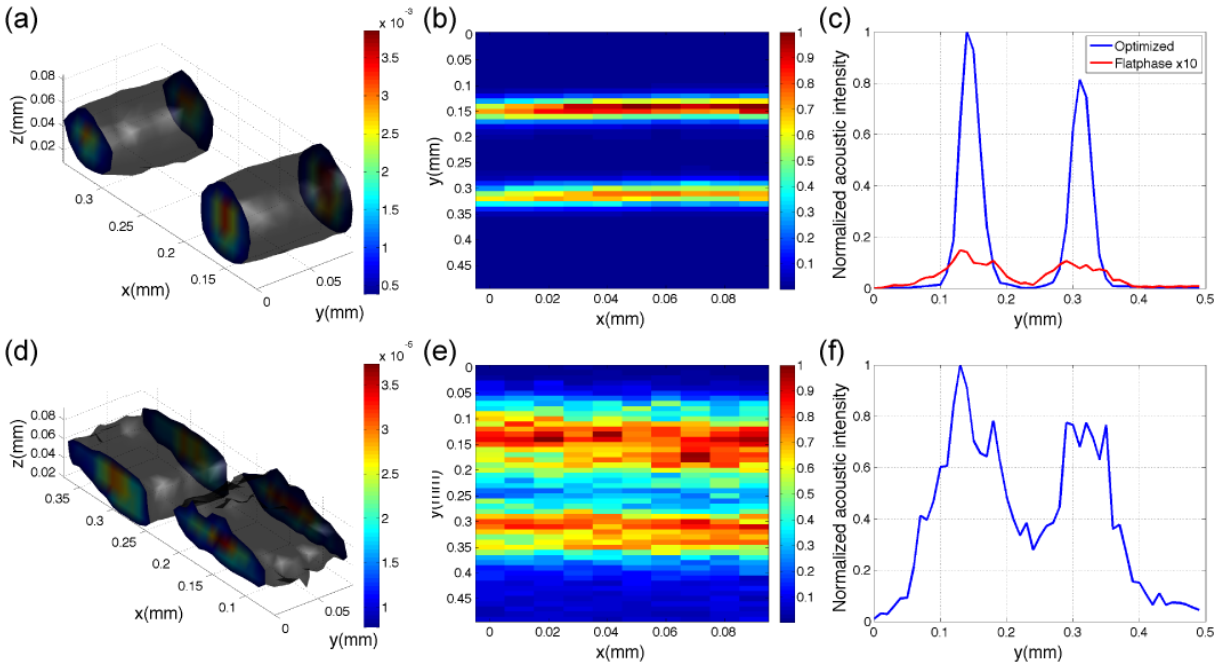

Figure 6.3. 3D imaging of two capillaries. First row corresponds to the optimized phase mask. Second row corresponds to a flat phase projected on the SLM. (a),(d) 3D scan with a 2% intensity threshold; (b), (e) 2D scan; and (c), (f) 1D scan of the capillary tubes.

6.4 Discussion and conclusion

We have demonstrated a one order of magnitude enhancement of the photoacoustic signal amplitude by GA optimization of the phase of the input wavefront to compensate for scattering and increase the optical intensity of light in the acoustic focus. This enhancement allowed for the imaging of two 90 µm inner diameter tubes with excellent signal-to-noise ratio as compared to a flat phase wavefront. Furthermore, by using the time of arrival information from the photoacoustic signal, the depth information was recovered and a 3D image reconstructed after scanning the sample in two dimensions.

In this experimental system we scan the sample around the focus because of the speed limitations imposed by the low repetition rate of the laser. With a higher repetition rate laser source and a faster wavefront modulation device[66], sub-second optimization of the input phase mask could potentially be enabled. This would open up the possibility of scanning the transducer instead of the sample and re-optimizing for each position, providing opportunities for *in-vivo* testing of biologically relevant samples and to increase the penetration depth of current photoacoustic microscopy techniques.

In conclusion, we have shown for the first time photoacoustic images created by locally enhancing fluence using wavefront shaping and hence the image signal-to-noise ratio. Furthermore, this is the first demonstration of imaging in three dimensions through a highly scattering medium (without using the memory effect[60], [115]) and without need to access the back side of the scatterer where the object is located.

CHAPTER 7

SUPER-RESOLUTION PHOTOACOUSTIC IMAGING THROUGH A SCATTERING WALL

7.1 Introduction

The previous chapter describes the use of a photoacoustic feedback to enhance the optical fluence through an ultrasound transducer focus. This system addresses a key to the practicality of any imaging technique by enabling the capability of focusing light without direct access behind the scattering wall. In this chapter the results of utilizing the photoacoustic system for increasing optical fluence via a genetic algorithm wavefront optimization are characterized. Interestingly, it is found that by combining the spatially non-uniform sensitivity of the ultrasound transducer to the generated photoacoustic waves with an evolutionary competition among optical modes, the speckle field develops a single, high intensity focus significantly smaller than the acoustic focus used for feedback. Notably, this method is not limited by the size of the absorber to form a sub-acoustic optical focus. We demonstrate imaging behind a scattering medium with up to ten times improvement in signal-to-noise ratio (SNR) and five to six times sub-acoustic resolution.

Recent advances in wavefront shaping have made imaging through scattering walls a possibility[11], [12], [60], [79], [81], [115]. By precompensating the optical wavefront, the light

propagation can be controlled through and beyond scattering materials[47], [53], [55], [116]. Most existing techniques, however, are limited by their need to generate feedback from behind or inside a scatterer with direct invasive access. Several recent techniques have overcome this limitation using acoustic waves, either with an ultrasound guide-star[70] or a photoacoustic feedback[73], [74]. Two modifications of the ultrasound guide-star method have allowed for the creation of an optical focus smaller than the acoustic spot size[71], [72]. Si et al.[71] frequency modulated diffuse light with a focused ultrasound transducer and then time reversed the encoded light using optical phase conjugation. Through iterative time reversal, a convergence of the light to the central region of the ultrasound focal volume where the modulation is the strongest was observed, resulting in an increase in the optical intensity in a sub-acoustic focal region. Alternatively, the time reversal of variance encoded light (TROVE) approach was also shown to break the acoustic resolution barrier by isolating the spatial location of optical speckles within the ultrasound focus[72]. While both of these techniques are promising for deep fluorescence imaging in scattering materials, their inherent low SNR could limit implementation

Photoacoustics, where acoustic waves are generated from optical absorption and subsequent thermal expansion, have also been used for wavefront optimization[73], [74]. In this case, the pressure of the generated acoustic wave is proportional to the light fluence. Hence, the detected photoacoustic wave provides a measure of the local light intensity, facilitating feedback and allowing for wavefront optimization. Only lately has imaging through scattering media been demonstrated using photoacoustic feedback[75]. Without optical focusing, photoacoustic resolution is determined by the ultrasound frequency and numerical aperture of the transducer. Considering a focused ultrasound transducer, uniform optical absorption excites acoustic waves throughout the focal region. However, as shown below, introduction of a scattering material

creates a non-uniform speckle field with separate and distinct speckle grains coherently combining to produce the photoacoustic response. Previous work using photoacoustic feedback with wavefront shaping has assumed that this feedback would create an optical focus limited by the size of the acoustic focus[73], [74]. With this assumption, a smaller optical focus could be created only when optimizing with sub-acoustic sized absorbers as targets[74].

In this chapter we demonstrate that by introducing a scattering element into the optical illumination path both SNR and resolution can be improved with wavefront shaping, enabling super-resolution imaging. To accomplish this, the optical intensity of the speckle field within the transducer focus is redistributed to create a single overpowering speckle smaller than the ultrasound transducer focus. Thus, the speckle acts as an optical focus and improves both photoacoustic emission and resolution, effectively allowing optical resolution photoacoustic microscopy[117] deep through scattering media. Such capabilities enable superb three-dimensional (3D) imaging of complex biological structures.

7.2 Theory

Optimizing a speckle field within the ultrasound transducer focal region presents significant challenges, as several speckle modes are present (Figure 7.1(a) and (b)). If multiple speckles contribute with equal weighting the feedback signal uniformly mixes the information coming from individual speckles and does not lead to focus optimization. However, the transducer focal region does not detect acoustic waves uniformly. Instead, a focused ultrasound transducer displays a Gaussian spatial sensitivity, which essentially weights the speckle field; giving higher weighting to speckles closer to the center (Figure 7.1(b)). By preferentially

weighting a single speckle mode, the spatially non-uniform photoacoustic feedback localizes the optical intensity to a single speckle smaller than the acoustic focus (Figure 7.1(a) and (b)).

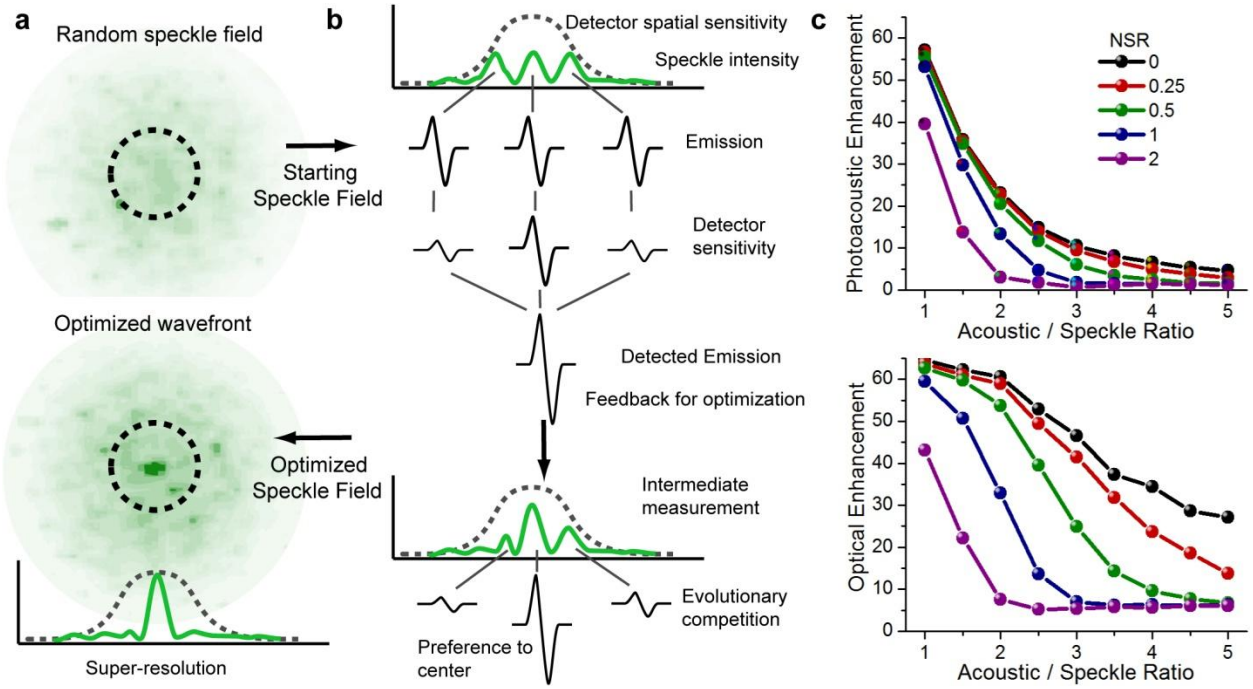

Figure 7.1. Optical focus creation with photoacoustic feedback: illustration and simulation. (a) The transducer focal region (dotted circle) illuminated with a speckle field (top) and the optimized speckle field with a sub-acoustic optical focus (bottom). (b) Profile of speckle grains and the detector spatial sensitivity. Each photoacoustic emission from the speckle grains is weighted by the Gaussian spatial sensitivity of the acoustic transducer. These emissions coherently combine to provide the photoacoustic feedback signal. During wavefront optimization with the photoacoustic feedback an optical focus forms at the center of the acoustic transducer due to the weight preference. (c) Simulation results of the photoacoustic and optical enhancements achieved after genetic algorithm optimization with various acoustic focus to speckle size ratios and noise-to-signal ratios (NSR).

7.3 Simulation

Simulations of the wavefront optimization elucidate the mechanism by which a spatially non-uniform sensitivity produces a tight optical focus when multiple modes participate in the feedback (see Section 7.7.1 for methods). Here, we use an evolutionary algorithm[52] that creates competition among modes within the acoustic focus. The number of modes, determined by the acoustic spot to optical speckle size ratio, and noise (noted as noise-to-signal ratio: NSR) are varied and the optimized photoacoustic signal and optical field analyzed. The wavefront optimization feedback uses an equivalent photoacoustic signal by integrating the total weighted light fluence throughout the acoustic focus. The signal improvement is assessed by photoacoustic enhancement, defined as the optimized photoacoustic signal divided by the mean of the photoacoustic signals of the initial population in the genetic algorithm[52]. In contrast, the optical enhancement evaluates the improvement in the maximum intensity of an individual speckle output mode as the ratio between its intensity and the initial average intensity. Interestingly, the optical enhancement outperforms the photoacoustic enhancement as the number of modes is increased (Figure 7.1(c)). The photoacoustic enhancement is integrated over the acoustic focal area while the optical enhancement is not. This indicates the optical energy localizes to an area smaller than the acoustic focus, creating an optical focus regardless of the small speckle size compared to the acoustic feedback. Furthermore, the optimized optical field most likely positions the enhanced speckle at the center of the acoustic focus (further details in Section 7.7.2). Thus, despite optimizing the wavefront based on feedback from multiple speckle modes within the acoustic focus, the light localizes to a single speckle, creating an optical focus.

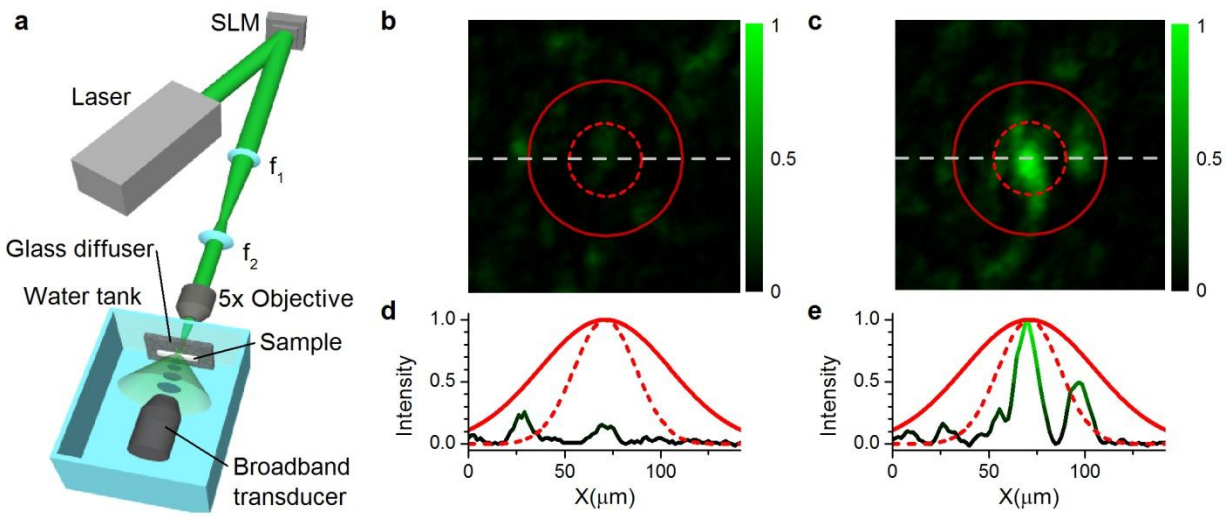

Figure 7.2. Experimental sub-acoustic focus creation. (a) Experimental set-up. (b) The speckle field without the optimized wavefront. (c) The sub-acoustic optical focus generated by the optimized wavefront. The red circles show the approximate filtered transducer focal region (80 MHz, -6 dB, dashed line) and focal spot size at the frequency peak of the detected photoacoustic response (50 MHz, -6 dB, solid line). (d,e) Cross sections of the approximate transducer focal regions (red) and the corresponding optical intensity distribution (black).

7.4 Experiment

7.4.1 Demonstration of sub-acoustic optical focus generation

We experimentally demonstrate the ability to localize a scattered light field to a sub-acoustic focus via photoacoustic feedback using the system shown in Figure 7.2(a). For this demonstration a 50 μm diameter black alpaca hair is selected for photoacoustic feedback, because it overfills both the acoustic transducer focal region and the speckle spot size (13 μm as measured through autocorrelation of Figure 7.2(b)). The high bandwidth acoustic transducer provides a wide range of frequency feedback. Because the transducer focal size inversely relates to frequency, the photoacoustic optimization signal is high-pass filtered, effectively limiting the acoustic focal diameter (-6 dB) to 38 μm, as shown by the dashed line in Figure 7.2(d). After genetic algorithm optimization of the optical wavefront through phase modulation with the SLM, the photoacoustic signal is enhanced by 8.5. The optimization creates a 13 μm (FWHM) focused

spot (Figure 7.2(c) and (e)), with an optical enhancement of 24, or three times the photoacoustic enhancement. As predicted, a small, single speckle optical focus is created despite integrating many speckle output modes within the photoacoustic feedback signal.

7.4.2 Demonstration of photoacoustic resolution improvement

Next, we demonstrate the resolution improvement by imaging a black alpaca hair (25 μm diameter) placed behind a scatterer. To understand the nature of the resolution improvement, we perform photoacoustic imaging by scanning the hair under three different optical fields (uniform, random speckle and optimized speckle). A photoacoustic image of the hair illuminated with a uniform optical field is shown in Figure 7.3(a). Here, the measured photoacoustic FWHM of the hair is found to be on average 79 μm, which agrees with the expected size given the acoustic resolution (see Section 7.8). With a glass diffuser placed in the optical path a random speckle field is created. The photoacoustic image reconstructed with this illumination is shown in Fig 7.3(b). Interestingly, the FWHM of the hair decreases to an average of 55 μm. The random speckle field does show a resolution improvement, likely due to the speckle arrangement within the transducer (i.e. a few intense speckles that provided improved resolution). Through genetic algorithm optimization of the optical wavefront on a large (43 μm diameter) alpaca hair the photoacoustic signal is enhanced by 6. Photoacoustic imaging with the optimized wavefront provides both the highest SNR and the best resolution as shown in Fig 7.3(c). The measured FWHM of the alpaca hair decreases to 30 μm. Assuming the optimization creates an optical focus of similar size to that of Figure 7.2(c), the resolution increases by five to six times compared to the acoustic resolution.

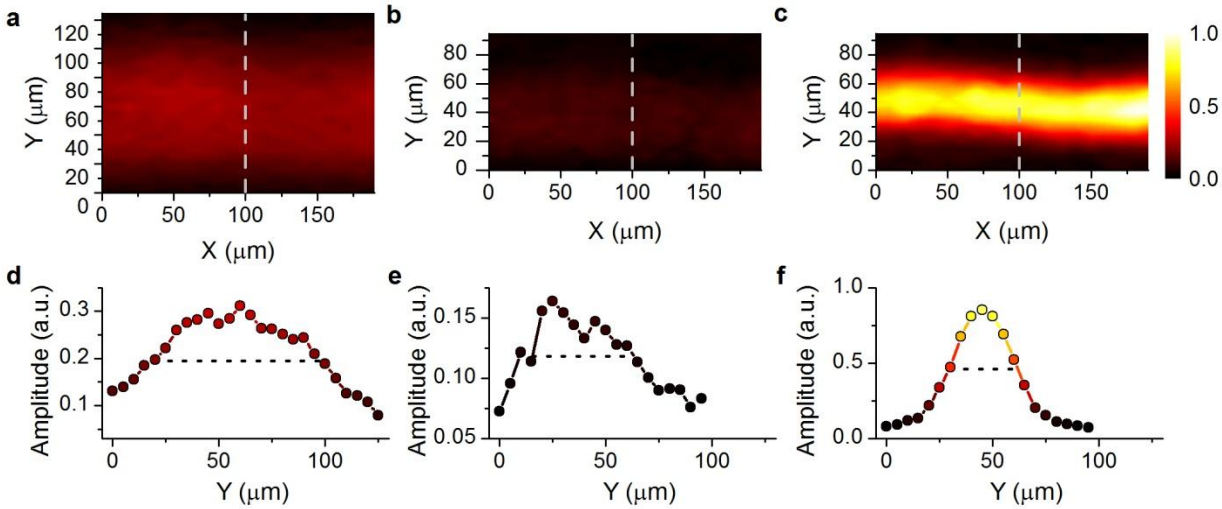

Figure 7.3. Resolution measurement with 25 μm black alpaca hair. The photoacoustic images created with different optical illuminations: (a) acoustic resolution using uniform illumination (no scatterer), (b) random optical speckle field from scatterer, (c) wavefront optimized speckle focus. (d), (e), and (f) show cross sections corresponding to the white dashed lines.

7.4.3 Super-resolution photoacoustic image reconstruction

Super-resolution photoacoustic imaging performed on a sweat bee wing, which provides an interesting complex structure, reveals significant resolution and signal improvement. As with the alpaca hair, we present photoacoustic images of the wing with uniform (Figure 7.4(a)) and random speckle (Figure 7.4(b)) illuminations for comparison. For the wavefront optimization we select an extended feedback region (~40x40 μm) at the intersection of the large vein on the leading edge of the wing and a branching vein. After optimization the signal strength improved by a factor of 10 over the random speckle field illumination. We image the bee wing by scanning it behind the scatterer (Figure 7.4(c)). The photoacoustic image significantly improves after optimization both in resolution and SNR, which facilitates 3D image reconstruction by sectioning the photoacoustic waveform temporally (Figure 7.4(d))[75]. With the uniform and random speckle fields small features, visible in the optical image (Figure 7.4(e)), such as hairs spaced 15-30 μm apart on the wing result in a high background signal and broadening of the

prominent vein features. However, with the optimized focus image, the hairs are individually resolvable (see Section 7.9). By treating the 4 μm wide hairs as point sources we measure the optical resolution to be 13.2 μm through autocorrelation of the imaged hairs.

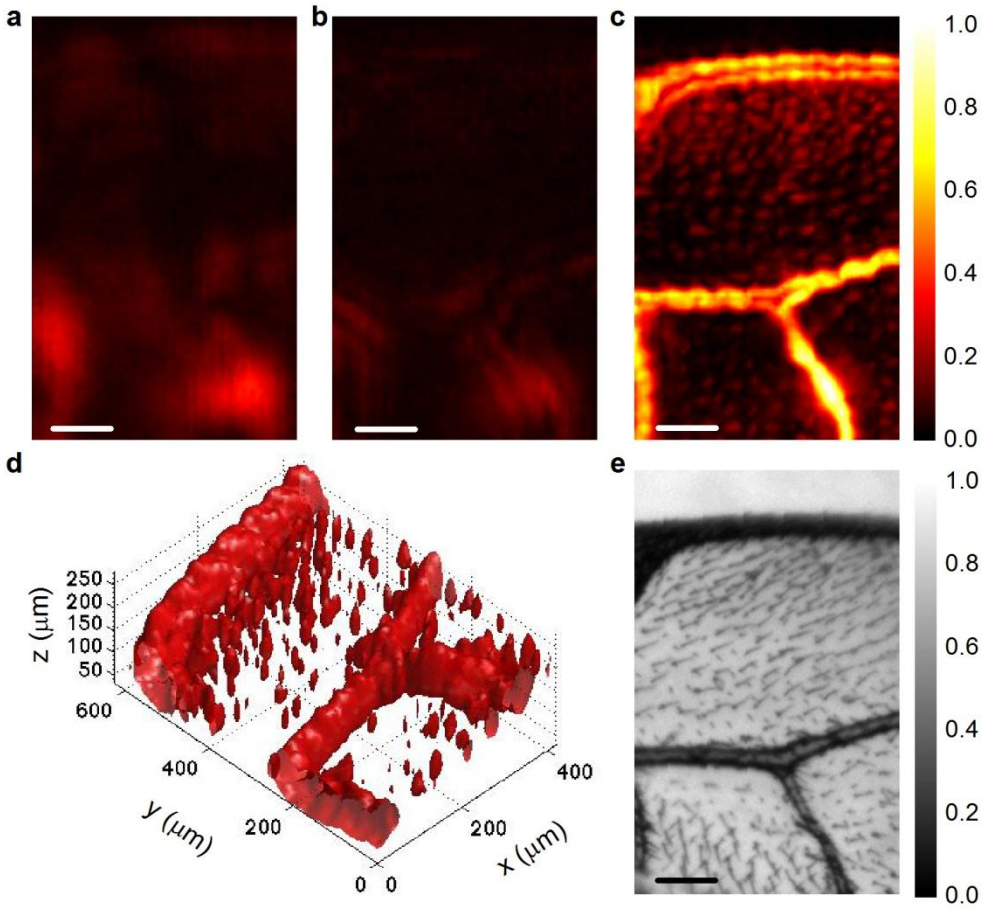

Figure 7.4. Photoacoustic image reconstructions of sweat bee wing. The photoacoustic images created with different optical illuminations, scale bars are all 100 μm: (a) acoustic resolution using uniform illumination (no scatterer), (b) random optical speckle field from scatterer, (c) wavefront optimized speckle focus. (d) 3D reconstruction of the optimized wavefront image. (e) The optical image of the same section of wing.

7.5 Conclusions

In conclusion, we have proposed and demonstrated a technique to create an optical focus behind a scattering medium that enables improved resolution and SNR of photoacoustic imaging. The spatially varying feedback signal provided by the ultrasound transducer allowed the

wavefront to evolve into a single speckle optical focus through mode competition. The method created an optical focal spot 5 times smaller than the acoustic focal spot size even though the optimization takes place on an extended absorber. The formation of this focus allowed for imaging absorbing samples at a higher resolution and SNR than possible without the scatterer. The technique is thus ideal for imaging through an opaque wall with resolution beyond that provided by the feedback mechanism. In this work, due to limitations imposed by a low laser repetition rate, the images presented were obtained by scanning the object while keeping the scatterer fixed. A straightforward extension would enable scanning of the laser beam and/or the acoustic transducer by continuous update of the wavefront[66]. Interestingly, the approach does not require use of the so-called memory effect[77], [115], [79] which would limit the applicability to weak or thin scatterers. The results presented here also suggest a path to increase the depth of optical resolution photoacoustic microscopy by providing high intensity optical foci deeper into tissue. This also opens up opportunities for 3D imaging applications in the diffusive regime beyond the sound wave diffraction-limited resolution, including medical imaging, photothermal therapy, neuroscience, and optogenetics.

7.6 Appendix A: Methods

7.6.1 Set-up

The experimental data are obtained using the set-up illustrated in Figure 7.2(a.) A collimated 532 nm, 5 ns pulsed laser (Continuum Surelight I20, 20Hz repetition rate) illuminates a spatial light modulator (SLM) (Boulder Non-linear Systems, 512x512 pixels) for wavefront shaping. The SLM is imaged onto the back aperture of a long working distance microscope objective (5x, 0.14 NA). The wavefront focuses into a water tank and onto the surface of a glass

diffuser. An absorbing sample ~8 mm behind the scatterer is mounted onto a 2D translation stage for scanning in the x and y dimensions. A 90 MHz (Olympus, V3512, 50 MHz bandwidth) focusing ultrasound transducer placed in the water detects the photoacoustic signal. After pre-amplification, an oscilloscope records, digitizes, and sends the detected signal to a computer for analysis.

To analyze the optical focus an Air Force resolution target is placed above the alpaca hair. After wavefront optimization the reflecting target is lowered into the focus to deflect the light to an imaging lens and CCD for analysis. The resolution target also provides calibration for the system magnification.

7.6.2 Uniform and Speckle Illumination

Photoacoustic images generated using random speckle illumination (Figure 7.3(b) and Figure 7.4(b)) had the same speckle size as the optimized wavefront case. The speckle illumination is created by encoding a flat phase on the SLM. For uniform optical illumination the scatterer is removed from the optical beam path (Figure 7.3(a) and Figure 7.4(a)).

7.6.3 Signal processing

During wavefront optimization low frequency signals are removed using a 2nd order Butterworth digital high-pass filter with an 80 MHz cut-off frequency to limit the feedback area. In contrast, image reconstructions do not use the high-pass filter, but instead use the unfiltered signal. These images are reconstructed with the maximum peak to peak value from the waveform from each position.

7.7 Appendix B: Simulation

7.7.1 Simulation methods

Simulations are used to explore the resulting optical speckle field after wavefront optimization utilizing an equivalent photoacoustic feedback mechanism. The simulation models the scattering process as a linear relation between the complex field at the input modes and the complex field at the acoustic transducer focal region:

$$E_m = \sum_{n}^{N} t_{mn} A_n e^{i\phi_n}, \tag{7.1}$$

where the optical path through the scattering material is represented by an MxN transmission matrix, and t_{mn}, generated from a circular Gaussian distribution[48], [49]. The amplitude, A_n, is uniform across all input modes and $A_n = 1/\sqrt{N}$. ϕ_n is the phase at input mode n. Each transmission matrix element relates the field at an input mode to an output speckle mode, E_m. The simulation uses a genetic algorithm for phase optimization to maximize the intensity of the photoacoustic signal[52]. The cost function, C, for the photoacoustic feedback GA is defined as the summation of the weighted intensities of each speckle output mode, m, within the transducer focal region.

$$C = \sum_{m=1}^{M} w_m \bullet |E_m|^2. \tag{7.2}$$

Each intensity being weighted by its location within the Gaussian shaped acoustic focus. The speckle field output mode locations are determined by placing the speckles in a hexagonal sampling grid and randomly shifting them about the preselected grid location. The weighting factor, w_m, is then selected based on the spatial location of each speckle in the Gaussian profile shown in Figure 7.5(a), in which the white circle represents -6 dB value. The simulation assumes

that the transducer focus is within a homogeneous absorbing material, so no additional weighting is applied. Finally, additive Gaussian noise is added to the cost function measurement to simulate experimental conditions.

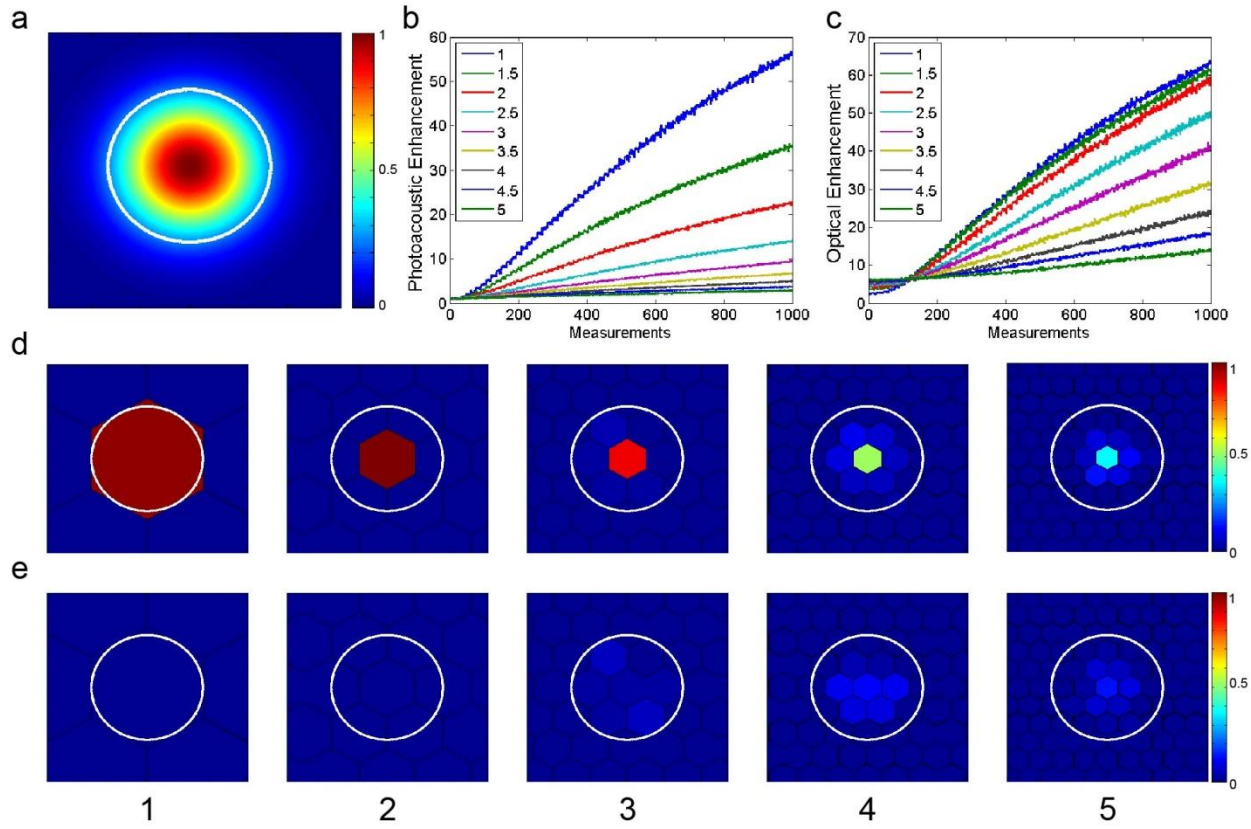

Figure 7.5. Simulation results showing the spatial confinement of optical focus. (a) The Gaussian function used to weight the output speckle modes. (b, c) The progression of the photoacoustic and optical enhancements as the genetic algorithm optimization progresses for various acoustic/speckle ratios at an NSR of 0.25. (d) The probability of each speckle output mode, distributed in a hexagonal grid, achieving the highest intensity after optimization for various acoustic/speckle ratios. (e) The probability that a mode will achieve a value greater than half of the maximum intensity. This illustrates that the focus will most likely lie within a single output speckle mode. The white circles in d and e represent the -6dB Gaussian weighting extent.

The simulation is run to compare the expected enhancement produced by different ratios of the acoustic focus diameter and the speckle size. This elucidates the consequence of having an increasing number of optical speckle modes within the photoacoustic feedback. The simulation also provides insight into the development of the speckle modes as the photoacoustic signal

optimizes. The GA variables selected mimic the experimental variables, with 800 spatial input modes and 1000 measurements. The simulation was repeated 100 times for five NSR values (0, 0.25, 0.5, 1.0, and 2.0) and nine acoustic to speckle diameter ratios (1 through 5 stepped every 0.5). As in the experiment, the photoacoustic enhancement is defined as the ratio of the cost function (equation 2) during optimization to the average cost function of the initial genetic algorithm population. The optical enhancement is the maximum optical intensity, $|E_m|^2$, divided by the mean intensity of all output speckle modes before optimization.

7.7.2 Simulation Analysis

Despite distributing multiple optical speckle output modes within a weighted feedback volume, the simulation shows a preference of enhancement to a single output speckle mode. Figure 7.5(b) shows an average of the photoacoustic enhancements during optimization for NSR of 0.25, similar to the experimental conditions. As the speckle size decreases relative to the acoustic focus size the photoacoustic enhancement is significantly lower after optimization. The speckle output mode data provides additional insight into the optimization. Although, the optical enhancement also decreases with decreasing speckle size the drop is significantly smaller than the photoacoustic enhancement (Figure 7.5(c) also NSR 0.25), thus indicating that an optical focus is formed with speckle size smaller than the acoustic feedback. The variation in the value initial enhancements shown in this plot is simply a result of the number of initial output modes. The higher the number of modes included, the more likely an output mode has a high random speckle value. Figure 7.5(d) and e illustrate the distribution of light within the transducer focus (white circle represents -6 dB). Figure 7.5(d) shows the probability of a speckle output mode, represented by the hexagonal grid, achieving the highest intensity after optimization for acoustic to speckle ratios of 1, 2, 3, 4, and 5. In all cases the optical output mode at the center of the

acoustic focus is most likely to be highest. Figure 7.5(e) shows how well the optimization confines the optical enhancement to a single speckle. Specifically it illustrates the probability that an output mode will have a value greater than half of the maximum intensity. As can be seen this virtually did not happen when the acoustic ratio was less than 4 times larger than the speckle. However, with smaller speckle sizes the likelihood increases, although it remains low at any speckle output mode.

7.8 Appendix C: Photoacoustic Imaging Resolution

The resolution of photoacoustic imaging in tissue depends on optical depth penetration[118]. In optical resolution photoacoustic microscopy the optical field is focused within a millimeter of the tissue surface allowing resolution beyond the acoustic wavelength. To penetrate deeper into tissue the optical field cannot be focused using conventional means and the resolution is dictated by the frequency of acoustic waves detected by the ultrasound transducer. To demonstrate that the wavefront optimization created an optical focus behind a scattering medium the received acoustic waveforms were analyzed.

The received time domain acoustic waveforms (Figure 7.6(a)-(c)) from the center of the alpaca hair image (Figure 7.3) were Fourier transformed to determine the frequency content and the corresponding acoustic resolution. This process was repeated over the area of the imaged hair. Uniform illumination produced acoustic waveforms with center frequencies ranging from 56.9 MHz to 38.1 MHz which corresponds to estimated range of -6dB acoustic diameters ($0.61\lambda/NA$) of 54 µm to 80 µm, respectively. The lower limit of the estimated acoustic focal diameter corresponds to the measured Alpaca hair (79 µm) under uniform illumination, indicating acoustic resolution. Illumination with a random speckle field produced acoustic

waveforms with center frequencies ranging from 59.5 MHz to 39 MHz which corresponds to estimated range of -6dB acoustic diameters of 51 µm to 78 µm, respectively. The measured diameter of the alpaca was in between the upper and lower limits of the acoustic focal diameter. The random speckle field could have slightly improved resolution depending on the intensity and relative location of the speckles within the acoustic focus. Illumination with the optimized wavefront produced acoustic waveforms with center frequencies ranging from 59.9 MHz to 46.8 MHz which corresponds to estimated range of -6dB acoustic diameters of 51 µm to 65 µm, respectively. However, the measured diameter of the Alpaca hair was significantly smaller (30 µm) for the optimized illumination. Hence, the improved resolution for optimized illumination was not due to higher frequency content, rather an optical focus that was smaller than the acoustic resolution.

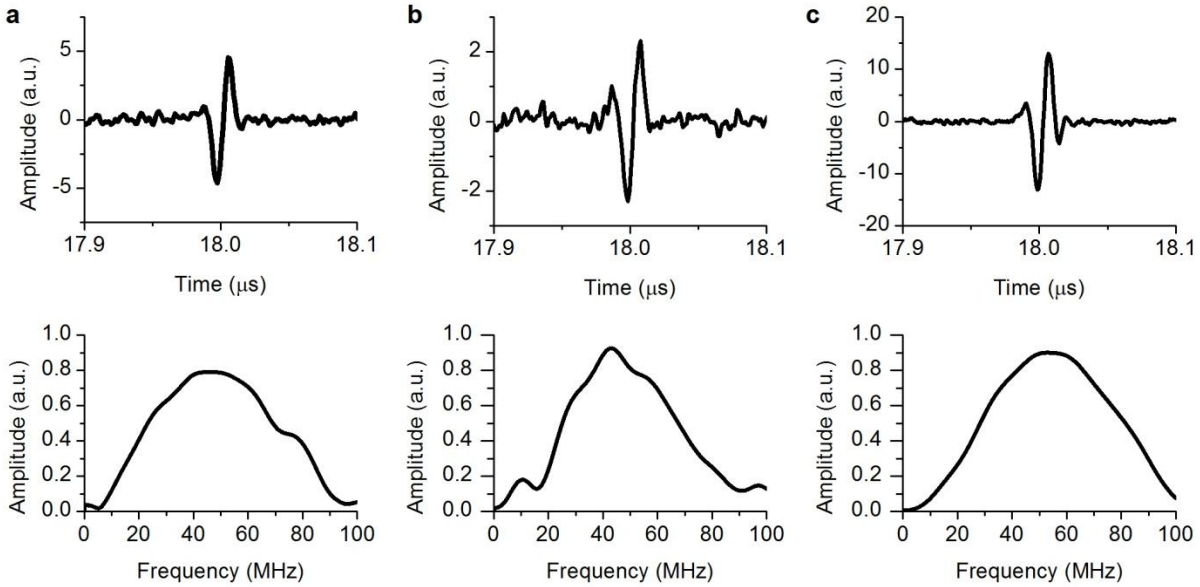

Figure 7.6. Received acoustic waveforms during photoacoustic imaging. The received acoustic waveforms from the center of the Alpaca hair image: (a)-(c), time domain and the corresponding frequency content below (a), uniform illumination (no scatterer) center frequency of 46.2 MHz, (b), random optical speckle field from scatterer center frequency of 43.1 MHz, (c), wavefront optimized speckle focus center frequency of 52.9 MHz.

7.9 Appendix D: Sweat bee wing hair analysis

To verify that the small 4 µm hairs on the sweat bee wing were photoacoustically imaged with the optimized wavefront illumination, we performed a normalized cross correlation measurement between the photoacoustic image of the hair and the optical image (shown in Figure 7.8). To ensure that only the hairs were contributing to the correlation measurement a subset of the photoacoustic image was used for the comparison which only contained potential hair signals. When the images overlapped the cross correlation value reached a peak, indicating that there was a strong correlation between the locations of the hairs in the optical image and the structure within the photoacoustic image. Therefore, we infer that the hairs were photoacoustically imaged.

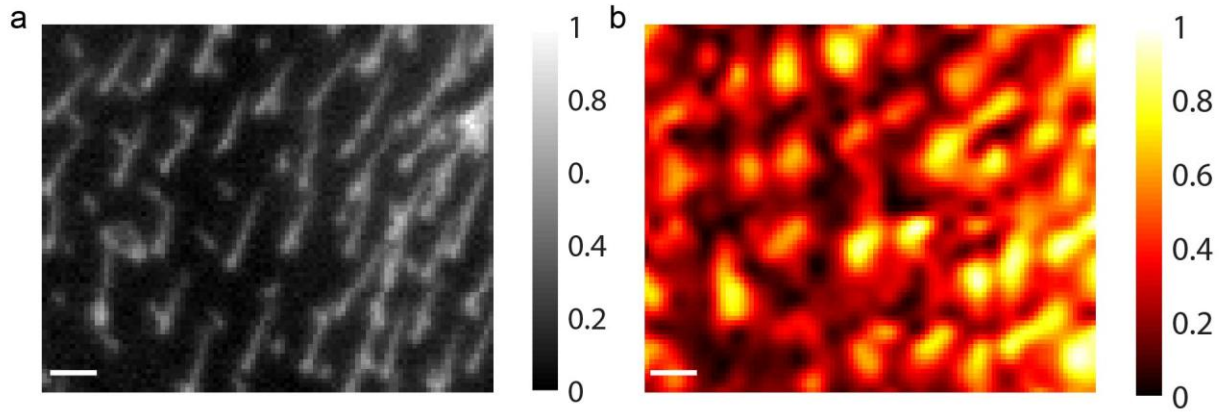

Figure 7.7. Sweat bee wing hair photoacoustic imaging. (a) A subset of the optical image shown in Figure 7.4(d) containing only the hairs. (b) The corresponding photoacoustic image obtained with the enhanced speckle illumination. A normalized cross correlation analysis of the two images reveals a strong correlation when they overlap, indicating the photoacoustic signatures correspond to the hairs. The scale bars are 20 µm.

CHAPTER 8

DISCUSSION AND FUTURE WORK

Early holographic work in imaging through turbid media utilized the deterministic nature of scattering and revealed the potential for wavefront correction to enable imaging through a thin scattering layer. Although the initial methods never overcame several limitations to become feasible imaging tools, they laid the groundwork for future development. Subsequent optical scattering media imaging techniques were based on the concept of filtering out scattered light, but were unable to image into the diffusive regime. In recent years, new wavefront shaping methods for controlling light through scattering materials have reopened the possibility of imaging beyond the ballistic regime[47]. For these to be successful in biomedical applications they must overcome tissue dynamic turbidity with high speed optimization and operate with a blind feedback. This thesis presents algorithms and high speed modulation systems to address the speed requirement and also expands on photoacoustic optimization to demonstrate blind sub-acoustic focus creation to enable super-resolution imaging through turbid media. Yet, this work is in its infancy and much remains to be done before these technologies can be implemented into biomedical imaging devices.

Light control through turbid media using genetic algorithm (GA) wavefront optimization is demonstrated in Chapters 2 and 3. The genetic algorithm optimization as described in Chapter 2 is ideal for non-dynamic turbid samples. In a dynamic sample the algorithm optimizes toward a maximum value. Once the transmission matrix varies too far from the optimized mask, the subsequent generation's performance would worsen. To regain a high enhancement the algorithm would have to reinitialize and start over again. An ideal dynamic turbid media optimization algorithm, however, would maintain a high enhancement, essentially reaching a steady state intensity value. For the GA to overcome dynamic turbidity and enable a steady state enhancement it should be modified. A couple pathways toward obtaining this include maintaining a high mutation rate throughout optimization and limiting the number of generations that a phase mask remains in the population. These modifications would allow the GA to constantly refresh the population with new input mode phase values (high mutation rate) and eliminate high performing masks after they become obsolete. In this way, perhaps, the GA could account for dynamic samples and maintain high focus intensity throughout optimization. Another potential approach to resolving this would be to explore new algorithms for optimization with dynamic turbid media.

Chapter 4 describes the implementation of a high-speed wavefront optimization system which utilizes the high switching speed of a digital micromirror device (DMD) to spatially modulate phase via computer generated binary amplitude holography. The main limitation imposed by the high-speed wavefront optimization technique is the short integration time allowed for photon collection. Currently, all of the demonstrated blind iterative optimization focusing methods necessitate a long photon collection time. The original blind focusing method requires a single fluorescent particle placed in a scatterer, which seems impractical for

biomedical implementation both in terms of bead sparsity and means of placement[11], [68]. In addition to its lack of practicality, due to scattering a single fluorescent bead placed deep in tissue would contribute few photons to the detector, thus requiring a long integration time. Another option, the two-photon fluorescence (TPF) feedback used to optimize an ultrashort pulse, could be used to eliminate the sparsity constraint for beads[61], [81]. However, the low efficiency of the TPF process would add considerable complications to its implementation with high speed optimization, especially in the diffusive regime. One possible route toward overcoming this is with GA optimization, because of its exceptional performance in low signal-to-noise ratio environments[52].

Another possibility for enabling high-speed optimization with blind focusing is implementing a digital optical phase conjugation (DOPC) system with the TI-DMD. An important distinction between the iterative optimization methods and DOPC is the number of required measurements. On one hand, the iterative methods require several hundred measurements, as an example, the DMD high-speed wavefront optimization uses 768 measurements to optimize 256 input modes[66]. In contrast, DOPC only needs a single image, which allows for an integration time three orders of magnitude longer than iterative techniques to optimize in the same time frame. Furthermore, the number of optimized input modes is only limited by the scattering layer and the optical system[102], thus enabling the possibility of optimizing thousands of input modes with a single frame.

DOPC, however, also has drawbacks. The two primary blind focusing methods demonstrated with DOPC have low photon collection constraints as well. The use of second harmonic generation particles would be limited by the process efficiency, which, like TPF, would suffer significantly in the diffusive regime. Using ultrasound guide-stars is promising, but

the low efficiency of acoustically modulating photons limits the technique[70]. Furthermore, the demonstrated methods for using ultrasound guide-stars to achieve sub-acoustic optical foci utilize DOPC with iterative techniques[71], [72], thereby imposing more restrictive timing requirements for high-speed optimization.

One potentially attractive solution involves combining photoacoustic feedback with the DMD high-speed wavefront optimization system. This would enable acoustic feedback, which is less susceptible to the deleterious scattering effects in tissue, as opposed to current methods which rely on optical feedback, whose intensity exponentially decays with depth. With these combined the short integration time required for high speed optimization would correspond to a single nanosecond pulse generating a single acoustic wave. This could be repeated at a rate similar to the high DMD modulation speed, thus opening the door to high speed focusing into a scattering sample.

The super-resolution photoacoustic imaging technique described in Chapters 6 and 7 for seeing behind a scattering wall was a significant contribution to the existing blind focusing work. The original demonstration imaged the absorbing sample behind the scattering layer by scanning the sample independent of the scatterer. The optimization time of the system was limited by the 20 Hz repetition rate of the laser, which necessitated scanning the sample behind the stationary scattering layer. For this technique to be feasible in biomedical applications, it must image without scanning the object behind a fixed scattering layer. This could be implemented by scanning the acoustic transducer and re-optimizing at new points. A high-speed photoacoustic feedback system could enable millisecond scale focusing times with this re-optimization imaging method. However, advancing this to allow super-resolution imaging will be a significant task and how to approach it remains uncertain. A first step could be additional research into the

mechanism for sub-acoustic focusing in regards to the frequency content of the optimized signal. The frequency of the detected acoustic wave is determined by the generating source of the wave, either by the size of the absorbing object or the extent of the illumination. By optimizing the frequency content an additional means of control for creating the sub-acoustic optical focus could be utilized to extract the information to create sub-acoustic resolution images.

CHAPTER 9

CONCLUSIONS

This Dissertation presents several significant contributions in the area of light control through scattering media. These advancements are specifically aimed to increase the speed of focus creation through a scattering layer and enable focusing and imaging behind scattering layers without physical access inside or behind the scatterer.

Focusing through scattering media using genetic algorithm (GA) wavefront optimization is introduced in Chapter 2. The initial motivation for implementation of the GA is for parallel mode optimization to increase the wavefront optimization speed. The GA achieves this by demonstrating a higher initial rate of intensity improvement than other algorithms. Significantly, the analysis reveals that an additional strength of the GA is the ability to optimize in low signal-to-noise environments much more effectively than other algorithms. For example, a simulation shows that in conditions where the noise level is twice the signal level, the GA achieves a one order of magnitude greater optical enhancement than other algorithms. The GA is increasingly used in wavefront control optimization for spectral control[119], spatio-temporal control[61], [120], photoacoustic feedback[75], [76], and digital ultrasonically encoded optical focusing[121]. Furthermore, as future experiments continue to increase the optimization speed

and focusing depth and thus becoming more photon-starved, it is likely that GA use will continue to expand.

The GA is also used in Chapter 3 in a first demonstration of image projection through scattering media. The GA, with a modified cost function, demonstrates a unique ability to generate multiple focal spots with uniform intensities through a scattering material. Multiple focal spot focusing paves the way for photo-dynamic therapy[84], and multi-neuronal excitation[86] through scattering tissue layers. Furthermore, the extension of this technique to multiple color light control illustrates its potential for multiple fluorophore excitation in deep-tissue imaging.

The work described in this thesis also explores high-speed wavefront optimization through the novel use of a binary amplitude spatial light modulator. Chapter 4 describes how binary amplitude holograms encoded with a digital micromirror device (DMD) for high-speed phase modulation enable the creation of the fastest turbid media focusing wavefront optimization system. This device measures 256 input modes in 34 ms; an order of magnitude faster than any other demonstrated method. The high DMD modulation speed is fully utilized with the inclusion of FPGA processing to achieve a 37 ms focusing time. In Chapter 5 this system is further extended for use with multi-mode fibers for focus creation through the fiber. This demonstration provides a possible route for overcoming mode-coupling within these fibers and has potential applications in biomedical endoscopic imaging systems and telecommunications.

The photoacoustic imaging technique described in Chapter 6 demonstrates the first photoacoustic image reconstruction through a scattering wall using optimized wavefront shaping. The wavefront shaping increased the optical fluence by an order of magnitude, thereby significantly improving the signal strength and, consequently, the image contrast. Additionally,

the acoustic detection enabled the first demonstration of three-dimensional imaging through a scattering layer without use of the memory effect.

Further exploring the photoacoustic wavefront optimization in Chapter 7 reveals the potential for a simple optical system to image through an opaque wall with a higher resolution than provided by the feedback. By optimizing the photoacoustic signal with an evolutionary competition among the contributing optical speckle modes only a single speckle mode achieves significant enhancement. The sub-acoustic focus generation indicates a potential method for increasing the depth of optical resolution photoacoustic microscopy by providing a high intensity optical focus in the diffusive regime of tissue. Indeed, sub-acoustic optical focus creation deep in tissue holds potential benefits for a variety of biomedical sensing and imaging applications and represents an important contribution to the focusing through turbid media body of work.

BIBLIOGRAPHY

[1] I. M. Vellekoop and A. P. Mosk, “Universal Optimal Transmission of Light Through Disordered Materials,” *Phys. Rev. Lett.*, vol. 101, no. 12, p. 120601, 2008.

[2] A. P. Mosk, A. Lagendijk, G. Lerosey, and M. Fink, “Controlling waves in space and time for imaging and focusing in complex media,” *Nat. Photonics*, vol. 6, no. 5, pp. 283–292, May 2012.

[3] P. Sebbah, Ed., *Waves and imaging through complex media*. Dordrecht; Boston: Kluwer Academic Publishers, 2001.

[4] M. I. Mishchenko, L. D. Travis, and A. A. Lacis, *Multiple scattering of light by particles: radiative transfer and coherent backscattering*. Cambridge; New York: Cambridge University Press, 2006.

[5] C. W. J. Beenakker, “Random-matrix theory of quantum transport,” *Rev. Mod. Phys.*, vol. 69, no. 3, p. 731, Jul. 1997.

[6] J. W. Goodman, *Speckle Phenomena in Optics: Theory and Applications*. Roberts and Company Publishers, 2007.

[7] A. Fenster and D. B. Downey, “3-D ultrasound imaging: a review,” *IEEE Eng. Med. Biol. Mag.*, vol. 15, no. 6, pp. 41–51, 1996.

[8] M. Xu and L. V. Wang, “Photoacoustic imaging in biomedicine,” *Rev. Sci. Instrum.*, vol. 77, p. 041101, 2006.

[9] A. A. Richards, *Alien Vision: Exploring the Electromagnetic Spectrum with Imaging Technology, Second Edition*. 1000 20th Street, Bellingham, WA 98227-0010 USA: SPIE, 2011.

[10] A. P. Gibson, J. C. Hebden, and S. R. Arridge, “Recent advances in diffuse optical imaging,” *Phys. Med. Biol.*, vol. 50, no. 4, p. R1, Feb. 2005.

[11] I. Vellekoop and C. Aegerter, “Scattered light fluorescence microscopy: imaging through turbid layers,” *Opt. Lett.*, vol. 35, no. 8, pp. 1245–1247, Apr. 2010.

[12] K. Si, R. Fiolka, and M. Cui, “Fluorescence imaging beyond the ballistic regime by ultrasound pulse guided digital phase conjugation,” *Nat. Photonics*, vol. 6, no. 10, pp. 657–661, Oct. 2012.

[13] L. C. Kennedy, L. R. Bickford, N. A. Lewinski, A. J. Coughlin, Y. Hu, E. S. Day, J. L. West, and R. A. Drezek, “A New Era for Cancer Treatment: Gold-Nanoparticle-Mediated Thermal Therapies,” *Small*, vol. 7, no. 2, pp. 169–183, 2011.

[14] B. A. Wilt, L. D. Burns, E. T. W. Ho, K. K. Ghosh, E. A. Mukamel, and M. J. Schnitzer, “Advances in Light Microscopy for Neuroscience,” *Annu. Rev. Neurosci.*, vol. 32, p. 435, 2009.

[15] M. Elias, N. Mas, and P. Cotte, “Review of several optical non-destructive analyses of an easel painting. Complementarity and crosschecking of the results,” *J. Cult. Herit.*, vol. 12, no. 4, pp. 335–345, Oct. 2011.

[16] A. F. Koenderink, A. Lagendijk, and W. L. Vos, “Optical extinction due to intrinsic structural variations of photonic crystals,” *Phys. Rev. B*, vol. 72, no. 15, p. 153102, Oct. 2005.

[17] E. N. Leith and J. Upatnieks, “Reconstructed Wavefronts and Communication Theory,” *J. Opt. Soc. Am.*, vol. 52, no. 10, pp. 1123–1128, Oct. 1962.

[18] E. N. Leith and J. Upatnieks, “Holograms: Their Properties and Uses,” *Opt. Eng.*, vol. 4, no. 1, pp. 040103–040103–, 1965.

[19] E. N. Leith and J. Upatnieks, “Holographic Imagery Through Diffusing Media,” *J. Opt. Soc. Am.*, vol. 56, no. 4, pp. 523–523, Apr. 1966.

[20] J. W. Goodman, W. H. Huntley, D. W. Jackson, and M. Lehmann, “Wavefront-reconstruction imaging through random media,” *Appl. Phys. Lett.*, vol. 8, no. 12, p. 311, Jun. 1966.

[21] B. J. Chang, J. S. Chang, and E. N. Leith, “Imaging through scattering media with an achromatic interferometer,” *Opt. Lett.*, vol. 4, no. 4, pp. 118–120, Apr. 1979.

[22] E. Spitz, “Holographic reconstruction of objects through a diffusing medium in motion,” *C R Acad Sci Paris Ser B*, vol. 264, pp. 1449–1452, 1962.

[23] K. A. STETSON, “Holographic Fog Penetration,” *J. Opt. Soc. Am.*, vol. 57, no. 8, pp. 1060–1061, Aug. 1967.

[24] A. W. Lohmann and H. Schmalfuss, “Holography through fog. A new version,” *Opt. Commun.*, vol. 26, no. 3, pp. 318–321, Sep. 1978.

[25] A. Cunha and E. Leith, “Generalized one-way phase-conjugation systems,” *J. Opt. Soc. Am. B*, vol. 6, no. 10, pp. 1803–1812, Oct. 1989.

[26] E. N. Leith and C.-P. Kuei, “Interferometric method for imaging through inhomogeneities,” *Opt. Lett.*, vol. 12, no. 3, pp. 149–151, Mar. 1987.

[27] H. Chen and L. Shentu, “Achromatic interferometer for imaging through turbulence,” *Appl. Opt.*, vol. 31, no. 9, pp. 1274–1278, Mar. 1992.

[28] C. Dunsby and P. M. W. French, “Techniques for depth-resolved imaging through turbid media including coherence-gated imaging,” *J. Phys. Appl. Phys.*, vol. 36, no. 14, p. R207, Jul. 2003.

[29] G. Indebetouw, “Distortion-free imaging through inhomogeneities by selective spatial filtering,” *Appl. Opt.*, vol. 29, no. 35, pp. 5262–5267, Dec. 1990.

[30] G. E. Anderson, F. Liu, and R. R. Alfano, “Microscope imaging through highly scattering media,” *Opt. Lett.*, vol. 19, no. 13, pp. 981–983, Jul. 1994.

[31] J. B. Pawley, *Handbook of Biological Confocal Microscopy*. Springer, 1995.

[32] K. Dowling, M. J. Dayel, M. J. Lever, P. M. W. French, J. D. Hares, and A. K. L. Dymoke-Bradshaw, “Fluorescence lifetime imaging with picosecond resolution for biomedical applications,” *Opt. Lett.*, vol. 23, no. 10, pp. 810–812, May 1998.

[33] E. A. McLean, J. Burris, and M. P. Strand, “Short-pulse range-gated optical imaging in turbid water,” *Appl. Opt.*, vol. 34, no. 21, pp. 4343–4351, Jul. 1995.

[34] J. Watson, P. Georges, T. Lepine, B. Alonzi, and A. Brun, “Imaging in diffuse media with ultrafast degenerate optical parametric amplification,” *Opt. Lett.*, vol. 20, no. 3, pp. 231–233, Feb. 1995.

[35] L. Wang, P. P. Ho, X. Liang, H. Dai, and R. R. Alfano, “Kerr-Fourier imaging of hidden objects in thick turbid media,” *Opt. Lett.*, vol. 18, no. 3, pp. 241–243, Feb. 1993.

[36] M. D. Duncan, R. Mahon, L. L. Tankersley, and J. Reintjes, “Time-gated imaging through scattering media using stimulated Raman amplification,” *Opt. Lett.*, vol. 16, no. 23, pp. 1868–1870, Dec. 1991.

[37] J. M. Schmitt, “Optical coherence tomography (OCT): a review,” *IEEE J. Sel. Top. Quantum Electron.*, vol. 5, no. 4, pp. 1205–1215, 1999.

[38] V. Ntziachristos, “Going deeper than microscopy: the optical imaging frontier in biology,” *Nat. Methods*, vol. 7, no. 8, pp. 603–614, Aug. 2010.

[39] J. D. Briers and S. Webster, “Laser speckle contrast analysis (LASCA): a nonscanning, full-field technique for monitoring capillary blood flow,” *J. Biomed. Opt.*, vol. 1, no. 2, pp. 174–179, 1996.

[40] J. Wang, Z. Zhi, Z. Han, C. Liu, Z. Mao, X. Wen, and D. Zhu, “Accessing the structure and function information of deep skin blood vessels with noninvasive optical method,” 2009, vol. 7176, p. 71760Q–71760Q–8.

[41] S. Yuan, A. Devor, D. A. Boas, and A. K. Dunn, “Determination of optimal exposure time for imaging of blood flow changes with laser speckle contrast imaging,” *Appl. Opt.*, vol. 44, no. 10, pp. 1823–1830, Apr. 2005.

[42] A. G. Bell, “On the production and reproduction of sound by light,” *Am. J. Sci.*, vol. s3–20, no. 118, pp. 305–324, Oct. 1880.

[43] H. F. Zhang, K. Maslov, G. Stoica, and L. V. Wang, “Functional photoacoustic microscopy for high-resolution and noninvasive in vivo imaging,” *Nat. Biotechnol.*, vol. 24, no. 7, pp. 848–851, Jul. 2006.

[44] H. W. Babcock, “Adaptive Optics Revisited,” *Science*, vol. 249, no. 4966, pp. 253–257, Jul. 1990.

[45] J. W. Hardy, “Adaptive optics: a progress review,” 1991, vol. 1542, pp. 2–17.

[46] E. Pastrana, “Adaptive optics for biological imaging,” *Nat. Methods*, vol. 8, no. 1, pp. 45–45, Jan. 2011.

[47] I. M. Vellekoop and A. P. Mosk, “Focusing coherent light through opaque strongly scattering media,” *Opt. Lett.*, vol. 32, no. 16, pp. 2309–2311, 2007.

[48] M. A. Webster, T. D. Gerke, A. M. Weiner, and K. J. Webb, “Spectral and temporal speckle field measurements of a random medium,” *Opt. Lett.*, vol. 29, no. 13, pp. 1491–1493, Jul. 2004.

[49] I. M. Vellekoop and A. P. Mosk, “Phase control algorithms for focusing light through turbid media,” *Opt. Commun.*, vol. 281, no. 11, pp. 3071–3080, Jun. 2008.

[50] I. M. Vellekoop, A. Lagendijk, and A. P. Mosk, “Exploiting disorder for perfect focusing,” *Nat. Photonics*, vol. 4, no. 5, pp. 320–322, May 2010.

[51] M. Cui, “Parallel wavefront optimization method for focusing light through random scattering media,” *Opt. Lett.*, vol. 36, no. 6, pp. 870–872, Mar. 2011.

[52] D. B. Conkey, A. N. Brown, A. M. Caravaca-Aguirre, and R. Piestun, “Genetic algorithm optimization for focusing through turbid media in noisy environments,” *Opt. Express*, vol. 20, no. 5, p. 4840, Feb. 2012.

[53] S. M. Popoff, G. Lerosey, R. Carminati, M. Fink, A. C. Boccara, and S. Gigan, “Measuring the Transmission Matrix in Optics: An Approach to the Study and Control of Light Propagation in Disordered Media,” *Phys. Rev. Lett.*, vol. 104, no. 10, p. 100601, Mar. 2010.

[54] S. Popoff, G. Lerosey, M. Fink, A. C. Boccara, and S. Gigan, “Controlling Light Through Optical Disordered Media : Transmission Matrix Approach,” *1107.5285*, Jul. 2011.

[55] Z. Yaqoob, D. Psaltis, M. S. Feld, and C. Yang, “Optical phase conjugation for turbidity suppression in biological samples,” *Nat. Photonics*, vol. 2, no. 2, pp. 110–115, Feb. 2008.

[56] E. J. McDowell, M. Cui, I. M. Vellekoop, V. Senekerimyan, Z. Yaqoob, and C. Yang, “Turbidity suppression from the ballistic to the diffusive regime in biological tissues using optical phase conjugation,” *J. Biomed. Opt.*, vol. 15, no. 2, p. 025004, 2010.

[57] M. Cui and C. Yang, “Implementation of a digital optical phase conjugation system and its application to study the robustness of turbidity suppression by phase conjugation,” *Opt. Express*, vol. 18, no. 4, pp. 3444–3455, Feb. 2010.

[58] I. Freund, “Looking through walls and around corners,” *Physica A*, vol. 168, pp. 49–65, 1990.

[59] S. Popoff, G. Lerosey, M. Fink, A. C. Boccara, and S. Gigan, “Image transmission through an opaque material,” *Nat Commun*, vol. 1, no. 6, p. 81, 2010.

[60] O. Katz, E. Small, and Y. Silberberg, “Looking around corners and through thin turbid layers in real time with scattered incoherent light,” *Nat. Photonics*, vol. 6, no. 8, pp. 549–553, Jul. 2012.

[61] O. Katz, E. Small, Y. Bromberg, and Y. Silberberg, “Focusing and compression of ultrashort pulses through scattering media,” *Nat. Photonics*, vol. 5, no. 6, pp. 372–377, May 2011.

[62] D. J. McCabe, A. Tajalli, D. R. Austin, P. Bondareff, I. A. Walmsley, S. Gigan, and B. Chatel, “Spatio-temporal focusing of an ultrafast pulse through a multiply scattering medium,” *Nat Commun*, vol. 2, p. 447, 2011.

[63] J. Aulbach, B. Gjonaj, P. M. Johnson, A. P. Mosk, and A. Lagendijk, “Control of Light Transmission through Opaque Scattering Media in Space and Time,” *Phys. Rev. Lett.*, vol. 106, no. 10, p. 103901, Mar. 2011.

[64] I. M. Vellekoop and C. M. Aegerter, “Focusing light through living tissue,” in *Proc. SPIE*, 2010, vol. 7554, pp. 755430–755430–10.

[65] M. Cui, “A high speed wavefront determination method based on spatial frequency modulations for focusing light through random scattering media,” *Opt. Express*, vol. 19, no. 4, pp. 2989–2995, Feb. 2011.

[66] D. B. Conkey, A. M. Caravaca-Aguirre, and R. Piestun, “High-speed scattering medium characterization with application to focusing light through turbid media,” *Opt. Express*, vol. 20, no. 2, p. 1733, Jan. 2012.

[67] C. Stockbridge, Y. Lu, J. Moore, S. Hoffman, R. Paxman, K. Toussaint, and T. Bifano, “Focusing through dynamic scattering media,” *Opt. Express*, vol. 20, no. 14, p. 15086, Jun. 2012.

[68] I. M. Vellekoop, E. G. van Putten, A. Lagendijk, and A. P. Mosk, “Demixing light paths inside disordered metamaterials,” *Opt. Express*, vol. 16, no. 1, pp. 67–80, Jan. 2008.

[69] C. Hsieh, Y. Pu, R. Grange, and D. Psaltis, “Digital phase conjugation of second harmonic radiation emitted by nanoparticles in turbid media,” vol. 18, no. 12, pp. 533–537, 2010.

[70] X. Xu, H. Liu, and L. V. Wang, “Time-reversed ultrasonically encoded optical focusing into scattering media,” *Nat. Photonics*, vol. 5, no. 3, pp. 154–157, Jan. 2011.

[71] K. Si, R. Fiolka, and M. Cui, “Breaking the spatial resolution barrier via iterative sound-light interaction in deep tissue microscopy,” *Sci. Reports*, vol. 2, p. 748, Jan. 2012.

[72] B. Judkewitz, Y. M. Wang, R. Horstmeyer, A. Mathy, and C. Yang, “Speckle-scale focusing in the diffusive regime with time reversal of variance-encoded light (TROVE),” *Nat. Photonics*, vol. 7, no. 4, pp. 300–305, Mar. 2013.

[73] F. Kong, R. H. Silverman, L. Liu, P. V. Chitnis, K. K. Lee, and Y. C. Chen, “Photoacoustic-guided convergence of light through optically diffusive media,” *Opt. Lett.*, vol. 36, no. 11, pp. 2053–2055, Jun. 2011.

[74] T. Chaigne, O. Katz, A. C. Boccara, M. Fink, E. Bossy, and S. Gigan, “Controlling light in scattering media non-invasively using the photo-acoustic transmission-matrix,” arXiv e-prints 1305.6246, May 2013.

[75] A. M. Caravaca-Aguirre, D. B. Conkey, J. D. Dove, H. Ju, T. W. Murray, and R. Piestun, “High contrast three-dimensional photoacoustic imaging through scattering media by localized optical fluence enhancement,” *Opt. Express*, vol. 21, no. 22, pp. 26671–26676, Nov. 2013.

[76] D. B. Conkey, A. M. Caravaca-Aguirre, J. D. Dove, H. Ju, T. W. Murray, and R. Piestun, “Super-resolution photoacoustic imaging through a scattering wall,” arXiv e-print 1310.5736, Oct. 2013.

[77] I. Freund, M. Rosenbluh, and S. Feng, “Memory Effects in Propagation of Optical Waves through Disordered Media,” *Phys. Rev. Lett.*, vol. 61, no. 20, pp. 2328–2331, Nov. 1988.

[78] S. Feng, C. Kane, P. A. Lee, and A. D. Stone, “Correlations and Fluctuations of Coherent Wave Transmission through Disordered Media,” *Phys. Rev. Lett.*, vol. 61, no. 7, pp. 834–837, 1988.

[79] C.-L. Hsieh, Y. Pu, R. Grange, G. Laporte, and D. Psaltis, “Imaging through turbid layers by scanning the phase conjugated second harmonic radiation from a nanoparticle,” *Opt. Express*, vol. 18, no. 20, pp. 20723–20731, 2010.

[80] X. Yang, C.-L. Hsieh, Y. Pu, and D. Psaltis, “Three-dimensional scanning microscopy through thin turbid media,” *Opt. Express*, vol. 20, no. 3, p. 2500, Jan. 2012.

[81] J. Tang, R. N. Germain, and M. Cui, “Superpenetration optical microscopy by iterative multiphoton adaptive compensation technique.,” *Proc. Natl. Acad. Sci. U. S. A.*, vol. 109, no. 22, pp. 8434–9, May 2012.

[82] Y. M. Wang, B. Judkewitz, C. A. Dimarzio, and C. Yang, “Deep-tissue focal fluorescence imaging with digitally time-reversed ultrasound-encoded light.,” *Nat. Commun.*, vol. 3, p. 928, Jan. 2012.

[83] C.-L. Hsieh, Y. Pu, R. Grange, and D. Psaltis, “Digital phase conjugation of second harmonic radiation emitted by nanoparticles in turbid media,” *Opt. Express*, vol. 18, no. 12, pp. 12283–12290, Jun. 2010.

[84] T. J. Dougherty, C. J. Gomer, B. W. Henderson, G. Jori, D. Kessel, M. Korbelik, J. Moan, and Q. Peng, “Photodynamic Therapy,” *J. Natl. Cancer Inst.*, vol. 90, no. 12, pp. 889–905, Jun. 1998.

[85] T. Cizmár, M. Mazilu, and K. Dholakia, “In situ wavefront correction and its application to micromanipulation,” *Nat. Photonics*, vol. 4, no. 6, pp. 388–394, May 2010.

[86] V. Nikolenko, K. E. Poskanzer, and R. Yuste, “Two-photon photostimulation and imaging of neural circuits,” *Nat. Methods*, vol. 4, no. 11, pp. 943–950, Nov. 2007.

[87] R. L. Haupt and S. E. Haupt, *Practical Genetic Algorithms*. John Wiley & Sons, 2004.

[88] U. Mahlab, H. J. Caulfield, and J. Shamir, “Genetic algorithm for optical pattern recognition,” *Opt. Lett.*, vol. 16, no. 9, pp. 648–650, May 1991.

[89] Y. Choi, T. D. Yang, C. Fang-Yen, P. Kang, K. J. Lee, R. R. Dasari, M. S. Feld, and W. Choi, “Overcoming the Diffraction Limit Using Multiple Light Scattering in a Highly Disordered Medium,” *Phys. Rev. Lett.*, vol. 107, no. 2, p. 023902, Jul. 2011.

[90] O. Bryngdahl and F. Wyrowski, “I Digital Holography – Computer-Generated Holograms,” in *Progress in Optics*, vol. Volume 28, E. Wolf, Ed. Elsevier, 1990, pp. 1–86.

[91] F. van Beijnum, E. G. van Putten, A. Lagendijk, and A. P. Mosk, “Frequency bandwidth of light focused through turbid media,” *Opt. Lett.*, vol. 36, no. 3, pp. 373–375, Feb. 2011.

[93] D. Akbulut, T. J. Huisman, E. G. V. Putten, and W. L. Vos, “Focusing light through random photonic media by binary amplitude modulation,” *Opt. Express*, vol. 19, no. 5, pp. 4017–4029, 2011.

[94] M. Cui, E. J. McDowell, and C. Yang, “An in vivo study of turbidity suppression by optical phase conjugation (TSOPC) on rabbit ear,” *Opt. Express*, vol. 18, no. 1, pp. 25–30, Jan. 2010.

[95] D. Dudley, W. M. Duncan, and J. Slaughter, “Emerging digital micromirror device (DMD) applications,” in *Proc SPIE*, 2003, vol. 4985, pp. 14–25.

[96] T. Kohlgraf-Owens and A. Dogariu, “Finding the field transfer matrix of scattering media,” *Opt. Express*, vol. 16, no. 17, pp. 13225–13232, Aug. 2008.

[97] W.-H. Lee, “III Computer-Generated Holograms: Techniques and Applications,” in *Progress in Optics*, vol. Volume 16, E. Wolf, Ed. Elsevier, 1978, pp. 119–232.

[98] C. Rathjen, “Statistical properties of phase-shift algorithms,” *J. Opt. Soc. Am.*, vol. 12, no. 9, pp. 1997–2008, 1995.

[99] K. Freischlad and C. L. Koliopoulos, “Fourier description of digital phase-measuring interferometry,” *J. Opt. Soc. Am.*, vol. 7, no. 4, pp. 542–551, Apr. 1990.

[100] D. B. Conkey, A. M. Caravaca-Aguirre, and R. Piestun, “High-speed scattering medium characterization with application to focusing light through turbid media,” *Opt. Express*, vol. 20, no. 2, p. 1733, Jan. 2012.

[101] R. Di Leonardo and S. Bianchi, “Hologram transmission through multi-mode optical fibers,” *Opt. Express*, vol. 19, no. 1, pp. 247–254, Jan. 2011.

[102] I. N. Papadopoulos, S. Farahi, C. Moser, and D. Psaltis, “Focusing and scanning light through a multimode optical fiber using digital phase conjugation,” *Opt. Express*, vol. 20, no. 10, p. 10583, Apr. 2012.

[103] I. N. Papadopoulos, S. Farahi, C. Moser, and D. Psaltis, “High-resolution, lensless endoscope based on digital scanning through a multimode optical fiber,” *Biomed. Opt. Express*, vol. 4, no. 2, pp. 260–270, Jan. 2013.

[104] T. Cizmár and K. Dholakia, “Exploiting multimode waveguides for pure fibre-based imaging,” *Nat. Commun.*, vol. 3, p. 1027, Aug. 2012.

[105] Y. Choi, C. Yoon, M. Kim, T. D. Yang, C. Fang-Yen, R. R. Dasari, K. J. Lee, and W. Choi, “Scanner-Free and Wide-Field Endoscopic Imaging by Using a Single Multimode Optical Fiber,” *Phys. Rev. Lett.*, vol. 109, no. 20, p. 203901, Nov. 2012.

[106] R. N. Mahalati, R. Y. Gu, and J. M. Kahn, “Resolution limits for imaging through multi-mode fiber,” *Opt. Express*, vol. 21, no. 2, pp. 1656–1668, Jan. 2013.

[107] A. Yariv, “Three-dimensional pictorial transmission in optical fibers,” *Appl. Phys. Lett.*, vol. 28, no. 2, p. 88, Jan. 1976.

[108] A. Gover, C. P. Lee, and A. Yariv, “Direct transmission of pictorial information in multimode optical fibers,” *J. Opt. Soc. Am.*, vol. 66, no. 4, pp. 306–311, Apr. 1976.

[109] G. J. Dunning and R. C. Lind, “Demonstration of image transmission through fibers by optical phase conjugation,” *Opt. Lett.*, vol. 7, no. 11, pp. 558–560, Nov. 1982.

[110] A. A. Friesem, U. Levy, and Y. Silberberg, “Parallel transmission of images through single optical fibers,” *Proc. IEEE*, vol. 71, no. 2, pp. 208–221, 1983.

[111] R. Di Leonardo, S. Bianchi, and R. Di Leonardo, “Hologram transmission through multi-mode optical fibers,” *Opt. Express*, vol. 19, no. 1, p. 247, Dec. 2010.

[112] H. Schreiber and J. H. Bruning, “Phase Shifting Interferometry,” in *Optical Shop Testing*, Daniellacara, Ed. John Wiley & Sons, Inc., 2006, pp. 547–666.

[113] C. Stockbridge, Y. Lu, J. Moore, S. Hoffman, R. Paxman, K. Toussaint, and T. Bifano, “Focusing through dynamic scattering media,” *Opt. Express*, vol. 20, no. 14, pp. 15086–15086, Jun. 2012.

[114] C. G. A. Hoelen, F. F. M. de Mul, R. Pongers, and A. Dekker, “Three-dimensional photoacoustic imaging of blood vessels in tissue,” *Opt. Lett.*, vol. 23, no. 8, pp. 648–650, Apr. 1998.

[115] J. Bertolotti, E. G. van Putten, C. Blum, A. Lagendijk, W. L. Vos, and A. P. Mosk, “Non-invasive imaging through opaque scattering layers.,” *Nature*, vol. 491, no. 7423, pp. 232–4, Nov. 2012.

[116] D. B. Conkey and R. Piestun, “Color image projection through a strongly scattering wall,” *Opt. Express*, vol. 20, no. 25, p. 27312, Nov. 2012.

[117] K. Maslov, H. F. Zhang, S. Hu, and L. V. Wang, “Optical-resolution photoacoustic microscopy for in vivo imaging of single capillaries,” *Opt. Lett.*, vol. 33, no. 9, p. 929, Apr. 2008.

[118] L. V. Wang and S. Hu, “Photoacoustic Tomography: In Vivo Imaging from Organelles to Organs,” *Science*, vol. 335, no. 6075, pp. 1458–1462, Mar. 2012.

[119] E. Small, O. Katz, Y. Guan, and Y. Silberberg, “Spectral control of broadband light through random media by wavefront shaping,” *Opt. Lett.*, vol. 37, no. 16, pp. 3429–3431, Aug. 2012.

[120] E. Small, O. Katz, and Y. Silberberg, “Spatiotemporal focusing through a thin scattering layer,” *Opt. Express*, vol. 20, no. 5, p. 5189, Feb. 2012.

[121] J. W. Tay, P. Lai, Y. Suzuki, and L. V. Wang, “Digital ultrasonically encoded (DUE) optical focusing into random media,” arXiv e-print 1309.3497, Sep. 2013.